Downloaded from orbit.dtu.dk on: Apr 25, 2024

DTU Library

Production and utilization of unconventional radiometals for advanced diagnostics and therapy

Fonslet, Jesper

Publication date:
2017

Document Version
Publisher's PDF, also known as Version of record

Link back to DTU Orbit

Citation (APA):
Fonslet, J. (2017). *Production and utilization of unconventional radiometals for advanced diagnostics and therapy*. DTU Nutech.

General rights
Copyright and moral rights for the publications made accessible in the public portal are retained by the authors and/or other copyright owners and it is a condition of accessing publications that users recognise and abide by the legal requirements associated with these rights.

- Users may download and print one copy of any publication from the public portal for the purpose of private study or research.
- You may not further distribute the material or use it for any profit-making activity or commercial gain
- You may freely distribute the URL identifying the publication in the public portal

If you believe that this document breaches copyright please contact us providing details, and we will remove access to the work immediately and investigate your claim.

DTU/NUTECH

Production and utilization of unconventional radiometals for advanced diagnostics and therapy

PhD thesis

Jesper Fonslet

23-05-2017

Preface

This thesis covers the majority of the work I conducted during the three years as a PhD student at the Technical University of Denmark. The focus of the thesis has been expanding the number of available radiometals for diagnostics and therapy. Special focus has been on long-lived PET- and Auger-emitting radionuclides. It has been very inspiring working in this highly interdisciplinary field, encompassing biology, nuclear physics, and inorganic chemistry.

I would like to thank my supervisors Mikael Jensen, Andreas I. Jensen, and Gregory W. Severin for their continuous support. Especially, I would like to thank Gregory W. Severin for mentoring me on a daily basis and for his friendship during these three years. My gratitude further extends to all members of the Hevesy Laboratory for making it the unique and cheerful workplace that it is.

Finally, I would like to thank my immediate family, especially my wife Britt, for continued love, help and support, and my two rays of light, my sons Axel and Buster, for always brightening up dark days.

The work was partially funded by the MATHIAS project (European Union Seventh Framework Programme FP7/2007-2013 under Grant 602820).

Corrections to this version:

Page 23: In Figure 11 the Zr-89 dose was not correct. The figure has been corrected and a paragraph in the main text has been removed to reflect this change.

Page 30 reads: ". Inductively Coupled Plasma Optical Emission Spectrometry (ICPOES) analysis of the ^{52}Mn used in the failed attempt later showed a significant Cr contamination of > 600 ng/MBq." This was corrected and now reads: "….showed a significant Zn contamination of > 600 ng/MBq."

Abstract

The continued development in biochemistry delivers vectors capable of specifically identifying foreign entities like malignancies and infections. Many of these vectors have long circulation time *in vivo*, resulting in optimal biodistribution for imaging several days post injection. The diagnostic potential of these can only be fully utilized if non-standard radionuclides with half-lives extending beyond those of the standard catalogue (^{11}C, ^{18}F, and ^{64}Cu) are available. As for therapy, the increased specificity of new vectors strengthens the argument for using targeted radionuclide therapy, as they allow delivery of therapeutic doses to target tissues with minimal unspecific uptake and dose in healthy non-target tissues. This allows for the use of a wider range of radionuclides, like α-emitters, for which high specificity is needed due to their high toxicity. The development of highly specific, internalizing vectors opens for use of Auger emitters. The therapeutic effect of these radionuclides most likely relies on internalization and translocation to the cell nucleus, because of their extremely localized, short-range dose deposition. Although the selection such vectors is still limited, the development of robust production methods for Auger emitters is crucial for investigating the basic principles of Auger therapy.

The focus of this thesis has been expanding the number of isotopes and techniques available in the nuclear medicine toolbox.

The work performed using diagnostic isotopes includes:

^{52}Mn: A production and separation method for high specific activity ^{52}Mn was developed. Labeling conditions and serum stability for ^{52}Mn-DOTA were investigated, and ^{52}Mn was labeled to intact antibodies showing *in vivo* stability in mice.

^{89}Zr: Very high specific activity ^{89}Zr was produced. A labeling method for sensitive metalloproteins was developed. Further, the potential pitfalls in quality control of ^{89}Zr labeled proteins were documented.

^{45}Ti: A production and separation method for ^{45}Ti was developed and optimized. This work includes one of the first ever *in vivo* studies of a ^{45}Ti-compound.

The work performed using therapeutic isotopes includes:

^{177}Lu: The sensitive metalloprotein FVIIai was conjugated with the chelator cDTPA and labeled with ^{177}Lu for a therapeutic study. This included optimization of labeling conditions and development of quality control.

^{135}La: Pressed Ba-targets were produced and production and separation methods for high specific activity ^{135}La were developed. Labeling conditions were tested and cellular and human dosimetry of ^{135}La was calculated.

^{165}Er: A production method for ^{165}Er was developed, based on electron-capture-mediated release of ^{165}Er from DOTA.

Finally, a method was developed using ^{140}Nd for assaying cellular internalization of a compound *in vivo*. General dosimetry calculations and considerations are further presented to aid selection of the radionuclide when designing a radiopharmaceutical.

The combined work serves to aid further development in both pharmaceutical research, and diagnostic as well as therapeutic applications of radionuclides.

Resumé

Den fremskredne udvikling i farmacien, stiller vektorer til rådighed, der med høj specificitet kan identificere fremmedlegemer såsom cancer og infektion. Mange af disse har lang cirkulationstid *in vivo*, hvilket betyder at den optimale biodistribution ift. billeddannelse, først opnås flere dage efter stoffet er indgivet. Det diagnostiske potentiale af disse vektorer, kan kun udnyttes fuldt ved anvendelse af radionuklider med halveringstider, der overskrider hvad der er tilgængeligt i standardkataloget (^{11}C, ^{18}F, and ^{64}Cu). Hvad angår terapi, styrker nye vektorers øgede specificitet kun argumentet for anvendelse af radionuklidterapi, idet de tillader afsættelse af terapeutisk dosis i det målrettede væv, mens raskt væv skånes pga. lavt optag i dette. Det tillader brug af et bredere udvalg af radionuklider, såsom α-emitterne der grundet deres høje giftighed kræver meget specifikt optag. Udviklingen af internaliserende vektorer tillader ydermere anvendelse af Auger-emittere. Disses terapeutiske virkning, beror sandsynligvis på internalisering og translokation til cellekernen, idet deres udsendte elektroner har en meget kort rækkevidde. På trods af at vektorer med disse egenskaber stadig kun er få, er udviklingen af robuste metoder til fremstilling af Auger-emittere kritisk, for at de grundlæggende principper for deres anvendelse kan fastlægges.

Et gennemgående fokus for denne afhandling har været at udvide antallet af tilgængelige isotoper i den nuklearmedicinske værktøjskasse.

Resultater af projekter med diagnostiske isotope inkluderer:

^{52}Mn: Udvikling af en produktions- og separationsmetode til fremstilling af høj specifik aktivitets ^{52}Mn. Mærkningsbetingelser for- og serumstabilitet af ^{52}Mn-DOTA blev undersøgt, og *in vivo* stabilitet af ^{52}Mn mærkede antistoffer påvist i mus.

^{89}Zr: ^{89}Zr blev produceret med meget høj specifik aktivitet. Der blev udviklet en mærkningsstrategi til mærkning af særligt følsomme metalholdige proteiner. Derudover dokumenteredes særlige problemstillinger i kvalitetskontrollen af ^{89}Zr-mærkede proteiner.

^{45}Ti: En ny produktions- og separationsmetode blev udviklet og optimeret. Dette arbejde inkluderer et af de første studier med et ^{45}Ti-mærket sporstof.

Resultater af projekter med terapeutiske isotope inkluderer:

^{177}Lu: Det følsomme metalholdige protein FVIIai blev først konjugeret med chelatoren cDTPA og efterfølgende mærket med ^{177}Lu til en terapeutisk studie. Dette indebar optimering af mærkningsbetingelser og udvikling af metoder til kvalitetskontrol.

^{135}La: Pressede Ba-targets blev produceret og produktions- og separations metoder udviklet til fremstilling af ^{135}La i høj specifik aktivitet. Mærkningsbetingelser blev optimeret og den tillhørende cellulære og humane dosimetri beregnet.

^{165}Er: En produktionsmetode der bygger på frigivelse af ^{165}Er fra DOTA under ^{165}Tm-henfald via elektron indfangning.

Endeligt præsenteres en udviklet metode til *in vivo*-måling af internalisering ved hjælp af ^{140}Nd. Generelle dosimetriberegninger og betragtninger præsenteres derudover, med det formål at kunne understøtte valget, af det bedst egnede radionuklid i designet af nye radiolægemidler.

Det samlede arbejde tjener det formål at støtte videre udvikling, i såvel farmaceutisk forskning, som i diagnostiske- og terapeutiske anvendelser af radionuklider.

List of publications

Listed in the order presented in the thesis:

I. Graves, S. A., Hernandez, R., **Fonslet, J.**, England, C. G., Valdovinos, H. F., … Severin, G. W. (2015). Novel Preparation Methods of 52 Mn for ImmunoPET Imaging. *Bioconjugate Chemistry*, *26*(10), 2118–2124. (Published; Manuscript attached)

II. **Fonslet, J.**, Tietze, S., Jensen, A. I., Graves, S. A., & Severin, G. W. (2017). Optimized procedures for manganese-52: Production, separation and radiolabeling. *Applied Radiation and Isotopes*, *121*, 38–43. (Published; Manuscript attached)

III. Napieczynska H., Severin, G. W., **Fonslet, J.**, Wiehr, S., Menegakis A., Pichler B. J., Calaminus C. Imaging Neuronal Pathways with 52Mn PET. Toxicity Evaluation in Rats. (Submitted to Neuroimage; Manuscript attached)

IV. Severin, G. W., Nielsen, C. H., Jensen, A. I., **Fonslet, J.**, Kjær, A., & Zhuravlev, F. (2015). Bringing Radiotracing to Titanium-Based Antineoplastics: Solid Phase Radiosynthesis, PET and ex Vivo Evaluation of Antitumor Agent [^{45}Ti](salan)Ti(dipic). *Journal of Medicinal Chemistry*, *58*(18), 7591–7595. (Published; Manuscript attached)

V. **Fonslet J.**, Tran T.A., Siikanen J., Siragusa M., Jensen K. M., Jensen A.I., Lee B.Q., Severin G.W. ^{135}La as an auger electron emitter for targeted internal radiotherapy. (Submitted to Physics in Medicine and Biology; Manuscript attached)

VI. **Fonslet, J.**, Siikanen, J., & Severin, G. W. A Szillard-Chalmers Based Generator for the Auger Emitter Erbium-165 (In preparation; Manuscript attached)

VII. Jensen, M. M., **Fonslet, J.**, Knudsen, C. S., Jeppesen, T. E., Jensen, A. I., Severin, G. W., …. Kjær, A. Tissue factor targeted radionuclide therapy with 177Lu-FVIIai inhibits tumor growth of human pancreatic cancer xenografts. (In preparation)

VIII. Edem, P. E., **Fonslet, J.**, Kjær, A., Herth, M., & Severin, G. (2016). *In Vivo* Radionuclide Generators for Diagnostics and Therapy. *Bioinorganic Chemistry and Applications*, *2016*, 1–8. (Published; Manuscript attached)

IX. Severin, G.W., Kristensen, L. K., Nielsen, C. H., **Fonslet, J.**, Jensen, A. I., … Köster, U. Neodymium-140 as an *in vivo* generator for preclinical positron emission tomography (Submitted to Frontiers in Nuclear Medicine; Manuscript attached)

List of Abbreviations

ASIS/FVIIai:	Active Site Inhibited Factor Seven
cDTPA:	[(R)-2-Amino-3-(4-isothiocyanatophenyl)propyl]-trans-(S,S)-cyclohexane-1,2-diamine-pentaacetic acid
DFO:	Deferoxamine
DOTA:	1,4,7,10-tetraazacyclododecane-1,4,7,10-tetraacetic acid
DTPA:	diethylenetriaminepentaacetic acid
EC:	Electron Capture
eV:	Electron volt (1.602 × 10-19 J)
Gy:	gray [J/kg]
HEPES:	4-(2-hydroxyethyl)-1-piperazineethanesulfonic acid
HPLC:	High Performance Liquid Chromatography
IC:	Internal Conversion
ICPOES:	Inductively Coupled Plasma Optical Emission Spectroscopy
IPA:	Invasive Pulmonary Aspergillosis
LC:	Liquid Chromatography
LET:	Linear Energy Transfer
logP:	Octanol-water partition coefficient
MEMRI:	Manganese Enhanced Magnetic Resonance Imaging
MRI:	Magnetic Resonance Imaging
PET:	Positron Emission Tomography
PMT:	Photomultiplier Tube
RBE:	Relative Biological Effect
SPECT:	Single Photon Emission Computed Tomography
Sv:	Sievert [J/kg]
TLC:	Thin-Layer Chromatography
TOF:	Time OF Flight

Table of Contents

Preface 2
Abstract 3
Resumé 6
List of publications 7
List of Abbreviations 8
Introduction to the thesis 11
Invasive pulmonary aspergillosis 11
Structure of the thesis 12
1. General Introduction 13
1.1 Radiometal-based radiopharmaceuticals 13
1.2 Radionuclide production 14
1.3 Labeling with radiometals 17
2. Diagnostic isotopes 20
2.1 Introduction to SPECT/PET 20
2.2 MIRD/OLINDA 22
2.3 Choice of diagnostic radionuclide based on target kinetics 22
3. Projects based on diagnostic isotopes 27
3.1 Manganese-52 27
3.1.1 Paper I 31
3.1.2 Paper II 31
3.1.3 Paper III 31
3.1.4 Other ^{52}Mn-based work 31
3.2 Zirconium-89 33
3.2.1 Specific activity 35
3.2.2 Oxalate-free labeling 35
3.2.3 Inverse labeling 37
3.3 Titanium-45 39
3.3.1 Paper IV 40
4. Introduction to Therapeutic isotopes 42
4.1 Targeted radionuclide therapy 42
4.2 Radionuclides used in therapy 43
4.3 Choice of therapeutic radionuclide based on target size 46
5. Projects based on therapeutic isotopes 49

5.1 Lanthanum-135 49
5.1.1 Paper V 51
5.2 Erbium-165 53
5.2.1 Paper VI 54
5.3 Lutetium-177 56
5.3.1 Paper VII 57
6. Introduction to *in vivo* generators 60
6.1 Paper VIII 60
6.2 Paper IX 60
7. Discussion 63
7.1 Measurement of dose in targeted radionuclide therapy 63
7.2 Receptor saturation in Auger therapy 63
7.3 The importance of specific activity 64
7.4 RBE of Auger electrons 64
7.5 Clinical outlook 65
8. References 67

Introduction to the thesis

The chart of nuclides reveals many isotopes with properties suitable for use within nuclear medicine. Only few of these are used routinely, but the increased interest in use of nuclear imaging for both clinical and preclinical investigations is prompting development of a larger catalogue of available isotopes.

The general tendency in nuclear medicine departments of shifting from SPECT to PET, makes the development of PET radioisotopes with half-lives longer than ^{64}Cu ($T_{½}$ = 12.7 h) essential. These allow the longitudinal quantitative imaging of the traced biomolecules that is needed for determining tracer biodistribution at late time-points. This is beneficial in pharmaceutical investigations where the information can aid in tuning compounds for optimal pharmacokinetics. It is also an excellent tool in personalized medicine, seeing that the target expression patterns in tumors, metastasis, and other malignancies can be globally mapped and identified, allowing assessment of therapy efficacy ahead of treatment. Additionally, this is a necessary tool to assess the feasibility and associated dosimetry in radionuclide therapy.

There is also a need for isotopes for radionuclide therapy, especially with Auger electron emitters. Continued development and research in biomolecules continuously delivers improved vectors for therapy. One exciting direction that comes from a broadened and specially designed catalogue of vectors is the promise of intercellular targeting, where it is rapidly becoming possible for vectors to traffic radionuclides directly into the cellular nucleus. Radioactive isotopes with accompanying Auger electron cascades compliment this capability with pinpoint dose deposition, offering maximal dose to the targeted cells, and very little dose to neighboring tissues. In order for these Auger emitters to prove their efficacy, reliable methods for their production and chemical separation are needed.

The focus of this thesis is to expand the number of available isotopes in the nuclear medicine toolbox by providing production methods for both long-lived diagnostic PET isotopes as well as Auger emitters for therapy. The work has been done in the context of supplying candidate isotopes for use in the MATHIAS project, which partially funded this thesis. The intent of the MATHIAS project is to improve diagnostic and therapeutic methods for invasive pulmonary aspergillosis (IPA).

Invasive pulmonary aspergillosis

IPA is a leading cause of death in patients with hematological malignancies and following bone marrow transplants, with more than 200,000 reported infections and a mortality rate of 50% even when diagnosed and treated[1]. Historically, IPA is an opportunistic infection relying on neutropenia and was first described after the introduction of corticosteroids in the 1950's. The potential number of patients has substantially increased since due to the advent of HIV/AIDS, the large increase in solid organ and bone marrow transplants and the increased use of immunosuppressive drugs in treatment of autoimmune disorders[2]. An emerging group of patients at risk are those suffering from chronic obstructive pulmonary disease, which generally fare notably worse with a mortality rate exceeding 75%[3].

Diagnosis of IPA is challenging, as symptoms such as fevers unresponsive to antibiotics, and pulmonary infiltrates, are nonspecific and the analysis of blood for biomarkers, lacks specificity and sensitivity. Therefore, the current practice is based on culturing the fungus from biopsy lung-tissue samples, which is a time-consuming practice that delays diagnosis and treatment. A recent technique

relies on detection of galactomannan in sample fluids obtained by rinsing the infected area of the lung with saline[4]. Although no tissue samples are needed, it is still a very uncomfortable procedure for the commonly very sick patients.

An aim of the MATHIAS project is to provide a PET imaging-based method of diagnosis of IPA, built on the Aspergillus Fumigatus-specific antibody JF5[5]. Using this antibody in conjunction with a long-lived radiometal can provide non-invasive and accurate detection of IPA[6]. A further aim of the MATHIAS project was to investigate the feasibility of performing radionuclide therapy using the JF5 antibody. The project was performed by a consortium, consisting of Eberhard Karls Universität Tübingen (Germany), Universitätsklinikum Essen (Germany), ISCA Diagnostics Ltd. (United Kingdom), CheMatech SAS (France), Paul Scherrer Institute (Switzerland) and Danmarks Tekniske Universitet (Denmark). The responsibility of DTU in this consortium was developing and producing relevant radiometals for both diagnostics and therapy. This PhD comprises part of the work done to fulfill this responsibility.

Structure of the thesis

The projects comprising the thesis are divided into two groups: Projects developing diagnostic isotopes, and projects developing therapeutic isotopes. The thesis is likewise divided and, after a general introduction pertaining to all projects, is split in two. First, it focuses on diagnostics and the diagnostic isotopes produced. Second, the principles of radionuclide therapy are introduced before the projects involving therapeutic isotopes are presented. Finally, a project on *in vivo* generators, which bridges both categories, is introduced.

1. General Introduction

1.1 Radiometal-based radiopharmaceuticals

Radiometals are radioactive metal isotopes that can be utilized for medical diagnostics and in some cases as therapeutic agents for therapy of cancer. An expanding number of radiometals of varying physical properties like half-life, emissions and energies, are routinely being produced, allowing careful matching of the nuclear properties to applications[7].

Most radiometal-based radiopharmaceuticals are designed using the same three components: a vector for which information about the *in vivo* distribution is wanted; a chelator, which is matched for optimal stability of the chelator-radiometal complex; and finally the radiometal, which is chosen by matching the decay characteristics to the purpose of the radiopharmaceutical[8]. If the purpose is diagnostic, the radionuclide must provide photons of sufficient energy to exit the patient without scattering, yet low enough energy to interact with the scanner. Furthermore, to minimize the associated dose to the patient, radioisotopes with only suited diagnostic emissions are preferred, and the nuclear half-life should be matched to the vector kinetics. For therapeutic applications, the radionuclide should deliver a high local dose, with minimal long-range emissions. This generally means little-to-no gamma emissions, and a longer half-life than is generally used for diagnostics, as most of the decays are desired after the vector has distributed[9].

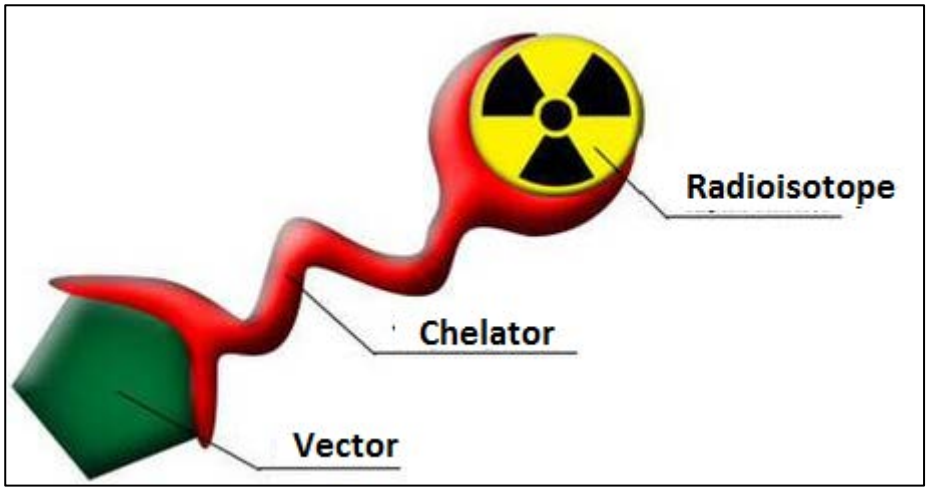

Figure 1: Typical design of a radiometal-based radiopharmaceutical. The radioisotope is bound to the vector via complexation in a chelator linked to the vector. Image adapted from Kruijff et al. [10].

The modular design of a radiometal-based radiopharmaceutical (Figure 1) makes for a virtually unlimited number of combinations, all relying on very similar labeling methods. This is where radiometals have an advantage over organic small molecule radiopharmaceuticals. The versatility of the modular build allows for modifications to the function of the tracer simply by changing the chelator-isotope construct conjugated to the vector. In this way, the same vector can be used for both Single Photon Emission Computed Tomography (SPECT) and Positron Emission Tomography (PET) and, if found suitable, the diagnostic isotope can be substituted for a therapeutic isotope that has been carefully chosen for its emissions. However, due to the nature of their relatively short half-lives, most radionuclides must be produced on demand. This is most commonly done using either charged particle- or neutron activation.

1.2 Radionuclide production

The radioisotopes produced in this thesis were made by charged particle activation. This method of activation has three major benefits compared to neutron activation. First, it provides variable incoming energy of the activating particle, allowing careful control of side reactions. Second, charged particle activation commonly creates radioactive products, which are different chemical elements than that of the irradiated target. Finally, charged particle accelerators often provide the ability to choose the incident particle itself (p, d or α), providing further opportunity to minimize coproduction of unwanted neighboring isotopes and facilitating subsequent separation.

These properties of charged particle activation theoretically allow the production of carrier-free radioisotopes, *i.e.*, the radioactive isotope in pure form, completely undiluted by stable isotopes of the same element. It further allows chemical removal of the bulk mass of the target material. Since the produced quantity of a radioisotope is extremely small compared to the number of target nuclei, the target material commonly needs to be removed for subsequent radiochemistry to be successful.

The primary accelerator for charged particle activation is the cyclotron (Figure 2). Commonly in the form of proton accelerators, they are widely available because of the widespread production of 2-deoxy-[^{18}F]fluoro-D-glucose ([^{18}F]FDG), supplying PET centers throughout the world. As of 2015, more than 1200 medical cyclotrons are in operation globally[11]. Typically, these medical cyclotrons supply protons of energy less than 20 MeV with available beam-currents of 50-200 μA.

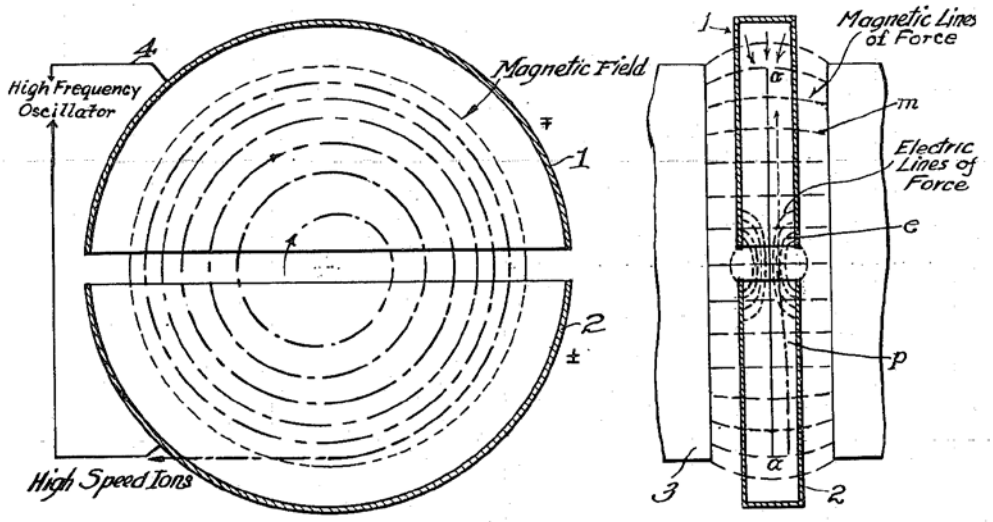

Figure 2: Schematic illustrating the basic cyclotron design. Ions are introduced in the center of the cyclotron and accelerated over the voltage applied between the two "dees". Contained in circular motion by a static magnetic field, the ions are repeatedly accelerated as they pass from one dee to the other. Because the radius of the circular motion is proportional to the velocity of the ions, they spiral outwards to higher radii as their energy increases. When they approach the edge of the acceleration chamber, they can be extracted towards the target. Adapted from Lawrence's original patent[12].

When the cyclotron-supplied high-energy particles hit a target, only a tiny fraction will cause nuclear transmutation and the rest will be stopped by either electron collisions or nuclear scattering. If the incoming particle is absorbed by a target atom it leaves the newly formed nucleus in in a highly excited and unstable state called the compound nucleus. Relaxation can occur via gamma- or particle (e.g. neutrons, protons or alphas) emission.

Nuclear reactions such as these cannot happen at any incoming particle energy. All nuclear reactions have an associated Q value denoting the energy released in the reaction. For Q > 0 the reaction is said to be exothermic (mass is converted to energy) and for Q < 0 it is said to be endothermic (energy is converted to mass). In (p,n)-reactions where the produced isotope will be radioactive and decay back to the target isotope this Q value will always be negative. For other reactions, this is not always the case[13,14].

To produce an isotope the incoming energy must be larger than -Q to satisfy energy conservation. However, when the Q value is negative the resulting nucleus and emitted particles cannot be at rest. In order to satisfy conservation of momentum, the resulting energy threshold (i.e. the minimum energy required to induce the reaction) is $E_{tr} = -Q(m_a + m_A)/m_A$. Here m_a denotes the rest mass of the incoming particle and m_A the resting mass of the target nucleus. Even though E_{tr} is the minimum energy needed to induce the reaction, reactions are not very likely to occur just above the threshold energy. This is because in order to enter the target nucleus the charged particle must traverse the Coulomb barrier. This electrostatic barrier is not incorporated in the threshold energy and has a height on the order of 1-2 MeV (depending on the Z value of the target material). The threshold energy describes the absolute minimum energy required for the reaction, and seeing that the charged particle can tunnel across the barrier, it is not required to completely overcome the barrier height. However, tunnelling is a very improbale event, and the cross section increases dramatically once the incident energy surpasses the combined threshold energy and coulomb barrier[13,14].

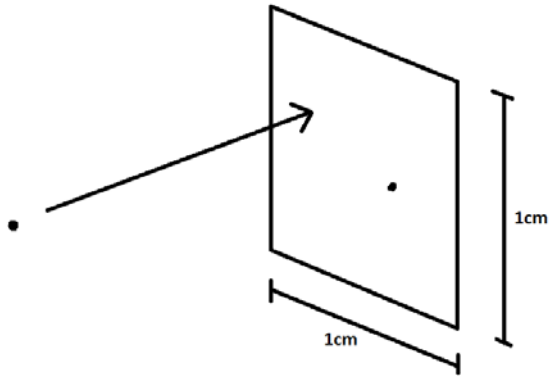

Figure 3: An illustration of the unit "barn": One proton passes through a surface of 1 cm² holding only a single atom. If the cross section is 1 barn for a given reaction between the proton and the target atom then the probability for that reaction occurring is in this setting 10^{-24}. The unit is measured in cm² simply because it describes probability per flux, i.e. $\frac{1}{1/cm^2} = cm^2$.

The term nuclear reaction cross section, denoted σ(E), is the probability for a nuclear reaction occurring through a certain reaction channel, like ^{52}Cr(p,n)^{52}Mn, as a function of incident energy. This notation means production of ^{52}Mn by bombarding ^{52}Cr with protons followed by evaporation of a neutron. The unit for the cross section is "barn" (b) with 1 barn = 10^{-24} cm²: a number very close to the area of the physical cross section of the uranium nucleus. Having the unit of area, the cross section describes a probability per unit flux, or, in other words, it describes the probability of the reaction, imagining just one target atom and one incident particle with a certain energy passing each other on a 1-cm² surface (Figure 3). That is: If a particle "a", moves through a surface S, containing one target nucleus A, then the probability of forming the B via the reaction A(a,b)B is equal to σ/S[13,14].

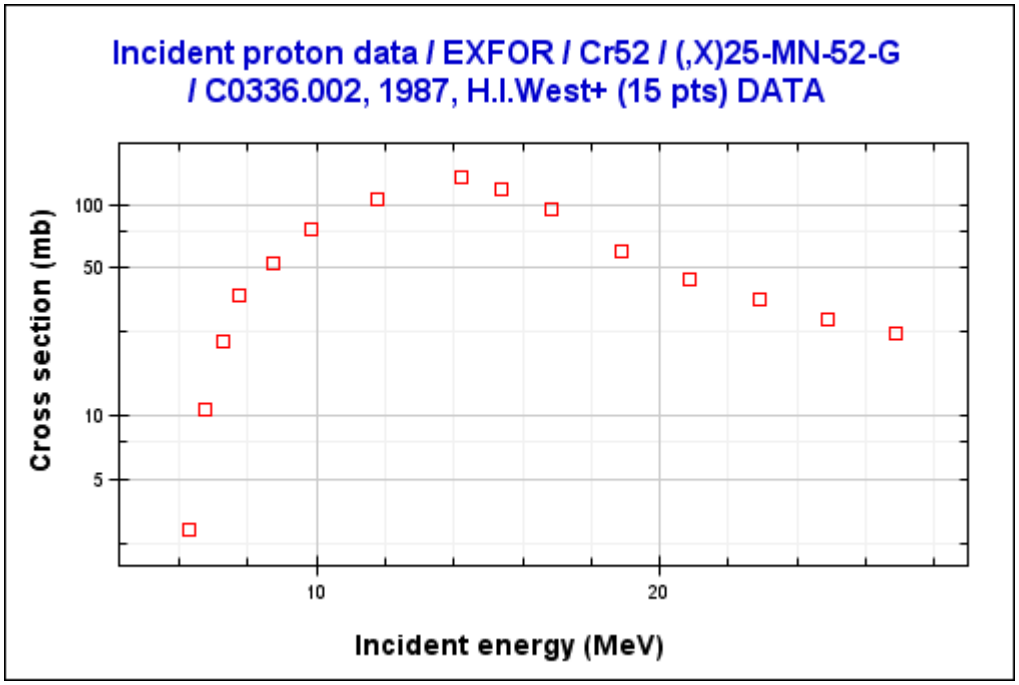

Figure 4: An example of a cross section curve as function of the incoming proton energy measured in MeV, specifically the experimentally measured cross section for the transmutation ^{52}Cr(p,n)^{52g}Mn as measured by West et al.[15].

However, all useful targets consist of many more than one atom per cm^2, and are bulk materials with finite thicknesses. One consequence of this is that the incident particle energy is continuously degraded as the particle travels through the target material. Since the cross section is a function of particle energy (e.g as shown in Figure 4), the probability, P, of a reaction is the integrated cross section with respect to depth in the target material, multiplied by the number of target nuclei, n, within the particle range. Alternatively, the calculation can be recast in terms of an energy integral:

$$P = n \int_{E_{threshold}}^{E_{incident}} \frac{\sigma(E)}{dE/dx} dE$$

In practice this rescaling from incident energy to range can be calculated using a simulation code called SRIM[16], where the stopping power, dE/dx, can be found. Multiplying the above by the incident flux of particles I gives the production rate R, i.e. the number of nuclei produced per second. This number is identical to the saturated yield, A_{sat} which is reached when the rate of production equals the rate of disintegration.

$$R = A_{sat} = nI \int_{E_{threshold}}^{E_{incident}} \frac{\sigma(E)}{dE/dx} dE$$

The total number of produced nuclei N will grow asymptotically towards the saturation level:

$$N(t) = nI\left(1 - e^{-\lambda t}\right) \int_{E_{threshold}}^{E_{incident}} \frac{\sigma(E)}{dE/dx} dE,$$

with $\lambda = {ln2}/{T_{½}}$ and $T_{½}$ being the half-life. λ is defined as the decay constant of the produced isotope, and t as the duration of the irradiation in seconds. In the last equation, it is clear that when $t \gg T_{½}$ it follows, that $\left(1 - e^{-\lambda t}\right) \approx 1$, meaning that the system has approached saturation. This also shows that the time needed to approach saturation, is directly proportional to the half-life of the produced isotope. This has the consequence that the ratios of any co-produced radioisotopes change significantly during longer irradiations, as shorter-lived isotopes might approach saturation, while long-lived isotopes will still increase activity at an almost linear rate (Figure 5). Another property worth noting is that irradiating much longer than one half-life is not very efficient. For every half-life irradiated, the gap to the saturation level is halved, meaning that after one half-life the production yield is 50% of the saturation level. This climbs to 75% after two half-lives, 87.5% after three half-lives etc. [13,14].

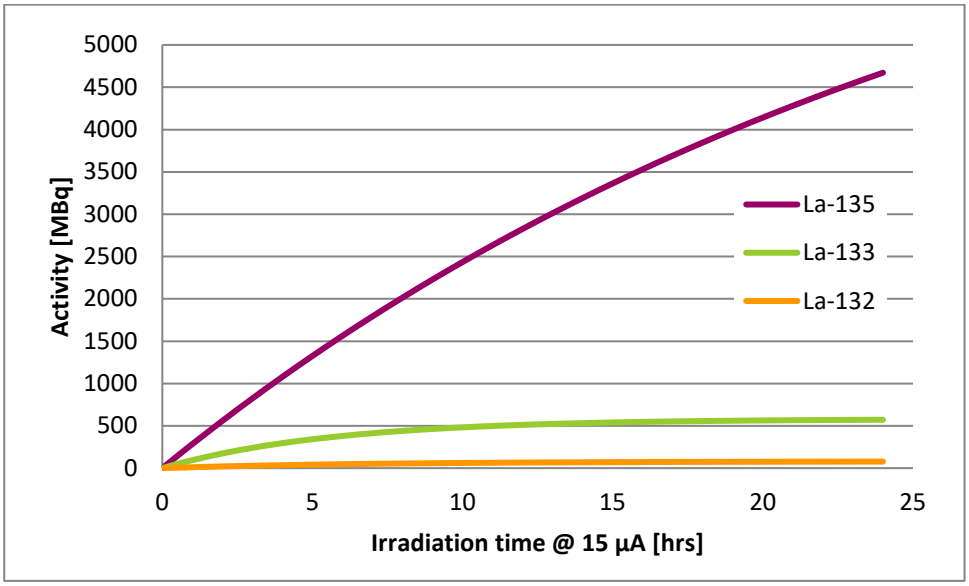

Figure 5: Activity as a function of time of the three main isotopes produced during 15 µA proton irradiation of ^{nat}Ba. Here the effects of half-life on production rates are visible, in that both of the short-lived isotopes ^{132}La and ^{133}La (T½ = 4.8 h and 3.9 h respectively) quickly approach saturation levels, while ^{135}La activity (T½ = 19.5 h) is still increasing.

As mentioned earlier only a small fraction of the incident particles cause nuclear transmutations. An even smaller fraction of the incident energy is consumed in the process. The remaining energy is converted to heat, deposited in the target material. This heat is often the limiting factor for production rates, as the highly localized deposition makes efficient cooling challenging. This imposes restrictions on the applied beam current and thus the production yield.

1.3 Labeling with radiometals

In order to trace a physiological process either the bare radiometal ion can be injected, or more commonly, the radiometal is injected as part of a vector-chelator construct described earlier. The binding of the radiometal is most often achieved using a bi-functional chelator. A chelator is a chemical structure designed to stabilize a metal ion by coordination with strategically placed lone pairs, forming a stable complex while protecting the metal from transchelation and hydrolysis[17].

Bi-functional chelators are chelators with the additional capability of forming covalent couplings to targeting vectors such as proteins, peptides, and nanoparticles. The functional groups for conjugation include NHS-esters and TFP-esters for amide couplings; isothiocyanate for thiourea couplings (Figure 6); and maleimides for thiol couplings. Being composed of modules (i.e. the metal specific chelator and the vector specific functional group for labeling), bi-functional chelators can be tailored for countless numbers of targets, particularly as the number of available vectors constantly increases due to advances in biological research[18].

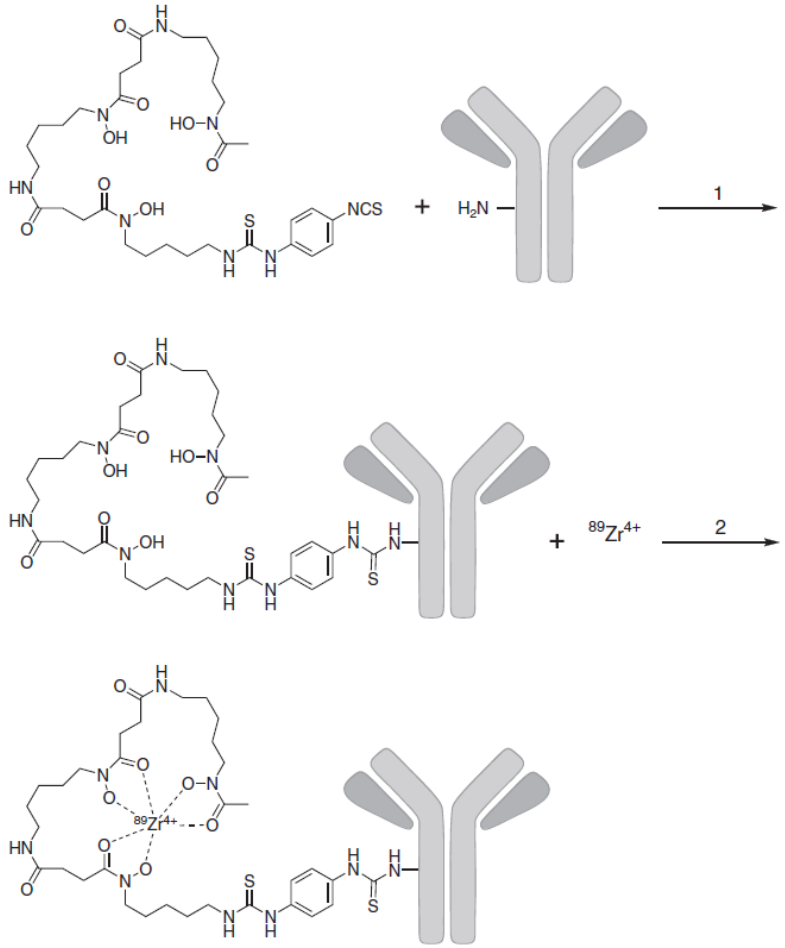

Figure 6: Illustration of the labeling process of an intact antibody with the radiometal ^{89}Zr. First the acyclic chelator DFO is conjugated to the antibody through the reaction of an NCS group on the bifunctional chelator with a lysine side-chain amine. Subsequently the ^{89}Zr is introduced and is complexed by the DFO chelator. Adopted from Vosjan et al. [19]

The structure and physical properties of the chelate complex can however, have pronounced effects on tracer biodistribution, especially with small vectors. Many chelator-metal complexes are highly hydrophilic which can lead to increased renal clearance of the labeled compound. It has been reported that by only changing the chelator, while keeping both the vector and the radiometal the same, the tracer biodistribution can be greatly affected[20]. The overall hydrophilicity of the complex can be determined by measuring the octanol-water partition coefficient (log*P*), and can by addition of hydrophilic or lipophilic moieties, be tuned to optimize the biodistribution[8].

To accommodate stable binding between chelator and radiometal, the donor atom preferences (N, O or S) of the specific radiometal need to be understood. Here, hard Lewis acids like Zr^{4+} and Fe^{3+} are more stably bound by hard Lewis bases like O and N whereas soft acids like Pd^{2+} and Au^{3+} ions are stabilized best by soft bases like S. The coordination geometry, coordination number, and the physical size of the radiometal ion also play important roles in stable chelation[21].

Overall, there are two different types of chelators, cyclic and acyclic. Generally, the cyclic chelators have higher thermodynamic stability. Since they are already largely in the conformation of the complex, the entropic loss during the complex formation is far lower than that of the acyclic chelators. This generally results in higher thermodynamic stability because the higher entropic loss experienced by acyclic chelators is thermodynamically unfavorable[22]. Acyclic chelators however, generally exhibit much faster complex formation and often quantitative chelation of metals even at room temperature, whereas cyclic chelators often require heating for extended periods (60-95°C for 30-90 minutes) to reach optimum labeling yields. Here the acyclic chelators have a great advantage when using short-lived isotopes like ^{68}Ga or when labeling heat-sensitive vectors like proteins and antibodies[22,23].

Radiometal- chelator complexes are rigorously tested and evaluated before use in human subjects and a number of tests have been designed to evaluate the *in vivo* stability of the complexes. If the radiometal dissociates from the radiopharmaceutical, the resulting biodistribution will reflect both the radiopharmaceutical biodistribution and the biodistribution associated with the free radiometal ion[24]. For example, the isotopes ^{68}Ga, ^{85}Sr, ^{89}Zr and the lanthanides will, when released from the complex, accumulate in the bones, whereas the isotope ^{64}Cu is known to accumulate in the liver[25]. The exact distribution of a radiometal ion or the intact compound can be assessed either by dynamic PET, SPECT or by *ex vivo* biodistribution. In the latter the animals are sacrificed at specific time points and the organs of interest are assayed for an accurate determination of uptake, either via well counting or liquid scintillation counting[26,27].

One way of testing the robustness of a radiometal-chelate complex is by challenging it *in vitro*, either with other metal ions, or with different chelators. By using techniques like High Performance Liquid Chromatography (HPLC) and thin layer chromatography (TLC) it is possible to monitor ion exchange and transchelation between the different complexes and metal ions. However, a method closer resembling the real *in vivo* situation is to challenge the complex with biologically relevant mixtures such as blood serum; hydroxyapatite (bone); metal binding proteins like ferritin (metal storage protein), transferrin and other metal transporters; and metal binding enzymes like superoxide dismutase. The stability can subsequently be determined using radio-HPLC or size exclusion chromatography[8].

Once stability of the chelate is achieved, the construct can provide trustworthy information of the biodistribution associated with the labeled compound.

2. Diagnostic isotopes

In order to visualize the distribution of a tracer, the patient is scanned using either a gamma camera for SPECT or a PET camera depending on the isotope used[28]. Today, PET is continuously gaining ground over the conventional gamma camera techniques[29]. The increasing availability of PET-isotope-based tracers from small medical cyclotrons has moved PET from being a preclinical research tool to being a large-scale clinical investigation tool. PET offers both improved sensitivity as well as improved resolution over conventional SPECT imaging[30].

2.1 Introduction to SPECT/PET

In a gamma camera, a collimator is placed between the detector and the source to provide spatial resolution. In this way only gamma rays perpendicular to the detector can be registered. This results in a 2D projection of the activity distribution in the patient. One such projection can be sufficient as in the case of bone scintigraphy. Alternatively, a large number of projections can be combined and a 3D image can be calculated. The former is called a planar acquisition and the latter a SPECT scan (Figure 7).

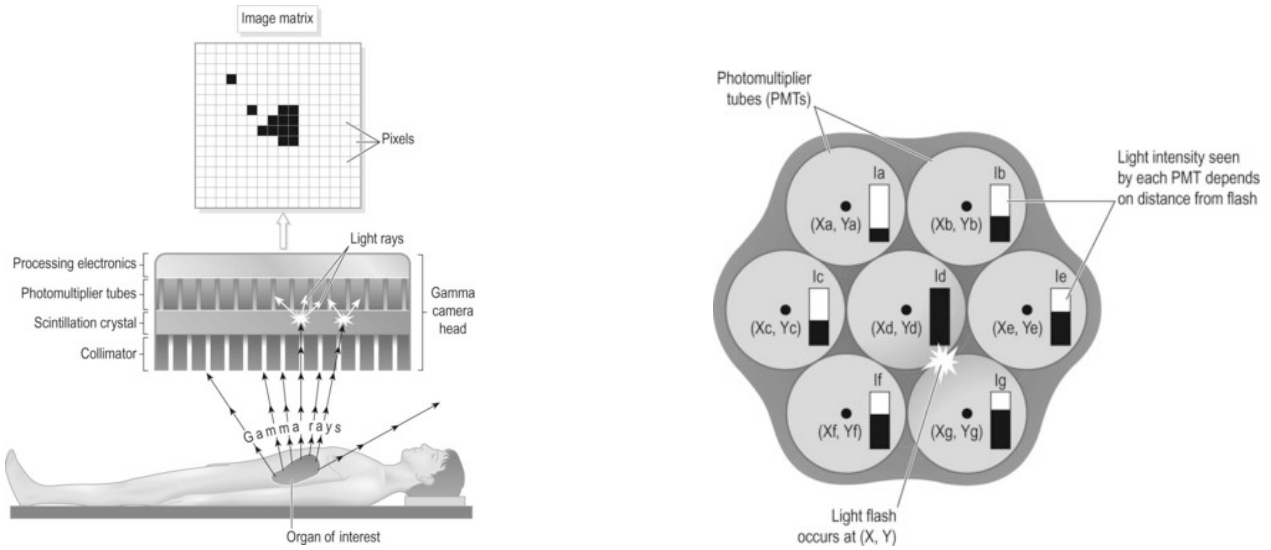

Figure 7: Schematic illustrating the principle of the gamma camera. Gamma photons emitted from the patient are collimated, and produce a current proportional to the gamma energy in the detector. The position of the decay can be calculated by the relative signal ratio from the detectors closest to the scintillation. Adopted from [28]

A PET camera relies on coincidence measurement of the two 511 keV photons created upon annihilation of an emitted positron. When a proton-rich radionuclide decays, it can happen via electron capture (EC) or positron emission (β^+). In the latter, the nucleus reduces its charge by transforming a proton into a neutron, while emitting a positively charged anti-electron called a positron. The ejected positron is slowed down by interaction with atomic electrons and once at rest, annihilates with an electron, converting their combined mass into two 511 keV photons. Due to the need to conserve momentum, the two photons are emitted back-to-back, 180° apart. The 180° angle is the key to the PET technique, seeing that if two 511 keV photons are detected simultaneously, the decay can be assumed to have happened somewhere on the straight line between the two points of detection (Figure 8). Modern cameras provide time of flight (TOF) measurements, further restricting the decay to a 10-20 cm stretch of the straight line. The information is then used to create a 3D image,

either via classic reconstruction methods like those used in SPECT, or more often iterative maximum likelihood algorithms.

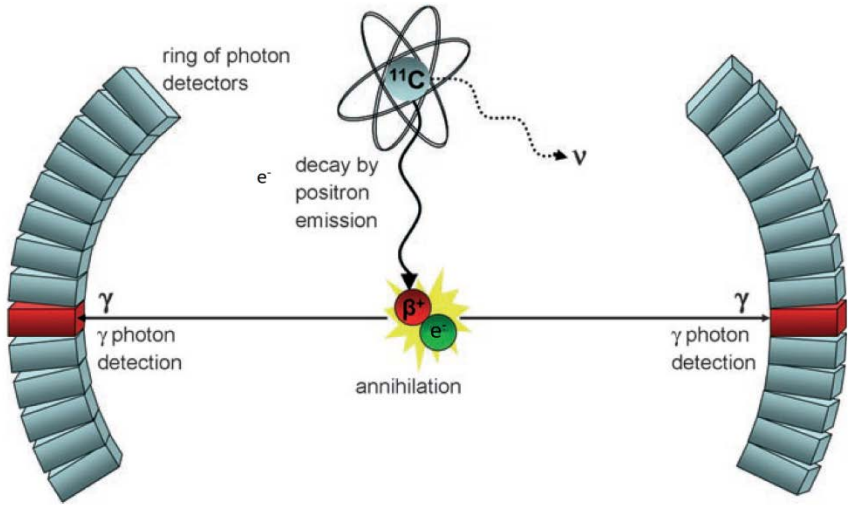

Figure 8: Illustration of the PET imaging principle. Upon decay the PET isotope (here ^{11}C) emits a positron which after traveling a short distance annihilates with an electron to create two 511 keV photons 180° apart. Adopted from Miller et al. [31]

Though the two imaging techniques are quite different, the detection method is the same. In both cases, detection relies on stopping the emitted photons in a scintillation crystal. This produces emission of low-energy photons in the crystal in numbers directly proportional to the energy deposited. To quantify the amount of scintillation light produced and thus the energy deposited, the scintillation crystal is mounted on a photomultiplier tube (PMT). The PMT converts the low number of photons into a measurable current. This conversion is done is several steps. First, the photons encounter the photocathode, a thin cathode on which the photons are converted to electrons via the photoelectric effect. Secondly, the released electrons are accelerated over a series of dynodes each with less negative voltage than the previous. Here each encounter with the dynodes multiply the number of electrons by a factor of 5, resulting in an overall amplification factor on the order of 10^8 at the anode (Figure 9).

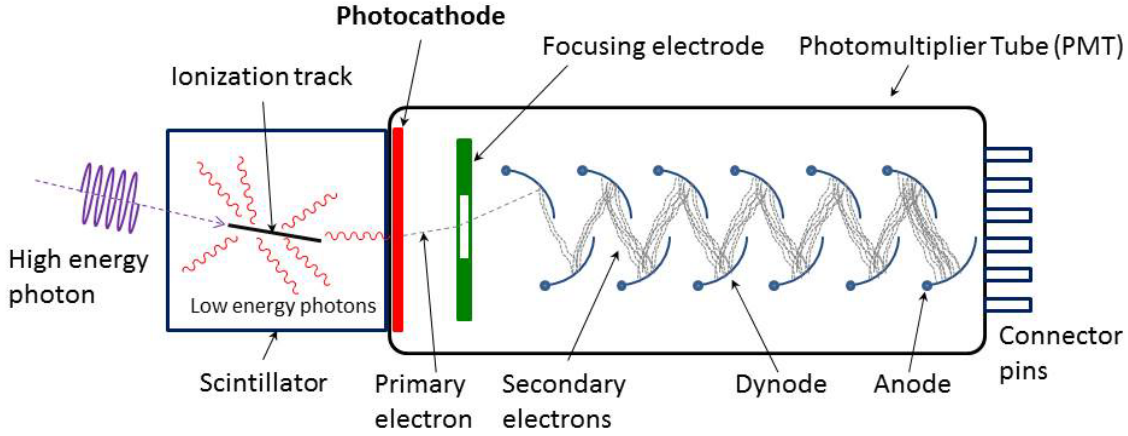

Figure 9 Schematic overview of a gamma detector consisting of a scintillator and a photomultiplier tube. Adapted from Wikimedia Commons.

Each imaging method has benefits of its own. Isotope availability and cost are the main pros for SPECT. SPECT does not rely on a cyclotron and the commonly used isotopes are either available from generators or have half-lives that allow them to be commercially available. PET on the other hand is more expensive and the more commonly used isotopes short-lived with half-lives of less than 2 hours, necessitating either on-site or nearby production. The benefits however are higher sensitivity and superior spatial resolution[32].

Whether the imaging method is SPECT or PET, there is always the tradeoff between image quality and the risk imparted on the patient from the exposure to ionizing radiation. Higher amounts of radioisotopes will, simply due to improved statistics, yield better images and improve diagnostic certainty. To be able to weigh the improved image quality against the increased risk of introducing illness, precise estimates of the associated dose are needed.

2.2 MIRD/OLINDA

Dose estimates are made using the MIRD formalism which describes the dose, D, from one organ, r_S to another r_T as

$$D(r_T \leftarrow r_S) = \tilde{A}(r_S) \times S(r_T \leftarrow r_S)$$

In which $\tilde{A}(r_S)$, also called the cumulated activity, is the total number of decays in the source organ, and $S(r_T \leftarrow r_S)$ is the dose in Gy/(Bq·s). In this way the total dose to an organ, is simply the sum of contributions from all organs and compartments:

$$D(r_T) = \sum_S \tilde{A}(r_S) \times S(r_T \leftarrow r_S)$$

To estimate the risk associated with the imparted dose, the term effective dose is introduced. Here each organ is assigned a tissue-weighing factor w_T based on its radiosensitivity and this weighted dose to individual organs summed:

$$D_{eff} = \sum_T w_T \times D(r_T) = \sum_T w_T \times \sum_S \tilde{A}(r_S) \times S(r_T \leftarrow r_S)$$

The calculated dose in Sievert serves as a measure for the associated risk of developing a deadly cancer, as one Sievert is estimated to increase the risk by 4.1% for healthy adults [33,34]. This risk however, cannot be assumed for patients, as the age distribution and, possibly, the radiation sensitivity of this group is different.

2.3 Choice of diagnostic radionuclide based on target kinetics

When PET tracers are designed, the radionuclide is chosen carefully based on several criteria such as β^+ branch, β^+ energy, associated patient dosimetry, and tracer uptake kinetics. In short, the β^+ branch should be as high as possible. The β^+ energy is proportional to its range in tissue, and higher energy will thus yield lower image resolution. In order to minimize patient dosimetry, radionuclides with many abundant gamma lines are generally avoided and the half-life of the chosen isotope should be matched with the kinetics of the tracer. It should be long enough that there is sufficient activity left to get a signal at the time of optimal biodistribution, while short enough that the isotope does not stay in

the patient long after imaging. A normal compromise between the two is to aim for a half-life similar to or shorter than the time needed to reach optimal uptake.

For this reason, the short-lived isotopes most commonly available, ^{18}F, ^{11}C, and ^{68}Ga are best suited for small molecules and peptides, which in general have a rapid uptake and thus optimal imaging after less than two hours. Larger structures like liposomes, nanoparticles, proteins and antibodies exhibit uptake characteristics that favor imaging on the order of days after administering the tracer.

To get an overview of the dose associated with the different isotopes, we first have to define a benchmark. What we want to know is how much dose a given isotope will impart on a patient per registered event in the PET camera detector. Different vectors are associated with dramatically different timespans before maximum uptake in the target tissue is reached. If the vector reaches optimal uptake in a timespan equaling one effective half-life of the isotope, one would have to administer twice the activity as compared to if the uptake was immediate. The dose would likewise be twice as high if one half-life is waited. The dose is a function of the total number of decays and thus a function of the injected activity and the half-life

$$D \propto N = \frac{A}{\lambda} = \frac{A \times T_{½}}{\ln(2)}$$

Assuming infinite biological half-life i.e. no clearance of the isotopes, the cumulated activity was calculated as a function of time between administration and imaging (t).

$$\tilde{A}(t) = \frac{A \times T_{½}}{\ln(2)} \times e^{\lambda t}$$

To compare not activity but imaging ability, the cumulated activity was normalized to the β^+ branching ratio, $BR_{\beta+}$ of the isotopes.

$$\tilde{A}_{\beta+weighted}(t) = \frac{A \times T_{½}}{\ln(2)} \times e^{\lambda t} \times \frac{1}{BR_{\beta+}}$$

Finally, the associated dosimetry was calculated in OLINDA as a function of the normalized cumulated activity[35]. OLINDA is a software package using the MIRD formalism for dosimetry calculations. Choosing a certain distribution in the body to represent all labeled compounds is not a simple task. It was chosen to use the compartment remaining body, i.e. everything excluding the organs in Table 1. When considering that in this scenario, the time of exposure is the time until optimal uptake, it was deemed a reasonable assumption that the radionuclide would mainly be present in either lymph or blood. Neither of these compartments is available in OLINDA as a source organ and thus are both incorporated in the source organ “remaining body” (RB).

$$D(t) = \frac{A \times T_{½}}{\ln(2)} \times e^{\lambda t} \times \frac{1}{BR_{\beta+}} \times \sum_{T} w_T \times S(r_T \leftarrow r_{RB})$$

Adrenals	Stomach Wall	Muscle	Spleen
Brain	ULI Wall	Ovaries	Testes
Breasts	Heart Wall	Pancreas	Thymus
Gallbladder Wall	Kidneys	Red Marrow	Thyroid
LLI Wall	Liver	Osteogenic Cells	Urinary Bladder Wall
Small Intestine	Lungs	Skin	Uterus

Table 1: Complete list of compartments available in the OLINDA output

The result tells us the dose in mSv per β^+/s at the time of imaging, as a function of time between administration and imaging. The result can be seen in Figure 10 and provides an overview of which radiometal should be chosen based on the uptake time of the tracer in question. From Figure 10 it is evident that for rapidly distributing tracers ^{11}C is superior. If the time of imaging is between 1 and 5 hours after administration ^{18}F has the lowest associated patient dose followed by ^{45}Ti, which is the better choice up to the point of 10 hours. From 11 to 60 hours ^{64}Cu is the favorable, followed by ^{89}Zr for times larger than 60 hours, followed by first ^{124}I and then ^{52}Mn at very late time points.

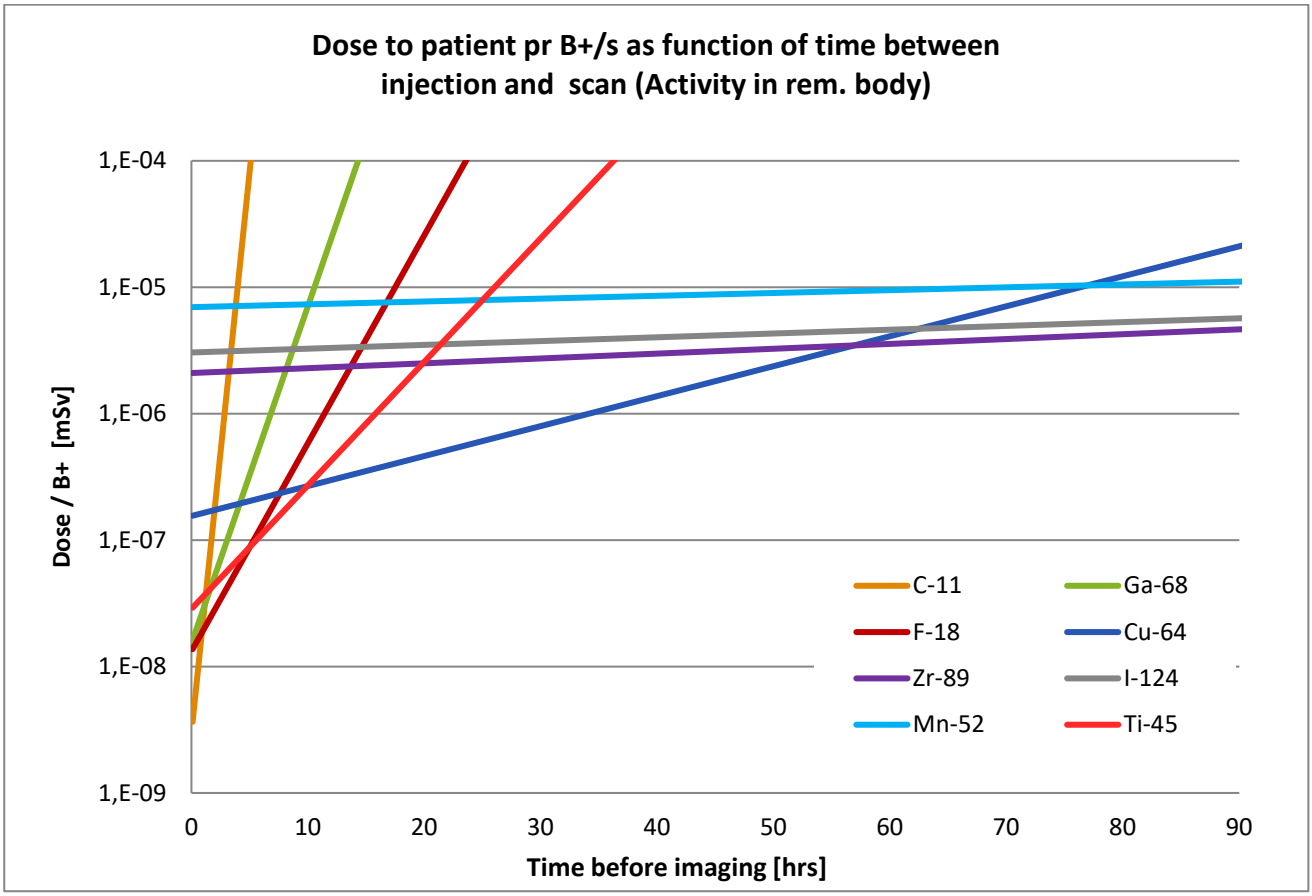

Figure 10: Effective dose to the patient per β^+/s at the time of imaging as a function of time between tracer administration and imaging.

Notice how it is critically important to consider the effect of distribution, before choosing the isotope. The fact that the compartment "remaining body" is not associated with a tissue-weighing factor in the OLINDA/MIRD formalism, will result in the radiation deposited locally, i.e. in the same compartment, not being factored into the calculated dose. This means that the dose from electron emissions (β+, β-, Auger-electrons, and conversion electrons) as well as low energy x-rays are underestimated in the

dosimetry as compared to gamma emissions. Placing the activity in a very sensitive organ gives a picture of the upper limit to the underestimation. The testes, being very sensitive organs, are chosen to exemplify the effect. This organ not only has very high radio sensitivity, it is also a very small target. These two factors combined will overestimate the contribution from β+, β-, Auger-electrons, and conversion electrons as compared to the contribution from gamma emissions. The result can be seen in Figure 11. Interestingly this indirect change in the weighting of the different types of emissions changes the relative dose of especially the longer-lived isotopes. The order of nuclides showing the lowest dose for the source organ "remaining body" is $^{11}C \rightarrow {}^{18}F \rightarrow {}^{45}Ti \rightarrow {}^{64}Cu \rightarrow {}^{89}Zr \rightarrow {}^{124}I \rightarrow {}^{52}Mn$. Using the source organ "testes" the order is $^{11}C \rightarrow {}^{18}F \rightarrow {}^{45}Ti \rightarrow {}^{64}Cu \rightarrow {}^{89}Zr \rightarrow {}^{52}Mn \rightarrow {}^{124}I$.

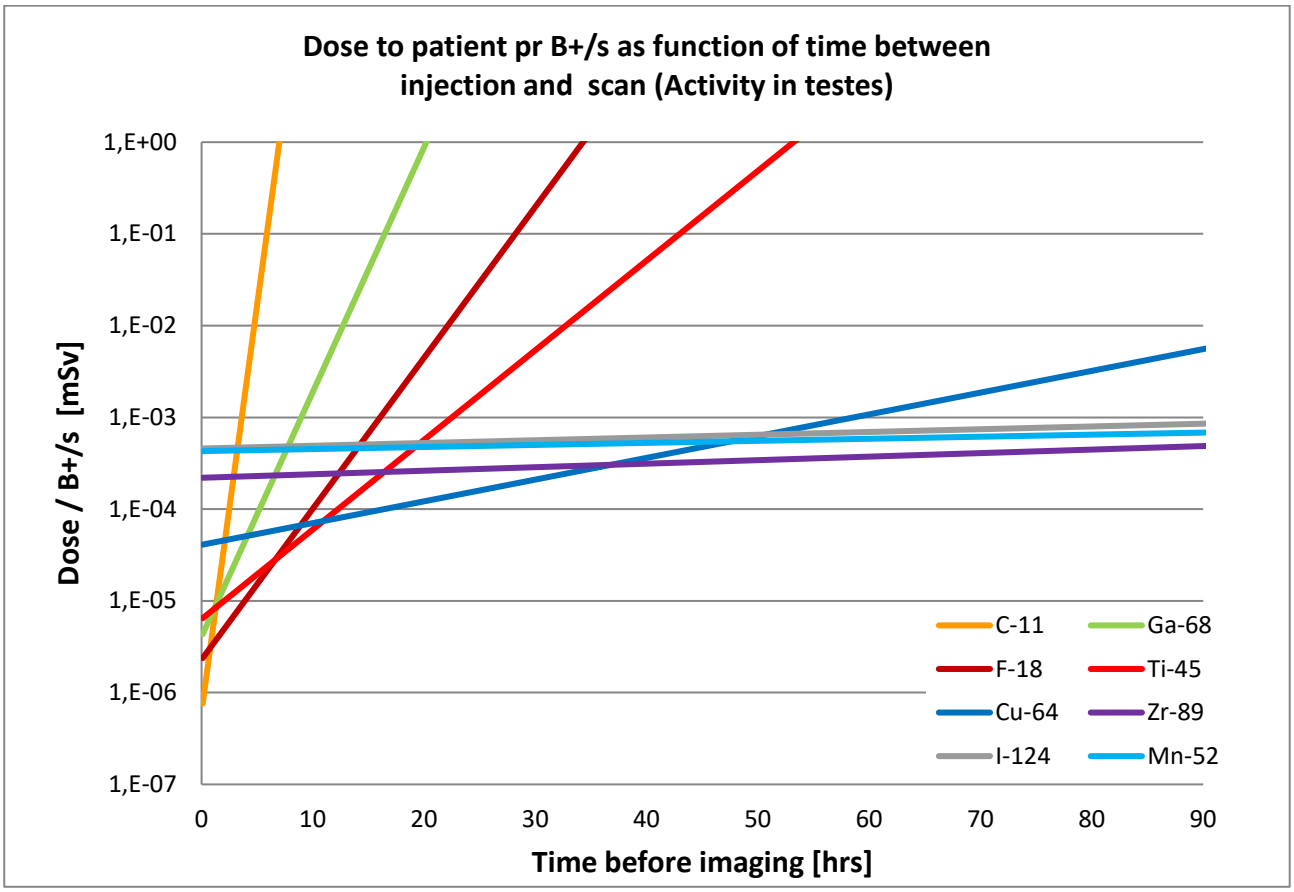

Figure 11: Effective dose to the patient per β⁺/s at the time of imaging as a function of time between tracer administration and imaging when the activity is only in the testes.

The situation in which the entire administered radioactivity is sitting in the most radiosensitive organ is of course highly unlikely, but the example shows the dramatic difference in tracer dosimetry, the biological distribution can induce. It further shows how an isotope cannot simply be labeled as "giving high dose". To optimize dosimetry, imaging cancers, calls for isotopes with low abundance of concurrent gamma emissions, whereas tracing physiological processes in healthy radiosensitive organs, favors isotopes with low β^+ energy.

There are of course other considerations than just the associated dosimetry, when choosing the radionuclide. Image resolution for one is important, especially when performing studies in small animals. The main parameter determining image resolution, besides the intrinsic properties of the

scanner, is the energy of the emitted β^+. The range in tissue is proportional to mean β^+ energy, $\bar{E}_{\beta^+}$ and is approximated [36] as

$$Range\ [cm] \sim \frac{\bar{E}_{\beta^+}\ [MeV]}{2}$$

Another parameter affecting the resolution is the amount of noise introduced by high energy gammas. These contribute with counts in the 511 keV energy window via scattering or their incomplete absorption in the camera detectors. This introduces false coincidences leading to a higher image background.

Though resolution and dosimetry are often the deciding factors when picking the right radionuclide, this is only an option if the isotope is used in its bound/chelated form. When, for example, tracing inherent properties of metal ions, the isotope used cannot simply be interchanged with another element. Here the isotope must be of either the same element as the one examined or one mimicking its behavour. Examples of these are many: ^{82}Rb for example, beeing a group 1 element can be used as a potassium mimic and being a substrate for the Na^+/K^+-ATPase it is is transported into the myocardium and its resulting distribution, maps the myocardium perfusion[37]. In therapy the isotope ^{223}Ra, being a Ca mimic, is used to treat bone metastasis, exploiting the accumulation of Ca in bone mineralization[38]. And as discussed in the next section, the isotope ^{52}Mn, likewise serving as a Ca mimic can be used among other things to image neural tracts, exploiting the ability of Ca to be transported along bundles of nerve cells in a neural activity-dependent manner.

3. Projects based on diagnostic isotopes

The aim of the work on diagnostic radioisotopes was to develop the long-lived PET radiometals: ^{52}Mn, ^{89}Zr, and ^{45}Ti:

3.1 Manganese-52

Interest in ^{52}Mn-based PET applications has dramatically increased over the last years. A driving motivation has been the advances in Manganese Enhanced MRI (MEMRI) where Mn^{2+} serves as a potent T1-shortening contrast agent[39,40]. Although promising, the MRI techniques are severely limited by the toxicity of manganese, the effects of which are well documented due to decades of chronic exposure to workers in the smelting industry. Here toxicity manifests itself in neurodegenerative disorders, prominent among these as Parkinson's disease[41–43]. This prohibits clinical use of most preclinical MEMRI techniques. The superior sensitivity of ^{52}Mn PET however, allows very low amounts of manganese administered and thus completely circumvents toxicity issues. ^{52}Mn-PET provides analogous information to MEMRI but with higher sensitivity and thus potentially allows clinical application of the historically MRI-based techniques in a PET setting.

The applications of ^{52}Mn are many: Mn^{2+}, mimicking Ca^{2+}, accumulates in areas of neuronal activity via activity dependent uptake through voltage gated Ca^{2+} channels. Having the ability to cross synaptic clefts, $^{52}Mn^{2+}$ can be used to visualize the bundles of nerve cells interconnecting different regions in the brain (neural tracts)[39,44]. Another prominent use is ^{52}Mn based cell tracking in which the Ca^{2+} channels and metal transporters are exploited to incorporate Mn^{2+} into cells *in vitro*, prior to administration[45–47]. Using ^{52}Mn-based PET, allows longitudinal and non-invasive assessment of location, dynamics and survival of transplanted cells, providing knowledge critical to translation into clinical use[48]. In addition, it has been established that manganese enters active beta cells in the islets of Langerhans. Using ^{52}Mn could possibly provide a non-invasive measure of the functional beta cell mass during the progression of diabetes[49]. Such information would allow monitoring of early disease progression and treatment response.

Despite the many applications utilizing the unique properties of ^{52}Mn, separation methods are underdeveloped. Published methods for separation of ^{52}Mn from the Cr target material, include both anion and cation exchange based methods, precipitation based methods and liquid-liquid extraction based methods[48,50–53]. However, the high dose-rate associated with ^{52}Mn does not allow extensive manual handling a fact complicating the use of both liquid-liquid separation and precipitation. Solid phase extraction-based methods (SPE) typically require less handling and have the further benefit that they are typically easily automated. The published SPE-based methods suffer from either large losses of ^{52}Mn[48], large elution volumes[51] or very time consuming[50].

Due to the established need for ^{52}Mn, the goal of our project was to facilitate and promote the use of ^{52}Mn, by developing an SPE-based methodology for production of high specific activity ^{52}Mn, identify a suited chelator for *in vivo* applications and optimize the labeling conditions.

^{52}Mn properties

^{52}Mn is one of three positron emitting manganese isotopes, the others being ^{51}Mn and ^{52m}Mn. Of the three ^{52}Mn has the longest half-life (5.591 days vs. 46.2 mins and 21.1 mins respectively) and by far the lowest β+ energy (244.6 keV vs. 970.2 keV and 1179 keV respectively), providing high resolution

PET imaging over extended time periods. It furthermore has a high β+ branch of 29.6% compared to that of other long lived PET isotopes like ^{89}Zr and ^{124}I both having 22.7%[54–57]. This makes ^{52}Mn a great choice not only when tracing the biological properties of Mn but also whenever a radiometal for longitudinal high-resolution PET is needed (Figure 12).

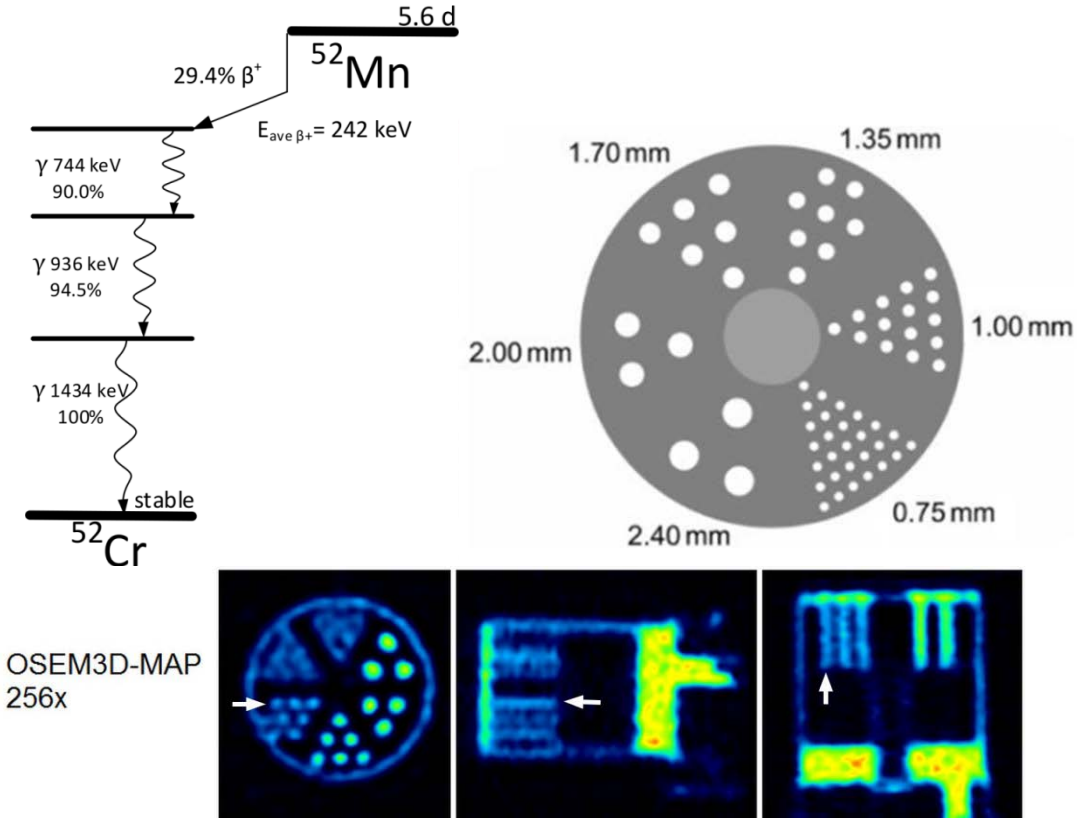

Figure 12: Top left: A simplified decay scheme for ^{52g}Mn[54]. Top right: A schematic cross section through a Derenzo-type phantom showing arrangement and diameters of the rod volumes – adapted from Scuffham et al., 2012. Bottom: PET images of the phantom with ^{52}Mn solution are shown in the coronal, sagittal, and axial directions – from Napieczynska et al., 2017. The arrow shows the 1.35 mm rods clearly resolved.

^{52}Mn production

The production of ^{52}Mn is done via proton irradiation of ^{nat}Cr which is composed of 83.8% ^{52}Cr, 9.5% ^{53}Cr, 4.3% ^{50}Cr and 2.4% ^{54}Cr. ^{52}Mn is produced primarily via the ^{52}Cr(p,n)^{52}Mn reaction with a small contribution from the much less abundant ^{53}Cr via the ^{53}Cr(p,2n)^{52}Mn reaction. While the ^{50}Cr content only gives rise to the very short-lived ^{50}Mn the ^{54}Cr will yield co-production of the 312 day half-life ^{54}Mn. The production ratio ^{54}Mn/^{52}Mn is energy dependent and estimated to be approx. 0.1-0.4%.

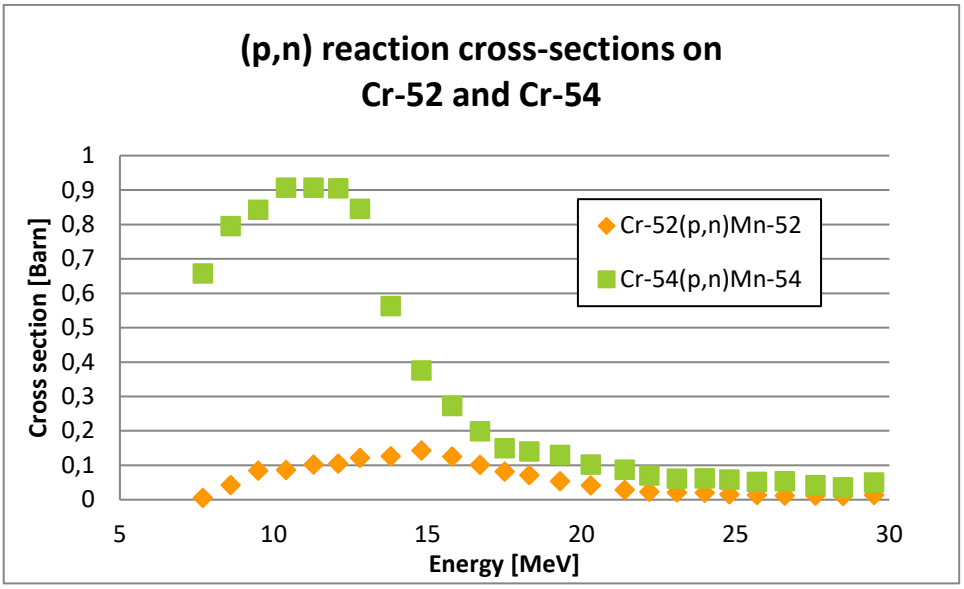

Figure 13: The experimental cross section for the reactions ^{52}Cr(p,n)^{52}Mn and ^{54}Cr(p,n)^{54}Mn as published by Levkovski et al[58]

Detailed work on the reaction cross sections of the ^{nat}Cr(p,x)^{52}Mn channels have shown how this route of production is easily capable of providing sufficient amounts of ^{52}Mn activity for imaging purposes (Figure 13)[51,59]. Looking at the ratio between the cross sections for the reactions ^{52}Cr(p,n)^{52}Mn and ^{54}Cr(p,n)^{54}Mn it is evident that allowing the beam to exit the Cr target with an energy of approx. 14 MeV will significantly decrease the relative amount of co-produced ^{54}Mn (Figure 14).

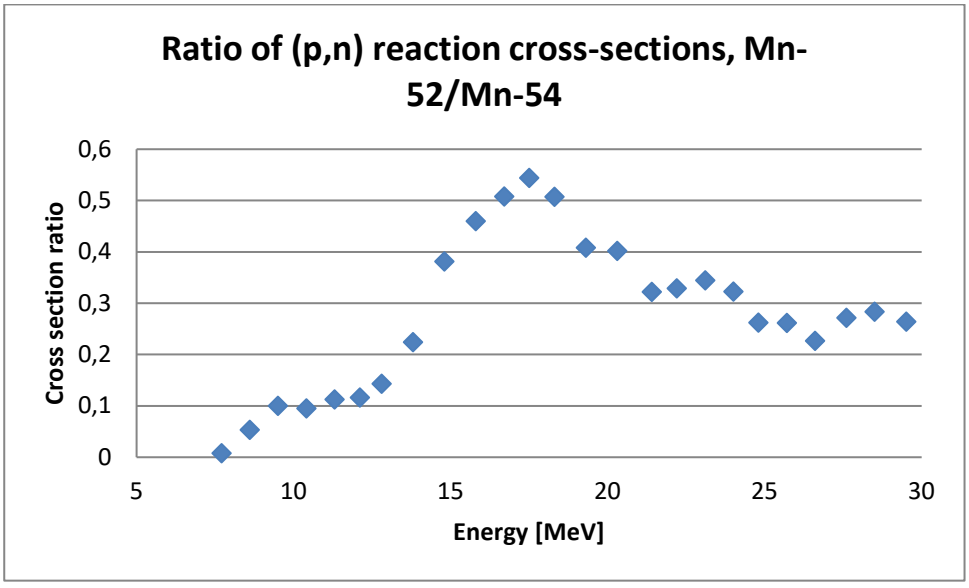

Figure 14: The ratio of 52/54 cross-sections, shown individually in Figure 13. It is seen that the production ratio peaks at approx. 17.5 MeV and decreases dramatically at energies below 14.8 MeV.

On a 16 MeV cyclotron, this would severely reduce the produced amounts of ^{52}Mn, and we therefore elected to not sacrifice production yield over radionuclidic purity. On a cyclotron providing higher energy protons, the effect on the production rate would not be as detrimental.

The chromium targets used were produced by pressing chromium metal powder onto the surface of silver discs. This was done using a mechanical press at pressures exceeding 75 kN/cm^2 in order to get the chromium powder to form an adherent and smooth surface (Figure 15). For a period of time chromium foils were used instead of powder, but the high chemical resistance of chromium caused subsequent target dissolution in HCl to be very slow as compared to the powder targets.

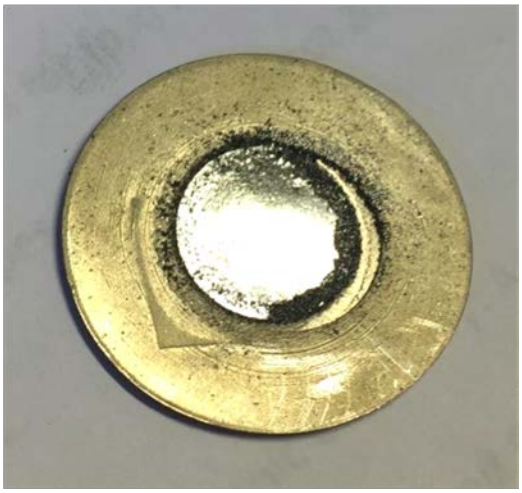

Figure 15: A Cr target: The chromium powder starts forming a smooth surface at applied pressures above 75 kN/cm^2.

The irradiation itself is straightforward as the chromium target material has a high melting point (2180 K) and high thermal conductivity (93.9 W/m·K) allowing high beam currents over extended time. Here, the chromium on silver target was simply covered with either a 100 µm Al foil or a 25 µm Nb foil, placed in a target holder providing water cooling on the rear face of the silver disc, and irradiated at a beam current of 20 µA. The cover foil slightly degrades the incident beam energy with an energy loss of ~0.6 MeV for 100 µm Al and ~0.4 MeV for 25 µm Nb, but is necessary to prevent contamination of the cyclotron in case any sputtering occurs.

Mn chemistry

Manganese can exist in a multitude of oxidation states (II, III, IV, VI and VII) with Mn(II) being both the most stable and abundant. In neutral or acidic aqueous solution this state exists as the pale pink hexaaqua ion $[Mn(H_2O)_6]^{2+}$. The water molecules are difficult to exchange and the formation constant for halogeno complexes is thus very low. However when ethanol or acetic acid is used as solvent, anionic MnCl complexes like $MnCl_3^-$, $MnCl_4^{2-}$, $MnCl_6^{4-}$ and $Mn_2Cl_7^{3-}$ are formed. Chromium on the other hand, having notoriously slow ligand exchange, does not rapidly adopt anionic form under these conditions and separation of the produced ^{52}Mn from the ^{nat}Cr target can thus be performed on anionic exchange resin from HCl-ethanol mixtures [60,61].

Little has been published on chelation of Mn^{2+} using the common cyclic chelator DOTA. This is due to the two main angles of interest that Mn^{2+} receives. Firstly, due to the toxicity of manganese, most published work on chelation of manganese is based on the attempt to provoke clearance of ingested manganese from the body. In this discipline rapid complex formation is a necessity and the focus is therefore solely on acyclic chelators. Of these DTPA seems to fare the best[62–64]. Secondly, a lot of

interest in Mn^{2+} chelation has been in the context of producing Mn-based Magnetic Resonance Imaging (MRI) contrast agents. For this purpose, coordinated water molecules are necessary, and the absence of these in DOTA effectively reduces the relaxivity value of the complex rendering it useless as a contrast agent. Though one study shows high inertness of the Mn-DOTA complex no serum stability or labeling optimization has previously been published[65,66].

Introduction to the ^{52}Mn projects in this thesis

The work mainly consists of two papers describing the development of the production, separation and labeling methods for ^{52}Mn. The two papers combined provide all the information needed in order to set up production of ^{52}Mn on a medical cyclotron, perform high specific activity separation and labeling.

3.1.1 Paper I

The first paper "Novel Preparation Methods for ^{52}Mn for ImmunoPET Imaging" describes the trap and release based separation method based on extraction of manganese chloride species from ethanolic HCl. It further provides imaging based biodistribution of the ^{52}Mn labeled antibody ^{52}Mn-DOTA-TRC105 as well as of the "free" ^{52}Mn ion. Comparison of the two biodistributions indicates stability of the ^{52}Mn-DOTA complex *in vivo.*

3.1.2 Paper II

The second paper "Optimized procedures for manganese-52: Production, separation and radiolabeling" sought to optimize the production method and to answer some of the questions left open in the first paper. The paper introduces an extra column in the separation to reduce the amount of cobalt, copper, zinc and iron in the purified ^{52}Mn. These are all competitors for DOTA and removal is imperative for high specific activity labeling. Furthermore, reaction conditions with DOTA were optimized and the serum stability of the complex was investigated.

3.1.3 Paper III

The third ^{52}Mn paper investigates the potential of ^{52}Mn as a neural tract tracer. This project was conducted in cooperation with Eberhard Karls University Tubingen, Germany. Rats were injected with ^{52}Mn in one of two compartments in the brain and the transport of the tracer was visualized using PET/MRI upon stimulation. The administered dose was further optimized such that no cell damage was observed. The submitted manuscript "Imaging Neuronal Pathways with ^{52}Mn PET. Toxicity Evaluation in Rats" is attached.

3.1.4 Other ^{52}Mn-based work

Several other investigations have been carried out using ^{52}Mn over the duration of the thesis work. As part of the MATHIAS project ^{52}Mn labeled antibodies were produced. This was done to study the translocation of the antibody into the lung. The mechanism by which iv.-administered antibodies reach their target in the lung lumen is not well understood. Previously reported high and fast uptake of aspergillus-specific antibodies in the infected lungs of neutropenic mice[6], could be a consequence of the radioisotope not being properly bound to the antibody and simply taken up by the *A. Fumigatus* upon release from the construct [67]. This argument is further supported by the high uptake in the liver, which is often a signature of unstably-bound ^{64}Cu (the isotope used in [6]). Injecting the labeled antibody prior to infection should allow imaging of the circulating labeled antibody with minimum uptake in lung or liver until the animal is infected. This would prove stability of the radiolabeled

antibody and thus show translocation of the intact structure to the lungs upon infection. This experiment not only displays the late time-point imaging capabilities of ^{52}Mn but also validates the radiochemistry used in the previous experiments. Although several labeling tests of the antibody had previously been performed both at DTU and in Tubingen, the labeling was unsuccessful on the day of the animal trials. The project is therefore still ongoing awaiting a second attempt. Inductively Coupled Plasma Optical Emission Spectrometry (ICPOES) analysis of the ^{52}Mn used in the failed attempt later showed a significant Zn contamination of > 600 ng/MBq.

Discussion

The first paper clearly demonstrates the concept of Mn extraction from the semi-organic solvent. The improvements in the second paper are:

1. The pressed powder target, minimizing the time required to dissolve the Cr target material
2. Reduced loss of activity in the separation process
3. The introduction of a remediation column removing cobalt, copper, zinc and iron. These are all potential competitors for subsequent labeling.
4. The optimization of labeling conditions with DOTA
5. The demonstration of serum stability of the complex

However, the amount of residual Cr in the purified Mn was slightly higher than what is reported in the first paper. During the development of the method, it was observed on more than one occasion that the ^{52}Mn did not trap efficiently on the column. To remedy this, the resin mass on the first column was increased and the flow over the columns was reduced from approx. 10 mL/min to approx. 2 mL/min. Though we never saw inefficient trapping after this change, it may have introduced another issue. Ligand exchange to chloride in the acid/ethanol is not necessarily exclusive to Mn and may only be limited by the notoriously slow exchange for chromium complexes[60]. This means that by changing the flow-rate and thus the time spent in the semi-organic solvent, more chromium may have formed anionic complexes and adhered on the column along with the manganese, resulting in a lower separation factor. A possible solution could be to use a longer column to ensure quantitative trapping while simultaneously using a high flow-rate over the column. This was tested in a recent ^{52}Mn production. When eluting the first column, the elution was inefficient at the higher flow-rate of ~10 mL/min when only using 1 mL of 0.1 M HCl. After waiting approximately 5 minutes the column was eluted with another 1 mL of 0.1 M HCl. The first elution was almost uncolored, and the second elution was bright green. This clearly indicated that trapped chromium complexes exchanged ligands to become cationic during the 5-minute timespan, and eluted in the second 1 mL aliquot.

The translation to clinical use is difficult because of the dosimetry of ^{52}Mn. Three high-abundance, high-energy gamma emissions accompany the decay of ^{52}Mn, resulting in very high gamma dose to patients (Figure 10). Some applications of ^{52}Mn can possibly be performed using ^{52m}Mn instead, which can be made available in a ^{52}Fe based generator system[68]. ^{52m}Mn has an only 21.1 m half-life complicating labeling and prohibiting labeling of large molecules, but is in some settings sufficient for tracing Mn^{2+}.

3.2 Zirconium-89

Having near ideal properties for imaging of intact antibodies and other slowly distributing vectors, ^{89}Zr is receiving growing interest both for preclinical and clinical investigations[69–71].

^{89}Zr Properties

The half-life ^{89}Zr of 78.4 hours matches the biodistribution of intact antibodies commonly showing optimal distribution 3-5 days post administration[72]. ^{89}Zr furthermore has a 22.7% β^+ branch, and average β^+ energy of only 396 keV, allowing high-resolution PET imaging[56]. Complicating, but not prohibiting, clinical use is the dosimetry associated with the 99% abundant 909 keV gamma emission from the ^{89m}Y daughter (Figure 16).

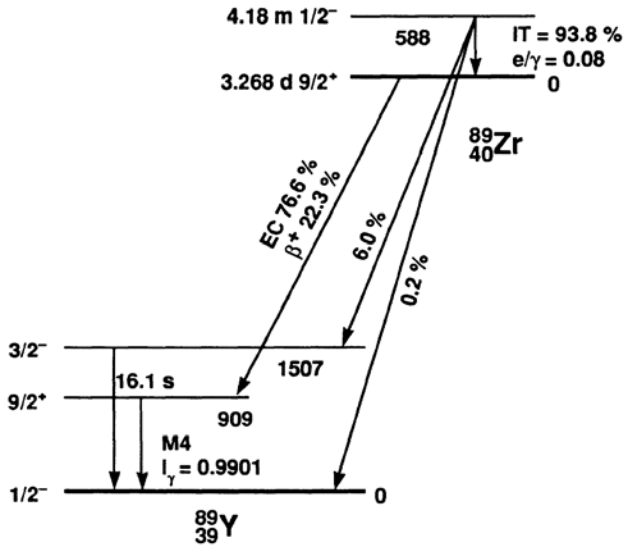

Figure 16: Simplified decay scheme of ^{89}Zr. Adapted from Mustafa et al.[73]

^{89}Zr Production

^{89}Zr is produced via the (p,n) reaction on the naturally monoisotopic ^{89}Y in high yields with a cross section approaching 800 mb at 13.8 MeV, which is an energy available on most medical cyclotrons. Incident energy is however commonly reduced below this energy to completely avoid coproduction of the two long-lived radioisotopes ^{88}Y (T½ = 106.6 days) and ^{88}Zr (T½ = 83.4 days)[74]. Still, high production rates are available with reported yields of > 50 MBq/μAh[75].

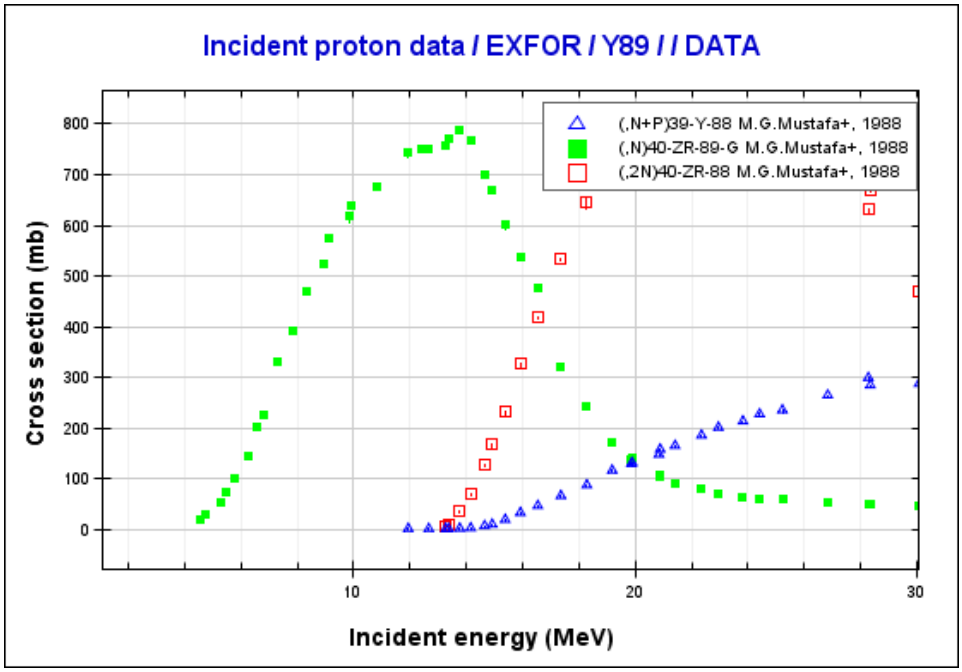

Figure 17: Cross section data for the reactions ^{89}Y(p,n)^{89}Zr, ^{89}Y(p,2n)^{88}Zr and ^{89}Y(p,pn)^{88}Y showing the potential for coproduction of long-lived contaminations. Experimental data adopted from Mustafa et al.[73]

For this thesis, activity was produced by proton bombardment of yttrium foils. These 640 µm thick, 5 mm × 5 mm foils were cut and sandwiched between a silver disc and a 500 µm Al degrader and placed in the target holder, providing direct water cooling on the rear face of the silver. Based on SRIM calculations[16] the Al foil degrades the incident proton energy from the nominal 16.5 to approx. 13.1 MeV, bringing the energy below the threshold for co-production (<100µb) of both ^{88}Y and ^{88}Zr (Figure 17). Even though thermal conductivity is not very high (17.2 W/(m·K)) the target was expected to withstand high irradiation currents because of the very high melting point of yttrium (1799 K). However, it was seen on several occasions that the yttrium foil was tarnished at the beam strike, looking slightly burnt even at beam currents of 15 µA. This is most likely a consequence of very poor heat conduction in the interface between the Y foil and the silver disc. Seeing that the Y foil was cut using scissors it was never perfectly flat, possibly causing a partial gap between the yttrium and silver. If much higher beam currents are needed a way to circumvent this, would be to press the yttrium onto the silver using a mechanical press. With both yttrium and silver being soft metals, they would easily join and form an interface of increased thermal conductivity.

Zr Chemistry

The aqueous chemistry of Zr is extensive. The principal oxidation state is 4+ but there is no indication of Zr^{4+} or ZrO^{2+} (the zirconyl ion) existing freely under any conditions in solution. In hydrochloric acid solutions the dominant species is the trinuclear $[Zr_3(OH)_6Cl_3]^{3+}$ as well as some amount of $ZrOCl_2{\cdot}8H_2O$. Zr^{4+} is a very hard Lewis acid, and highly oxophilic, and therefore forms very stable complexes with oxalate. Zr^{4+} is commonly stabilized in solution by oxalate and here considered to be in the form of $[Zr(C_2O_4)_4]^{4-}$ [60,76].

Separating the produced ^{89}Zr from the bulk ^{89}Y target material was performed according to the method developed by Meijs et al. [75,77]. In brief, ^{89}Zr was separated from ^{nat}Y by solid phase

extraction using approximately 100 mg of hydroxamate resin, prepared by functionalizing the carboxylate groups of the commercially available, silica-based Waters Accell™ plus CM weak cation exchange resin[77–79]. First, the bombarded yttrium foil was dissolved by addition of 6 M HCl and the solution was diluted with water to ensure a final concentration of less than 2 M HCl. The solution was passed over 100 mg of hydroxamate resin, which had been prewashed with 8 mL of MeCN, 15 mL of water and 2 mL of 2 M HCl, in that order. After loading, the resin was washed with 10 mL of 2 M HCl and then 10 mL of water to remove residual yttrium ions and any other impurities present. Finally, the activity was eluted in a small volume of 1 M oxalic acid.

3.2.1 Specific activity

To assess the molar activity of the purified ^{89}Zr, ICPOES analysis was performed on a single batch from 2016. The sample was prepared by diluting 100 µL of 1 M oxalic acid containing 9.7 MBq of ^{89}Zr to a total volume of 10 mL with 0.3 M HCl. Analysis showed 4.36 ppb of Zr per MBq of ^{89}Zr. Recalculating the activity to end of bombardment, this corresponds to 0.51 ng/MBq at time of production and a specific activity of 174 GBq/µmol. This corresponds 11.9 % of theoretical molar activity.

3.2.2 Oxalate-free labeling

During the last 2 years we made several attempts to establish a labeling strategy independent of oxalic acid. We had issues with the metalloprotein ASIS (an activity inhibited version of coagulation factor seven – see section starting page 57) losing its activity and stability after ^{89}Zr-labeling with oxalate present. ASIS has in its folded conformation several Ca-atoms incorporated. We believe the observed loss of activity is due to the insolubility of Ca-oxalate, and oxalate thus depleting the Ca binding pockets, rendering the protein unstable. Preliminary data showed that sucrose was efficient in re-dissolving dry zirconium chloride and we therefore elected to determine whether it was also efficient in stabilizing Zr^{4+} in solution[67]. This would serve to facilitate labeling of metalloproteins with ^{89}Zr.

Three different labeling methods were used and the result of each was tested using an in-vitro cell-binding assay. The standard oxalate containing method described by Vosjan et al. was tested against one using sucrose as a stabilizer and one without stabilizer [19].

^{89}Zr in HCl was taken to dryness in three vials and re-dissolved in oxalic acid, saline and sucrose. pH was adjusted to 7.0 with 0.5 M HEPES and the dissolved activity was transferred to the DFO-conjugated protein. The labeling was performed at 37 °C for 80 min. At this point all three reactions showed > 95 % completion on radio-TLC (Figure 18). In this TLC system un-chelated ^{89}Zr will complex with citrate in the eluent and move with the eluent front, while labeled protein stays at the spot. DTPA was added to all three to remove any un-specifically bound ^{89}Zr and after another 15 minutes, the mixtures were transferred onto PD-10 size exclusion columns.

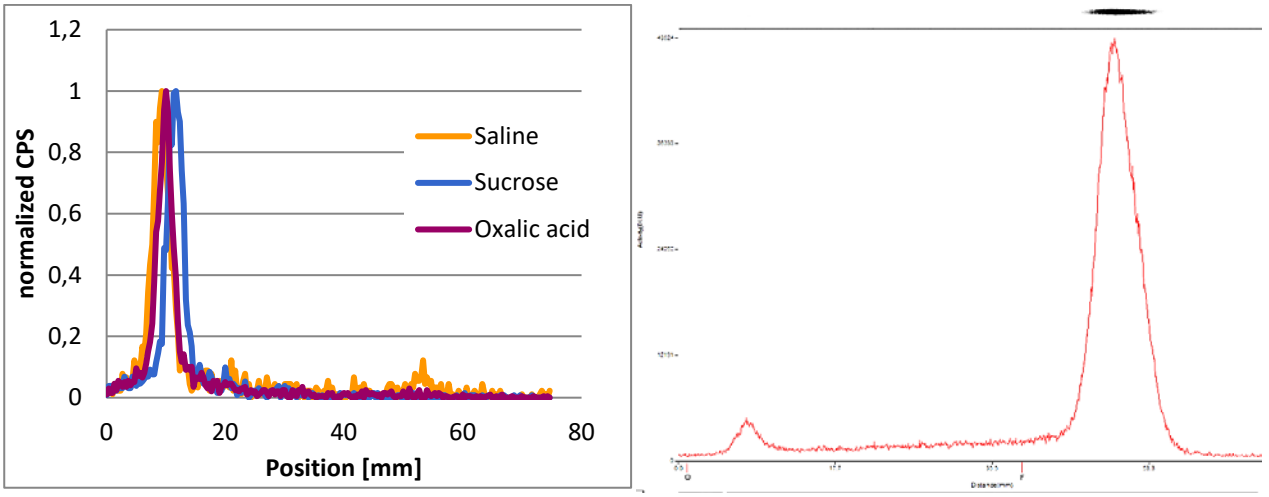

Figure 18: Left: Normalized radio-TLC data showing the reactions after 80 min at 37°C. Right: Unlabeled ^{89}Zr elutes with the eluent front. The reactions thus show more than 95% of the available ^{89}Zr bound to the protein.

From the data in Table 2 it is evident that the oxalic acid is superior to both the sucrose and the saline in terms of re-dissolving the dried down zirconium/zirconyl chloride. Contrastingly, data from PD-10 purification indicates that the labeling is most efficient in sucrose.

	Dissolution yield [%]	PD-10 yield [%]	Total Labeling yiel [%]
Oxalic acid	100	69	69
Saline	46	63	29
Sucrose	47	81	38

Table 2: Table summarizing the apparent radiochemical yields obtained in the three different labeling approaches. Further analysis showed dramatically different yields for the "Saline" and the "Sucrose" methods.

However, when the labeled protein is analyzed with HPLC (Reverse-phase C4 gradient; 0.1% TFA in H2O: 0.1% TFA in MeCN) the picture looks different. Only the protein labeled in the presence of oxalic acid showed a coinciding peak on the radio and UV detectors (Figure 19 & Figure 20). This clearly tells us that the zirconium, when used without oxalic acid as a stabilizing agent against hydrolysis, is not only unreactive, but will adhere efficiently to proteins. This adhesion cannot be removed by adding DTPA (as done in the above protocol), seeing that the hydrolyzed Zr is not reactive and thus cannot be chelated by DTPA. On radio-TLC, the hydrolyzed Zr behaves unlike un-hydrolyzed Zr and does not elute with the citrate. This behavior is therefore easily misinterpreted as being properly labeled on the protein. Furthermore, the hydrolyzed Zr will follow the protein in the large molecule fraction on a PD-10 size exclusion column, and thus end up in the final product.

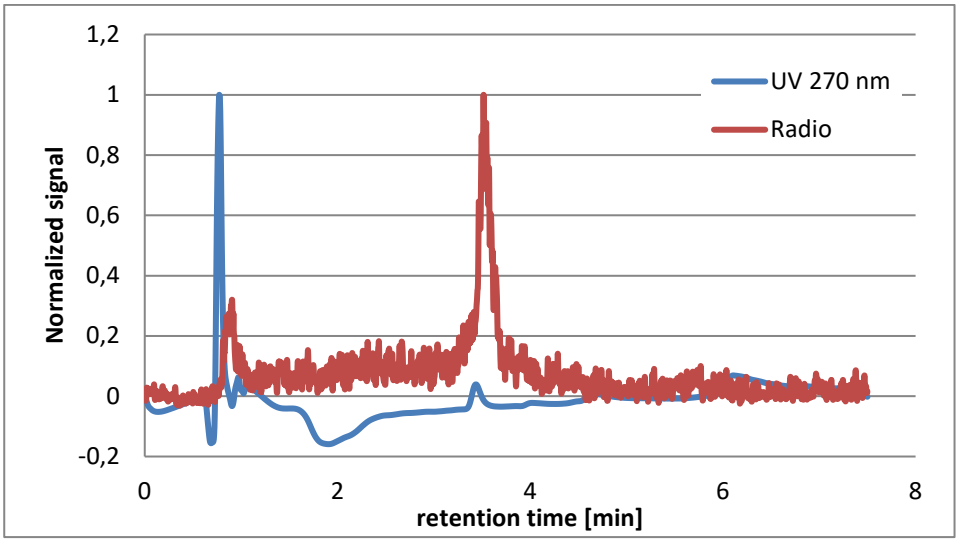

Figure 19: HPLC analysis of ASIS labeled using oxalate as a stabilizer. The chromatogram shows coinciding UV and radio-peaks at 3.5 min.

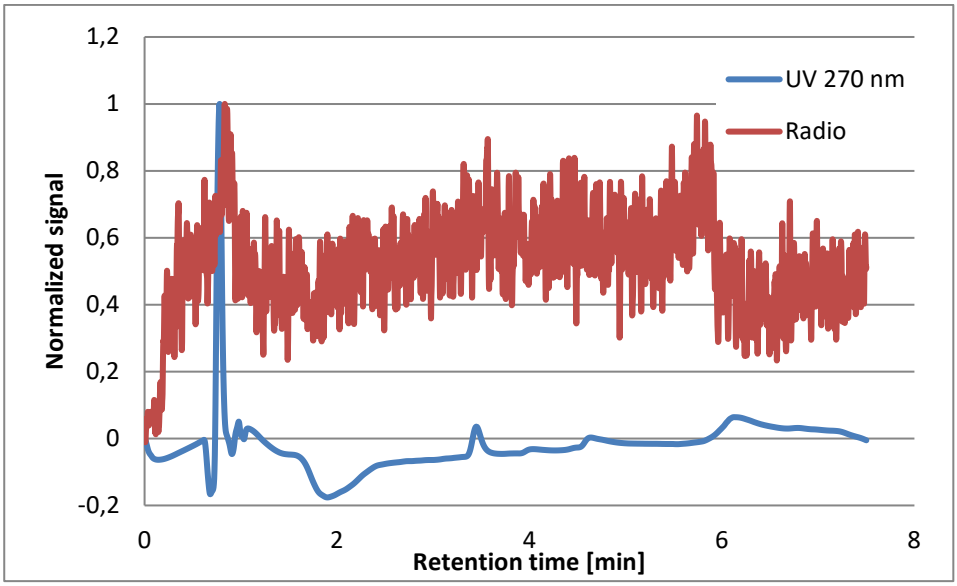

Figure 20: HPLC analysis of ASIS labeled using sucrose as a stabilizer. Here the chromatogram shows no radio-peak at 3.5 min. Instead, the ^{89}Zr appears to elute steadily over the course of analysis.

In the case of both the saline and the sucrose batch, an *in vitro* cell-binding assay showed perfect binding of the labeled protein, but that the binding could not be blocked by addition of carrier protein. This indicates that the ^{89}Zr is binding to the cells without receptor specific binding of the protein [80]. In case of the oxalate batch an activity of 43% was measured.

Based on these results the saline and the sucrose labeling strategies were abandoned.

3.2.3 Inverse labeling

In another attempt to create a labeling method that would avoid exposure of the protein to oxalic acid, we tested labeling the chelator prior to conjugation to the protein. First the ^{89}Zr was incorporated into the chelator under normal labeling conditions for ^{89}Zr i.e. 250 mM Na-oxalate and 185 mM HEPES, pH 7[19].

After 30 min at 40 °C an excess of DTPA was added to make sure all ^{89}Zr was chelated. The oxalate was removed by addition of $CaCl_2$ causing precipitation of insoluble calcium oxalate. The solution was then centrifuged, and the supernatant containing the labeled chelator transferred to the protein. The precipitate contained 34% of the radioactivity. pH of the conjugation reaction was adjusted to 8.5 by addition of sodium carbonate and the solution heated to 40 °C and allowed to react for 1 h.

PD-10 showed a conjugation yield of 28% resulting in an overall labeling yield of 17%. This is low compared to achievable yields upwards of 100% using the standard oxalate method, but nonetheless the result was expected seeing that the conjugation yield normally is around 30%[19].

This method can be used as a last resort to label sensitive metalloproteins, which would otherwise be damaged by the presence of oxalic acid.

Discussion

Even though the labeling yield is quite low, the development of the inverse labeling method could prove very useful for labeling of sensitive proteins. However, the most important result of this section is the documented behavior of hydrolyzed Zr. It is common when labeling antibodies, to use PD-10 columns as the sole indicator for labeling yield[81–84]. The PD-10 result is sometimes combined with size-exclusion chromatography or radio-TLC for verification of the labeled compound. As shown above, these procedures cannot discriminate properly labeled protein from hydrolyzed ^{89}Zr sticking to the protein. Injecting the latter into a patient or animal would most likely result in the hydrolyzed ^{89}Zr distributing independently of the vector.

3.3 Titanium-45

As discussed above, imaging intact antibodies requires relatively long half-lives to provide sufficient signal at the time of optimal distribution. For purely diagnostic purposes however, smaller formats are often engineered (diabodies, Fab-fragments), providing significantly accelerated distribution. For these formats, much shorter radionuclide half-life is required[85]. In recent years there has been growing interest in titanium based anti-cancer drugs with several stable Ti-based compounds published[86,87]. Moving from toxicity tests in cell culture towards clinical use requires understanding of pharmacokinetics of the potential pharmaceutical. Dynamic PET imaging with ^{45}Ti allows noninvasive quantification of the biodistribution, as the radiolabeled pharmaceutical distributes *in vivo*. This could be a valuable asset in the continued development of Ti-based cancer therapy. Furthermore, ^{45}Ti is a highly underutilized radiometal. It has near-perfect properties for peptide and small molecule labeling, such as high production rate, high β^+ branch (~85%), virtually no gamma emission, and a suitable 3-hour half-life. Unfortunately, there is currently no available chelator allowing stable complexation of ^{45}Ti. However, succeeding in forming stable complexes when mimicking the Ti-based anti-cancer drugs, may reveal possible chelation strategies, thus promoting development and use of ^{45}Ti radiotracers.

Properties

^{45}Ti has highly desirable properties for medical imaging. It is an almost clean positron emitter with a combined branch for other gamma emissions of less than 0.4%, low β^+ energy (438.9 keV average) and a high β^+ branch of 84.8 %. With a half-life of 3.08 hours it is from a physical perspective the perfect radiometal for tracing fast clearing or quickly distributing vectors like peptides[88,89].

Production

When irradiating the naturally monoisotopic ^{45}Sc, ^{45}Ti is produced via the ^{45}Sc(p,n)^{45}Ti reaction. At proton energies above approx. 13 MeV small amounts of ^{44}Ti are produced via the ^{45}Sc(p,2n)^{44}Ti reaction. Due to the very long half-life of ^{44}Ti (59.1 years) however, the co-produced activity is very low. The reaction cross sections are seen in Figure 21.

For the current work, we constructed a target consisting of a 6x6 mm Sc foil sandwiched between a silver coin and a 500 μm Al degrader foil (bringing the energy from the nominal 16 MeV to approx. 13 MeV to ensure no co-production of the long-lived ^{44}Ti). The sandwich was placed in the target holder providing direct water-cooling on the rear face of the silver. The target was irradiated at beam currents in the range of 10-20 μA without signs of thermal damage.

Chemistry

The aqueous chemistry of Ti is nontrivial and the reason for the non-existing utilization of an otherwise perfect PET isotope. Due to the high charge to radius ratio, no simple aquated Ti^{4+} ion exists because of its strong propensity for hydrolization. In fuming HCl however, Ti exists in the form of $[TiCl_6]^{2-}$[60]. This is utilized in the separation of Sc and Ti in which the target material after dissolution in HCl is dried under argon and redissolved in 12 M HCl. Now on the chloride form, the Ti being highly oxophilic can react and bind on the diol resin while the Sc passes through. Had the Ti not been in 12 M HCl it would already be at least partially hydrolyzed and thus have reduced or zero affinity for the diol resin.

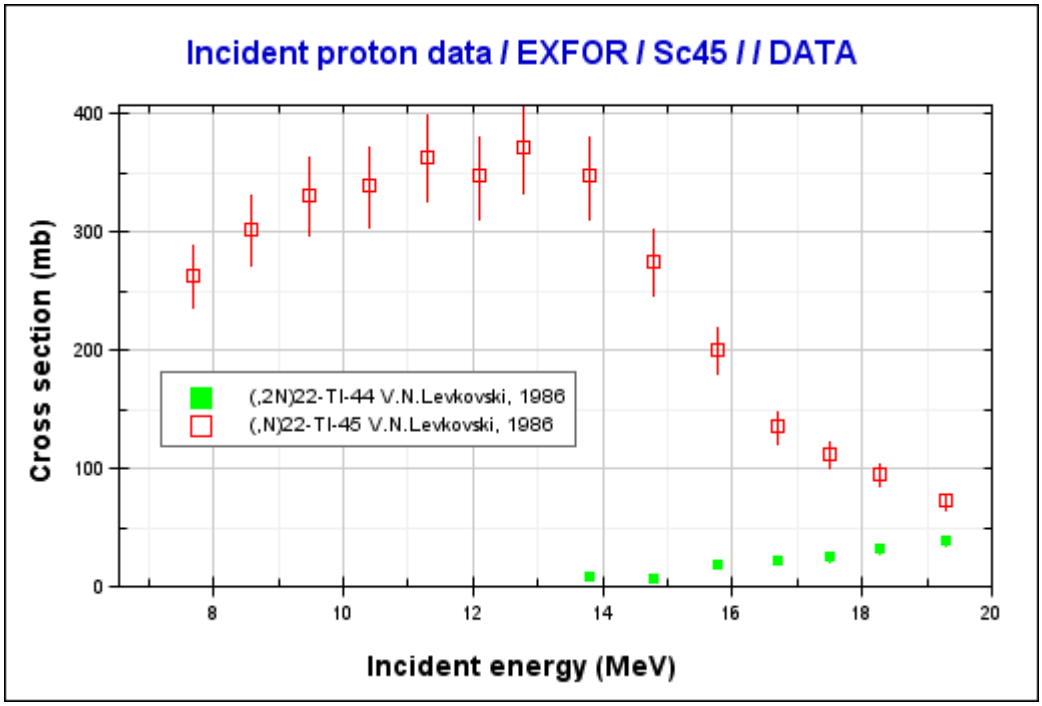

Figure 21: The cross section for the ^{45}Sc(p,n)^{45}Ti reactions peaks around 13 MeV at approx. 370 mb. Co-production of ^{44}Ti starts around 13 MeV. Cross section data adapted from Levkovskij et al [58]

Several different resins were investigated for their ability to trap ^{45}Ti out of 12 M HCl. C_4OH, Tentagel HLOH, 1-hexadecanol and 1-10 decandiol all showed no trapping of ^{45}Ti. Hydroxamate resin[90], Hypogel 200 diol and Hypogel 400 diol resins all were able to trap ^{45}Ti efficiently, but seeing that we were unable to elute the activity from the hydroxamate resin only the Hypogel 200 diol and Hypogel 400 diol were further investigated. The difference between the two is the length of the PEG chain. To decide between the two resins, the partition coefficients of Sc and Ti to the resins were determined. This was done by mixing known quantities of Ti and Sc in 12 M HCl with a known mass of the resins. After equilibration, the partition coefficients could be determined by measuring the Ti and Sc concentrations in the supernatants using ICP-OES. The result showed the Hypogel 200 diol as the better choice having both a slightly higher affinity for Ti as well as higher ratio of the two partition coefficients P_{Ti}/P_{Sc}.

3.3.1 Paper IV

In the paper "Bringing Radiotracing to Titanium-Based Antineoplastics: Solid Phase Radiosynthesis, PET and ex Vivo Evaluation of Antitumor Agent [^{45}Ti](salan)Ti(dipic)" ^{45}Ti is utilized to assess the biological fate of the antineoplastic compound Ti-salan-dipic. A PET analogue of the compound is prepared by complexing the purified ^{45}Ti with salan and dipic on a solid support. The *in vivo* behavior of the compound is monitored in mice using dynamic PET, and shows rapid removal from the bloodstream and translocation into the bile.

Discussion

In spite of the physical characteristics of ^{45}Ti, this study is one of the first to utilize the potential of ^{45}Ti PET imaging. As mentioned, the aqueous chemistry is challenging and currently no suitable chelator exists. If this is solved, and a chelator allowing aqueous labeling is developed, ^{45}Ti could be a

workhorse in nuclear medicine. It has a half-life and production yield that allows for nationwide shipping and has far better imaging characteristics and lower associated patient dosimetry (Figure 10) than ^{68}Ga, which currently is the preferred PET radiometal for peptide labeling. Unlike ^{68}Ga, ^{45}Ti has the further benefit of a half-life that allows imaging of small antibody-derived formats like diabodies. This work hopefully inspires further research in ^{45}Ti radiopharmaceuticals and helps move the development of a ^{45}Ti chelator closer to fulfillment.

4. Introduction to Therapeutic isotopes

4.1 Targeted radionuclide therapy

When looking at PET images showing tumor uptake, it is a very appealing thought to simply attach a therapeutic isotope instead of a diagnostic one. The idea of treating illnesses using radiation is by no means a new one, and iodine treatments of hyperthyroidism have been used for more than 60 years[91]. However, as targeting improves it opens for new opportunities, and allows the specific transport of the therapeutic isotope to the target tissue. This idea was conceptualized by Paul Ehrlich and coined "the magic bullet" already in the 19th century, with his description being remarkably similar to modern day targeted radionuclide therapy [92] (Figure 22). Ehrlich describes how toxins, by the means of highly specific antibodies, could be delivered to only the targeted cells and thus exclusively damage these, while sparing the normal organism. Although the specific vector delivering the therapeutic isotope is not always an antibody and radioisotopes are not toxins, the concept is almost exactly what Ehrlich proposed: A toxic compound delivered specifically to the intended target cells. Instead of poisoning the target cells, the aim in targeted radionuclide therapy is to induce irreparable damage to the DNA, commonly believed to be done most efficiently via induction of double strand breaks[93].

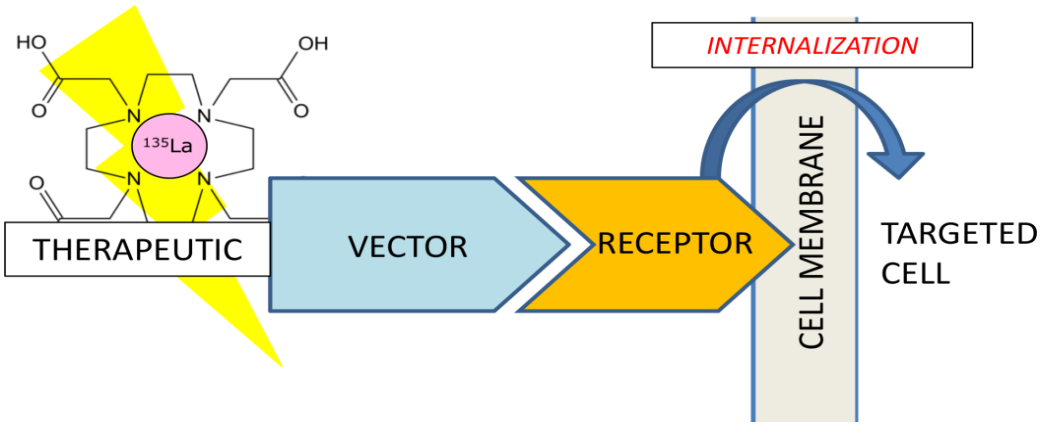

Figure 22: Illustration showing the concept of targeted radionuclide therapy. The therapeutic isotope is bound to a vector with high specificity for a certain receptor which is exclusive to or overexpressed on the target.

Intact antibodies are still used as vectors, but are receiving increasing competition from smaller formats like antibody fragments and other antibody derived formats, peptides and aptamers which due to their smaller size exhibit faster *in vivo* distribution[94].

Once the vector has reached its target tissue, the radiotherapeutic will locate either on the surface of the cells or be internalized into the lumen of the cell. The two scenarios each pose a different set of challenges. If the ligand ramains on the surface of the cell the ligand-receptor bond needs to remain intact, preferably throughout the entire life-time of the radioisotope. Furthermore, the radioisotope needs to be bound to the ligand in a way, such that it does not, for whatever reasons, dissociate with subsequent removal from the target cells. If on the other hand the ligand is internalized, the ligand is transported through the endocytic pathway and degraded in lysosomes[95]. During this process the radio-isotope can be released from the ligand vehicle and travel based on the chemical characteristics of the isotope. The elements generally have widely different fates in the body, however, once

internalized, metals generally stay inside the cell at timescales relevant for therapy and imaging[38]. Halogens on the other hand are efficiently transported out of the cell and into circulation, thus loosing their effect as imaging- or therapeutic agents.[96]

4.2 Radionuclides used in therapy

Traditionally, high-energy β-emitters have been used in targeted radionuclide therapy[97]. Over the last few years however, there has been an increasing interest in α-emitters, which to a large extent is due to the advent of the first commercially available α-emitter based therapeutic, Xofigo (formerly Alpharadin). Consisting of something as simple as the calcium analogue [^{223}Ra]-$RaCl_2$, it preferentially accumulates in bone metastases of patients, suffering from illnesses such as disseminated prostate cancer[98–100]. To understand the benefits of α-emitters one must first be introduced to the term Linear Energy Transfer (LET). When particles move through matter, they deposit their energy by ionizing atoms in the matter. In water which comprises most of the human body, this leads to formation of free radicals.

$$H_2O \rightarrow H_2O^+ + e^-$$

$$H_2O^+ + H_2O \rightarrow H_3O^+ + OH\cdot$$

The free radicals produced in the ionizations, are highly reactive oxygen species capable of destroying biological molecules, including DNA[101]. The amount of energy deposited per unit length is termed LET. Seeing that the amount of energy needed to create an ionization event is the same for different kinds of ionizing radiation, the LET is proportional to the number of ionization events per unit length. The average length traveled by the particle between such ionization events is very different for α- and β-particles [9]. The mean distance traveled by an electron between subsequent ionizations, is much larger than the distance between the two DNA strands. This makes it highly unlikely that a single pass of an ionizing electron will cause a double strand break. The very high LET associated with α-particles results in high density of ionizations along the track making the creation of a double strand break much more probable (Figure 23).

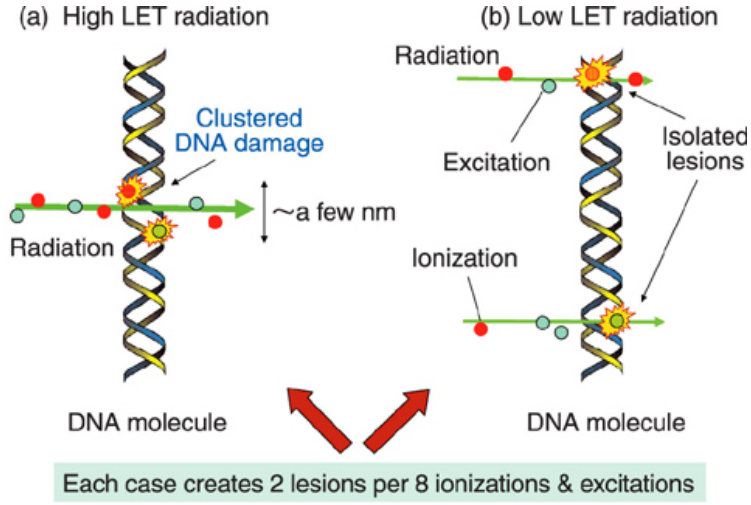

Figure 23: When the same amount of energy is deposited in a cell the number of single-strand breaks is also similar, however the highly clustered energy deposition of high-LET radiation, dramatically increases the chance of creating double-strand breaks. Adapted from the JAEA R&D Review 2007[102]

A way to quantify the increased effectiveness in damaging cells is by measuring the relative biological effect (RBE) of the radiation. This is done by measuring the dose needed to achieve a certain biological endpoint (like LD10 orLD50) and comparing it to the dose needed from a low LET source (typically a ^{60}Co or 250 keV x-ray source) to get to that same endpoint. This way an RBE of 2 means that only half the dose compared to the low LET standard, is needed to reach the same biological endpoint. The common tabulated RBE-value for α-emitters is 20, meaning that they, dose for dose, are 20 times more efficient in killing cells[103].

The use of α-emitters is still limited for several reasons. One reason for the limited use is availability. ^{225}Ac and ^{213}Bi are still only available in limited amounts from the decay of ^{229}Th even though cyclotron production is feasible [104,105]. However, the main reason is the difficult to handle decay chains. Most α-emitters with a half-life suitable for targeted radionuclide therapy have several α-emitting daughter isotopes with half-lives that allow complete biological redistribution of the daughter (Figure 24). If the daughters would stay with the vector, this would not pose any complications but only contribute to the dose to the targeted tissue. Unfortunately this is not the case as the recoil energy of most daughter nuclides exceeds 100 keV [10]. For comparison the binding energies of the daughters of ^{225}Ac to the cyclic chelator DOTA are less than 20 eV [106].

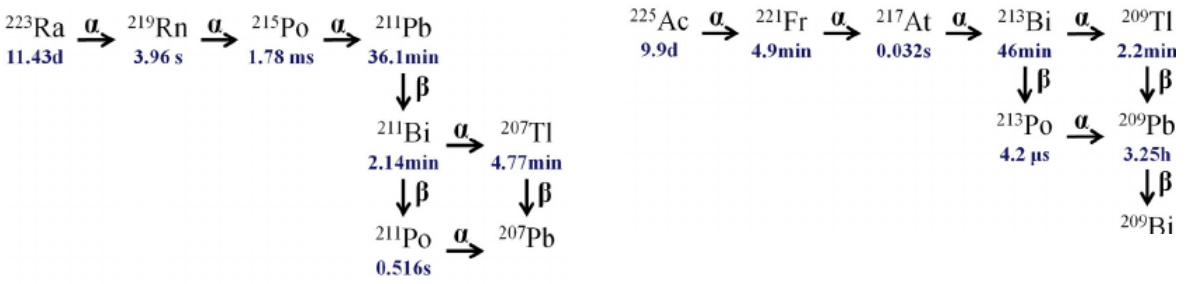

Figure 24: The decay chain of ^{223}Ra and ^{225}Ac. ^{211}Pb, ^{221}Fr and ^{213}Bi have half-lives allowing redistribution *in vivo* before subsequent α-emissions. Adapted from Rojas et al. [107].

One α-emitter, ^{211}At, can be produced on cyclotrons and decays by a single α-particle emission. However, the half-life of 7.2 hours makes logistics and availability a challenge. With astatine being a halogen, the vector used must be non-internalizing to avoid dislocation of the radionuclide. ^{211}At is probably still the most promising α-emitter for targeted radionuclide therapy.

With the lacking availability and challenging decay characteristics of α-emitters, targeted radionuclide therapy is today mainly performed by the use of β-emitters. Here commonly used radionuclides include ^{90}Y, ^{177}Lu and ^{131}I, with mean β-energies of 933.5 keV, 141.0 keV and 181.2 keV respectively[108]. As mentioned earlier the corresponding range is estimated by the approximation

$$Range\ [cm] \sim \frac{\bar{E}_{\beta^+}\ [MeV]}{2}.$$

For many years, a third group of radionuclides, the Auger-emitters, has received interest due to the properties of the inherent Auger cascade. Here, following electron capture or a conversion electron, the atom is left with a resulting K or L-shell vacancy. As the vacancy is filled by an electron from a higher energy shell or subshell the excess energy (the energy difference between the higher energy shell and the acceptor shell) is transferred to an even higher energy electron which is ejected from the

atom. This creates yet another vacancy and now two vacancies are present. The relaxation repeats itself to fill the two vacancies rendering four vacancies. This process, called the Auger cascade, continues until the vacancies have propagated to the outermost, lowest energy electrons with measured Auger electron yields of > 30 e^-/decay[109]. A competing process during relaxation is the emission of characteristic x-rays (Figure 25).

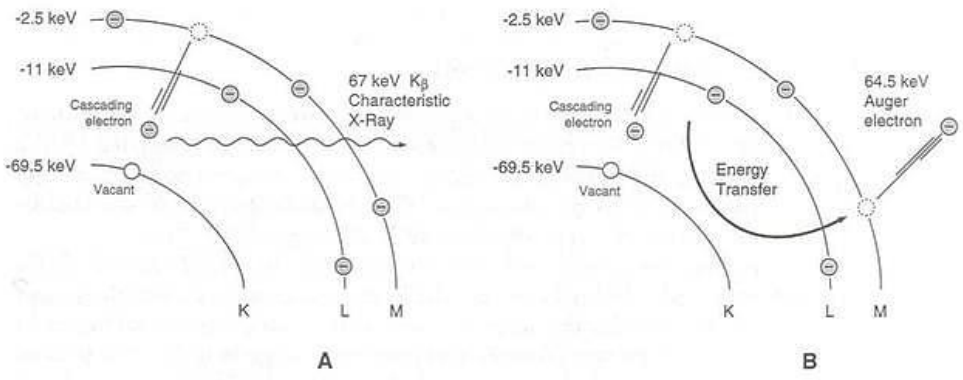

Figure 25: Illustration of the relaxation subsequent to electron capture. A K-shell vacancy is filled with a higher energy electron and the excess energy is emitted as A) a characteristic x-ray or B) an Auger electron. Adapted from Bushberg et al.[32]

The Auger electrons have very low energy compared to β-emissions and therefore very short ranges resulting in highly localized energy deposition. Combined with the high multiplicity of emitted electrons it results in ionization density similar to high-LET radiation (Figure 26). From a physical perspective it is therefore expected that the RBE value for the Auger emitters is larger than 1 [110–112]. The expected crossfire on neighboring cells is likewise expected to be minimal due to the short range of the emissions and the $1/r^2$ decrease in ionization density.

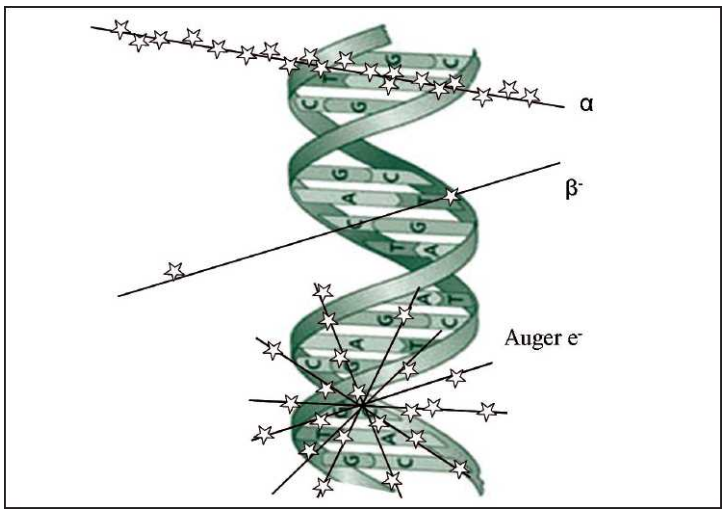

Figure 26: Ionizations (represented as stars) in close proximity of the DNA to illustrate the ionization density from α and β particles as well as from Auger electrons. The multiplicity of the Auger electrons create a high-LET-like ionization density. Adapted from H. Thisgaard [113].

4.3 Choice of therapeutic radionuclide based on target size

For all targeted radionuclide therapy, the radioisotope is chosen based on several criteria:

- Stable labeling chemistry:
- When a vector is used, the element must allow stable chemical attachment to that vector. If the construct is unstable and the therapeutic isotope dissociates from the vector, it will in the best case result in inefficient treatment and in the worst case result in high doses to non-target tissues.
- Low γ-yield:
- The radioisotope should have a low abundance of γ-emissions to reduce dose to non-target tissues. Low yield 100-300 KeV can however be beneficial, allowing SPECT imaging and thus aid dosimetry calculations.
- Tumor size and receptor abundance:
- Generally, it is preferable to have the range of the β be equal to or smaller than the size of the tumor targeted. If the β range is larger than the tumor size, it will lead to increased dose to normal tissue (Figure 27).

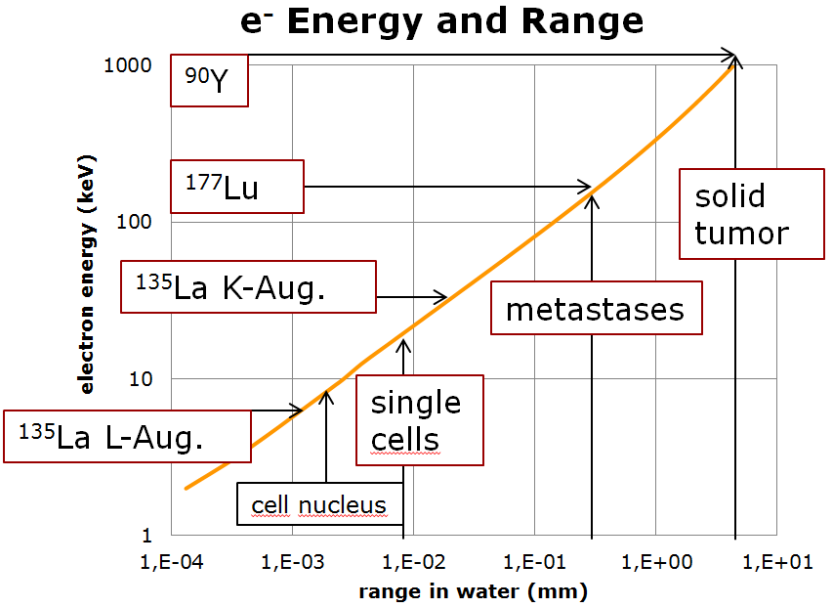

Figure 27: Illustration of electron energy as function of range. Insert is typical sizes of biological targets and ranges of the commonly used therapeutic isotopes ^{90}Y and ^{177}Lu as well as the Auger emitter ^{135}La.

The importance of matching the isotope with the size of the target is a consequence of the tumor to target ratio. Too high energy compared to the target size will result in the beta particle depositing most of its energy outside the target volume. This is of course undesirable, as the energy will be deposited in normal healthy tissue[114]. Therefore, a reasonable method for choosing the isotope is by evaluating the fraction of its energy that is deposited in the target volume. By plotting the relative fraction of the total energy released per decay that is deposited inside the target volume as a function of target radius, it can be visualized which radioisotope will deliver the least dose to normal for a given dose to target.

This was done for ^{90}Y, ^{177}Lu, and ^{165}Er using the sphere model in OLINDA down to target sizes of 10 mg. Below this size the MIRDcell formalism was used to calculate the dose to spherical cell volumes

down to 3.3×10^{-11} g [115]. The target masses were converted to radius using the density of water = 1 g/cm^3, and the doses were recalculated to reflect identical activity concentration of 1 MBq/g. The results can be seen in Figure 28.

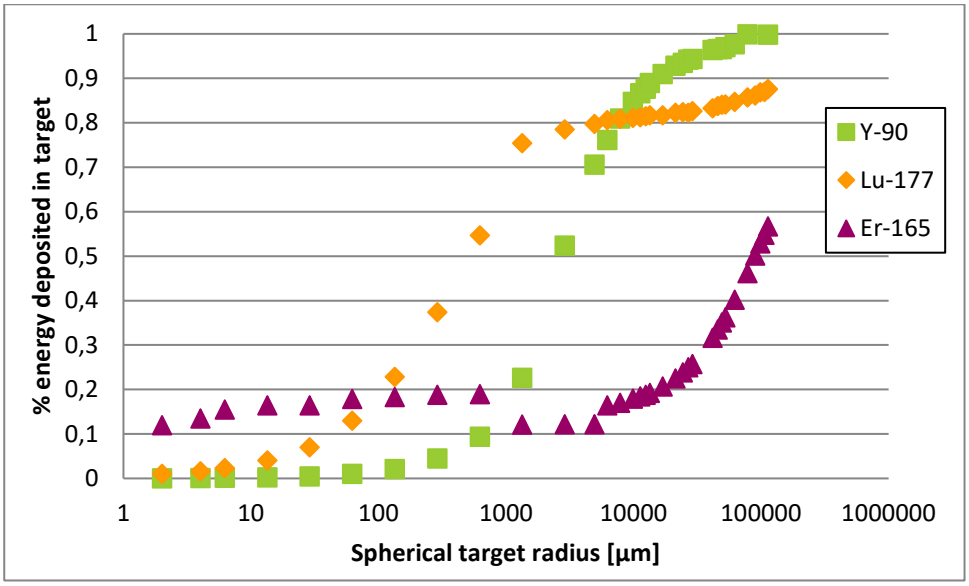

Figure 28: The fraction of energy emitted that is deposited in the target sphere as a function of target sphere radius.

Despite the apparent mismatch in deposited energy for ^{165}Er where the two models OLINDA and MIRDcell meet, the figure illustrates the point that smaller targets, require lower β energy in order to spare the surrounding tissue. The high-energy beta emitter ^{90}Y is superior for large targets with diameters of >15 mm. Below 15 mm and down to a diameter of roughly 250 µm ^{177}Lu fares the best. Below 250 µm the Auger emitter ^{165}Er has the highest fraction of its energy deposited in the target, and especially for very small targets the benefit over the other two is remarkable.

Another thing to notice is the shape of the ^{165}Er curve. At large radii the fraction of its energy deposited starts growing as a consequence of the x-rays getting more efficiently stopped in the larger spheres. At the low radii (< 500 µm) there is hardly any decrease until radii < 6 µm. This means that even for a sphere with radius of 6 µm almost the entire electron dose is deposited inside. This simultaneously implies that hardly any dose will be imparted on healthy cells, even when in close proximity of the target cell.

It should be mentioned however, that other considerations than minimizing dose to normal tissue need to be taken when planning treatment. Importantly, tumors are never homogeneous, meaning that uniform distribution of the isotope inside the tumor volume, cannot be assumed. In this regard, the higher energy β-emitters have advantage seeing that an area in the tumor volume with low uptake, will still receive substantial dose from high uptake areas. This argues for use of emission energies higher than what is indicated in the above figure (Figure 28).

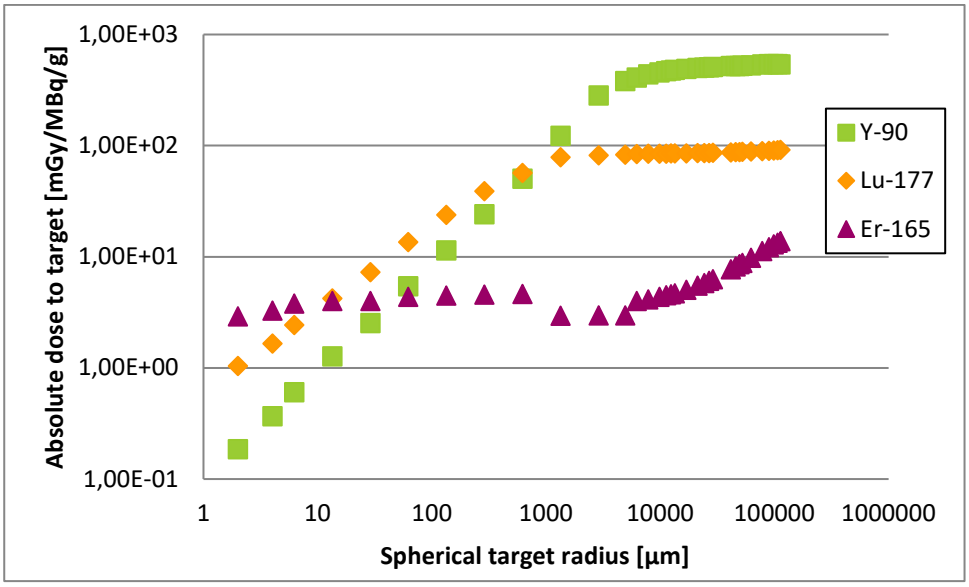

Figure 29: The absolute dose to target spheres as function of sphere radius for identical activity concentration of 1 MBq/g

Looking at the absolute dose delivered as a function of sphere size, it is evident that the β-emitters ^{90}Y and ^{177}Lu deliver much higher doses at large sphere sizes than the Auger emitter ^{165}Er. This is of course expected as the total amount of energy released per decay for the two is likewise significantly higher (0.934, 0.18054 and 0.04224 MeV/(Bq·s) for ^{90}Y, ^{177}Lu and ^{165}Er respectively). However, at the size of single cells (r = 5 µm) the Auger emitter delivers higher absolute dose than both ^{90}Y and ^{177}Lu (Figure 29).

Due to the modular design of radiometal-based pharmaceuticals, it is easy to substitute one radiometal for another, if other properties are needed. This especially holds true, if the same chelator can be used to stably complex both radiometals. Therefore choosing a radioisotope that can readily be substituted for other isotopes with different properties is advantageous. Here the group of lanthanides is especially interesting. Its 15 members have virtually identical chemistry allowing complexation with the chelator cDTPA[116]. The group of lanthanides hosts α, β and Auger emitters for therapy and PET and SPECT isotopes for diagnostics. These features make the lanthanides a very attractive group of metals and ideally suited for use in therapy, seeing they allow both facile tailoring to different tumor sizes as well as exchange for diagnostic isotopes for evaluation of treatment response and dosimetry.

5. Projects based on therapeutic isotopes

The aim of the work within the field of therapeutic isotopes, was to develop robust methods for production and utilization of the lanthanide radionuclides ^{135}La, ^{165}Er, and ^{177}Lu.

5.1 Lanthanum-135

^{135}La properties

^{135}La decays by electron capture, primarily to the ground state of stable ^{135}Ba, with a half-life of 19.5 hours[117] (Figure 30). Following the decay, Auger electrons are emitted which are potentially useful for internal radiotherapy. X-rays accompany the Auger cascade with a spectrum comparable to that of ^{125}I allowing concurrent SPECT imaging in small animals, facilitating dosimetry calculations in small animal models.

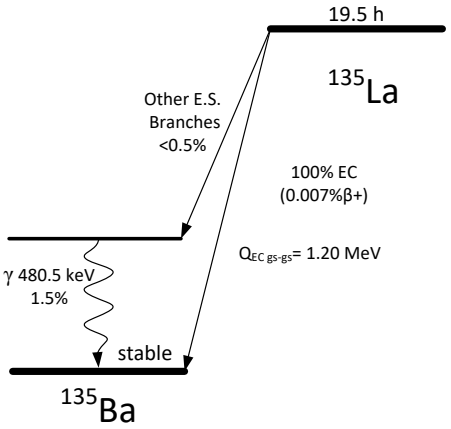

Figure 30 A simplified decay scheme of ^{135}La [117].

^{135}La production

^{135}La is produced via proton bombardment of ^{nat}Ba. It is produced through several channels with ^{135}Ba(p,n)^{135}La and ^{136}Ba(p,2n) as the main contributors at 16 MeV. It is the primary radioisotope produced in proton induced reactions on unenriched barium (Figure 31). The isotopes ^{132}La and ^{133}La are coproduced via (p,n) and (p,2n) reactions on ^{132}Ba and ^{134}Ba respectively. Due to their shorter half-lives of 4.8 and 3.9 hours respectively, the relative amounts can be reduced either by waiting or by irradiating longer (Figure 32). Longer irradiation will shift the ratio because the shorter half-life isotopes will approach saturation (Figure 5).

The targets were produced by pressing chunks of dendritically distilled metallic barium into a groove in a silver disc. Barium is soft and malleable and can be pressed to a smooth surface using a mechanical press at a pressure of approx. 20 kN/cm^2. Barium readily oxidizes in air and, seeing that the thermal conductivity of the oxide is only 1/6th of that of the metal, it is important to minimize this process[118]. To do so, the pressed targets were immediately mounted under a cover foil in the target holder. Thermal conductivity of the metal is fairly low (18.4 W/(m·K) but beam currents of 15 μA were routinely used without visible signs of the target melting.

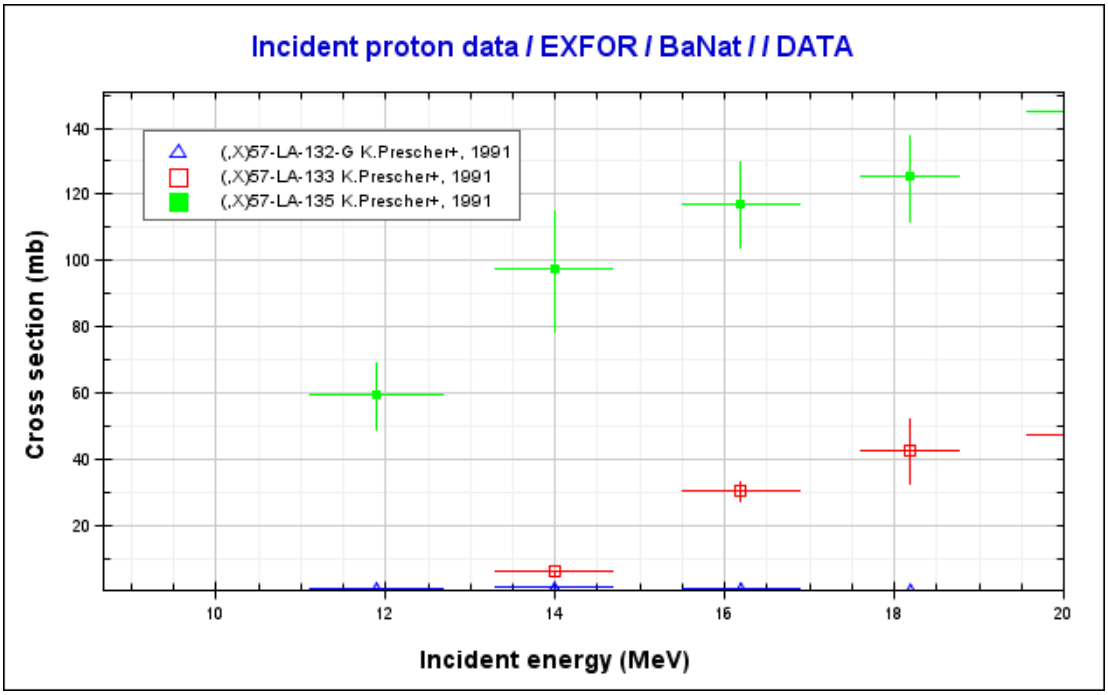

Figure 31: The reaction cross sections for $^{nat}Ba(p,x)^{132g}La$, $^{nat}Ba(p,x)^{133}La$ and $^{nat}Ba(p,x)^{135}La$ at incident energies <20 MeV.

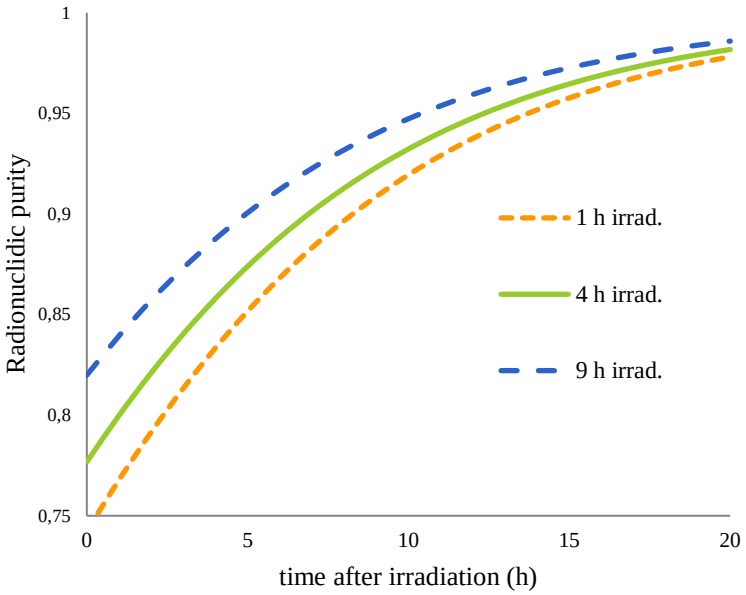

Figure 32: Graph showing the radionuclidic purity as a function of time after EOB and the effect of irradiation times. At longer irradiations the shorter half-life isotopes will approach saturation levels while the ^{135}La production rate will be almost unchanged. This causes the radionuclidic purity to increase as a function of irradiation time.

Lanthanide chemistry

The chemistry of lanthanum follows the general rules for lanthanides. Lanthanum, like the rest, has a strong preference for the $(M)^{3+}$ oxidation state and being the first in the line of lanthanides, it has the biggest ionic radius of 1.061 Å vs only 0.848 Å for the last in the lanthanide series, lutetium. The decreasing ionic radius of the $(M)^{3+}$ ions, known as the lanthanide contraction is a consequence of imperfect shielding of charge between *4f* electrons, resulting in the increasing effective nuclear charge experienced by the *4f* electrons as the number of protons increases. Since the *4f* electrons are relatively uninvolved in bonding, this change in ionic radius and the influence this has on complex formation with ligands is exploited to separate the different lanthanide ions. A commonly used ligand for this kind of separation is α-hydroxyisobutyric acid (α-HIBA). However, separation of neighboring lanthanides using this method is not trivial, and suffers from low separation efficiency, large solvent volumes and from being very time consuming.

Lanthanum has the benefit of having the lanthanide chemical properties providing possibilities for facile interchange to other therapeutic- or diagnostic lanthanide isotopes, while as the only lanthanide having non-lanthanide target for (p,x) reaction-based production. This allows efficient separation from the barium target material, while retaining the benefits of the lanthanide group.

The separation is performed by dissolving the barium target material in HCl. Once dissolved the solution is buffered to pH 3-7 using ammonium acetate or HEPES buffer. Under these conditions, the cationic ^{135}La is retained when the solution is passed over Waters Accell Plus CM weak cation exchange resin. The target barium also traps so some degree but gives way to the ^{135}La, which is quantitatively trapped. After washing the column with water and/or buffer, the ^{135}La can be eluted in 0.1 M HCl.

5.1.1 Paper V

The paper "*^{135}La as an auger electron emitter for targeted internal radiotherapy*" describes in detail the production methods including target preparation, irradiation, separation and molar activity measurements. It further presents a recalculated Auger spectrum, and the associated cellular dosimetry.

Discussion

The published production rates may prove insufficient for large-scale production using a 16 MeV cyclotron. However, looking at the cross sections above 30 MeV reveals potential for much higher production rates (Figure 33). Calculations based on stopping powers calculated using SRIM[16] and the experimental cross sections measured by Prescher[119] and Tárkányi[120] were performed, using an incident energy of 50 MeV and a target thickness allowing the beam to exit the target barium at an energy of 30 MeV. The calculations show an approx. 50-fold increase in production rate, as compared to the calculated production rate of a 16 MeV incident beam on a thick target. This would amount to approx. 750 MBq/μAh, allowing production of tens of GBq. If a high-energy cyclotron is not available, the production rate can be greatly increased by bombarding enriched ^{135}Ba, which only comprises 6.6% of ^{nat}Ba. This, along with target optimization for higher beam currents, should allow an increase in production rate, similar to what is gained from higher energy. Due to the high cost of enriched isotopes reuse of 135Be would most likely be necessary. Although sacrificing some of the production rate, a solution target containing aq. $^{135}BaCl_2$ could prove to be a viable route.

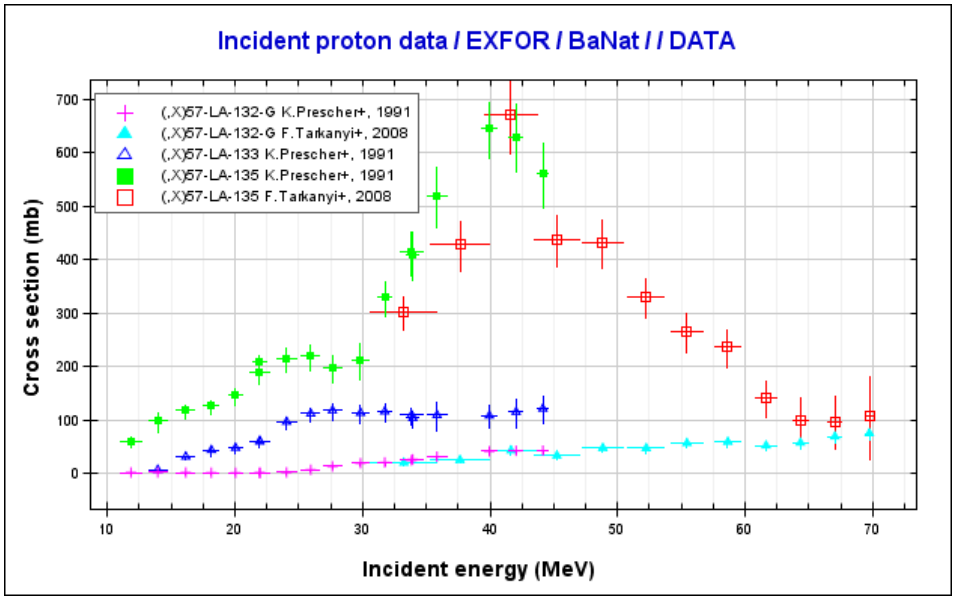

Figure 33: Expanding the scope beyond energies commonly available on small medical cyclotrons reveals high cross section values of >650 mb for the $^{nat}Ba(p,x)^{135}La$ reaction around 40 MeV.[119,120]

5.2 Erbium-165

Another promising Auger emitter besides ^{135}La is ^{165}Er. With a higher number of Auger emissions and lower gamma and fluorescence yield, this lanthanide is perfectly suited for Auger therapy. However, unlike ^{135}La it suffers from only having lanthanide neighbors, making the separation from the target material both inefficient and time consuming. The attached paper draft "A Szillard-Chalmers Based Generator for the Auger Emitter Erbium-165" presents a liquid generator-based production method based on the escape of ^{165}Er from DOTA subsequent to the auger cascade of its mother isotope ^{165}Tm. The paper provides an elegant and possibly general method for separating daughter isotopes following EC decay.

^{165}Er properties

Prominent amongst pure auger emitters as an internal radiotherapeutic nuclide is ^{165}Er. It has an attractive half-life of, 10.4h, making it suitable for both peptide and antibody labeling.

^{165}Er production and separation

As mentioned, ^{165}Er is produced in a generator system as the daughter of ^{165}Tm. At 16 MeV ^{165}Tm is produced by proton irradiation of ^{nat}Er via the ^{nat}Er(p,2n)^{165}Tm reaction. At higher energies the production rate increases significantly, likely due to contribution from the production channels ^{nat}Er(p,3n)^{165}Tm and possibly ^{nat}Er(p,4n)^{165}Tm (Figure 34). [121–123]

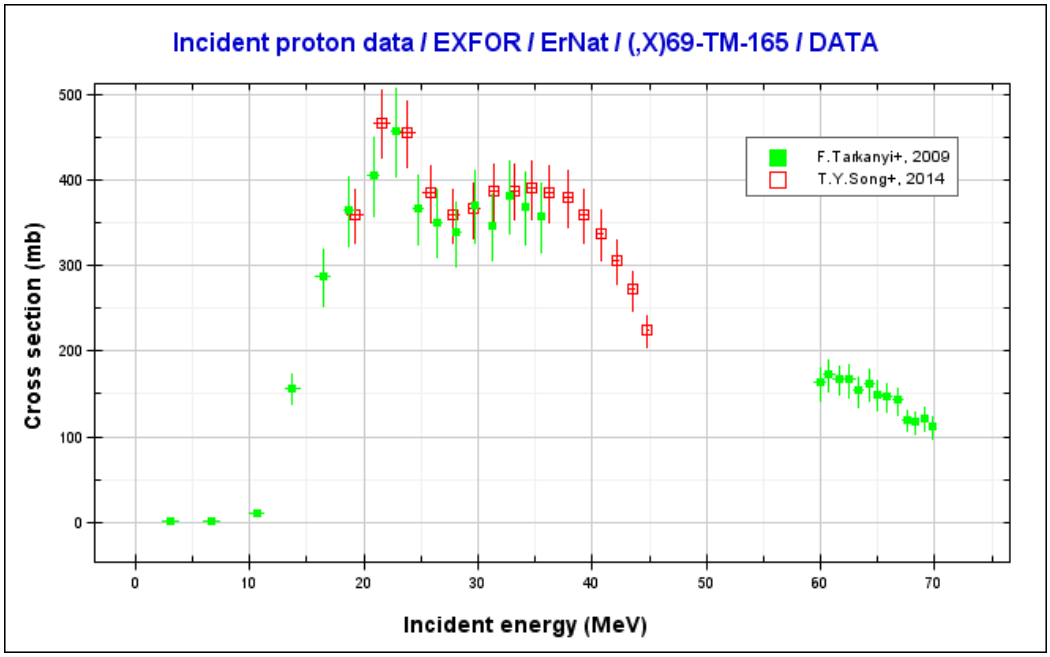

Figure 34 Like in the case of ^{135}La the experimentally measured cross section data shows a large increase in potential production rate when going beyond the 16 MeV[124,125].

Here a 250 µm thick Er foil was mounted under a 100 µm Al cover foil, and irradiated at 20 µA, without taking damage. During bombardment, many other Tm isotopes than ^{165}Tm (^{161}Tm, ^{162}Tm, ^{163}Tm, ^{164}Tm, ^{166}Tm, ^{167}Tm, ^{168}Tm and ^{170}Tm) are coproduced.

After irradiation the Er foil is dissolved and the bulk of the ^{nat}Er is removed using LC with α-HIBA solvent. The remaining Er and Tm is chelated using the cyclic chelator DOTA at 95 °C. When ^{165}Tm decays by EC, the ^{165}Er daughter is released from the chelator. Since erbium cannot reenter DOTA at room temperature, it stays in solution, and can be collected by passing the entire solution over cation exchange resin. The other coproduced Tm isotopes all have short half-lives or stable daughters, rendering ^{165}Er the only radioisotope trapped. Utilizing the decay mediated release from DOTA, the ^{165}Er can be separated from the ^{nat}Er in high purity.

The parent/daughter activity relationship between ^{165}Tm and ^{165}Er is given by the equation:

$$A_{Er} = \frac{\lambda_{Er}}{\lambda_{Er} - \lambda_{Tm}} A_{Tm_0}\left(e^{-\lambda_{Tm}t} - e^{-\lambda_{Er}t}\right) + A_{Er_0}e^{-\lambda_{Er}t}$$

with A_{Tm_0} and A_{Er_0} denoting ^{165}Tm and ^{165}Er starting activities respectively. This is simply the solution to the differential equation $\frac{dN_{Er}}{dt} = \lambda_{Tm}N_{Tm} - \lambda_{Er}N_{Er}$ saying that the change in number of ^{165}Er nuclei is the influx from decaying ^{165}Tm minus the number of decaying ^{165}Er nuclei[126]. The ^{165}Tm/^{165}Er relationship shows that the ^{165}Er activity peaks after 24 hours at 57% of the starting ^{165}Tm activity (Figure 35).

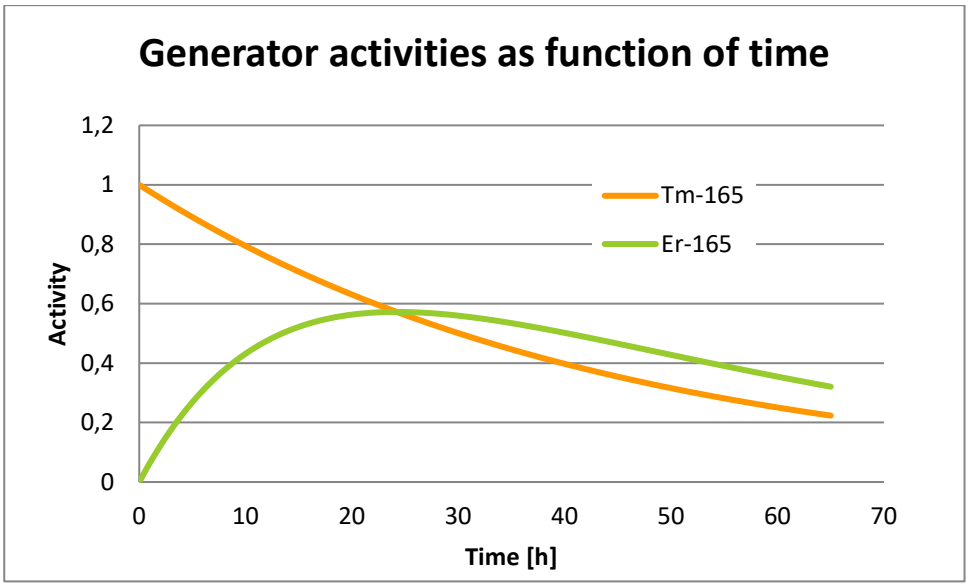

Figure 35: The normalized ^{165}Tm and ^{165}Er activities as a function of time.

This means that given the measured production rate of ^{165}Tm of 233 MBq/μA at saturation, a 4 hour irradiation at 20 μA can theoretically yield 235 MBq of purified ^{165}Er 24 hours later.

5.2.1 Paper VI

The paper draft "*A Szillard-Chalmers Based Generator for the Auger Emitter Erbium-165*" is attached, describing the 165Er generator as well as α-HIBA separation of erbium from thulium in detail.

Discussion

For small animal trials, only small amounts of activity are sufficient to prove the concept of ^{165}Er based radionuclide therapy. As for ^{135}La however, the published production rate on a 16 MeV cyclotron is

insufficient for clinical use. But also in this case, greatly increased production rates are available at higher incident energies. Comparing the thick target yield using 50 MeV protons to the 16 MeV data, reveals a 43-fold increase in production rate which would allow production of >10 GBq of ^{165}Er (Figure 34).

When using ^{nat}Er targets of the size needed for 16 MeV irradiation, the removal of bulk ^{nat}Er using LC is probably not needed. Chelating the entire target mass would require 1-2 g of DOTA which is still economically feasible compared to the cost and time spent setting up and running the LC method. However, if the method is to be applied to large-scale production on a 50 MeV cyclotron, the target mass for a would be approx. 18 times higher[16] making removal of ^{nat}Er necessary.

Another possible route to higher production yields, could be the (p,n) reaction on monoisotopic ^{165}Ho. As mentioned the subsequent α-HIBA separation of two neighboring lanthanides is time-consuming and not highly efficient. Nonetheless, with careful optimization, this route could provide high amounts of ^{165}Er, for applications where very high specific activity is not essential.

5.3 Lutetium-177

^{177}Lu properties

With a one-week half-life (6.65 d), 100 % β^- -emission and a low gamma dose, ^{177}Lu has excellent physical properties for targeted radionuclide therapy. It has a 10 % abundant 208 keV gamma emission suitable for concurrent SPECT imaging and dosimetry evaluation (Figure 36). The average beta-range in soft tissue of only 670 μm makes the isotope ideal for irradiation of small volume tumors and micro-metastasis[127].

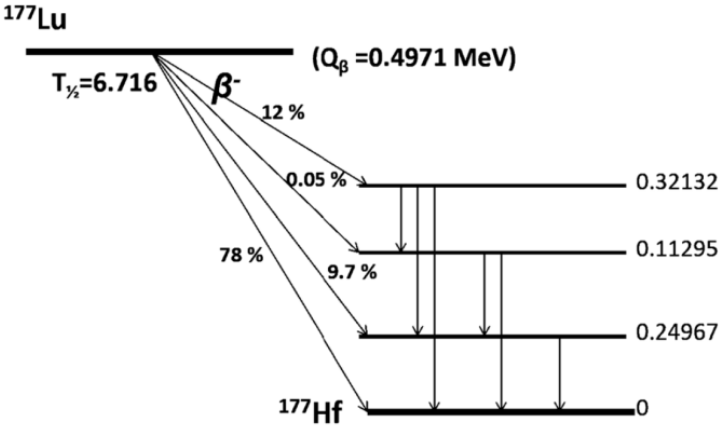

Figure 36: A simplified decay scheme for ^{177}Lu. Adapted from Dash et al.[127]

^{177}Lu production

^{177}Lu is, unlike the other radioisotopes in this thesis, produced in a reactor. This can be done in two different ways: The direct route of ^{176}Lu(n,γ)^{177}Lu or the indirect way ^{176}Yb(n,γ)^{177}Yb with subsequent decay of the short-lived ^{177}Yb ($T_{½}$ = 1.9 h) to ^{177}Lu (Figure 37). Under normal conditions, neutron activation via (n,γ) reactions will yield very low specific activity seeing that the target material cannot be chemically separated from the product. For the ^{176}Lu(n,γ)^{177}Lu reaction this is not the case because of the unusually high associated reaction cross section of 2090 barns for neutron capture. This allows normal research reactors to reach approx. 25 % of theoretical specific activity (1.1 TBq/mg) in a 4 week irradiation[127,128]. In theory, the latter production route can yield higher specific activity, seeing how the target material can be chemically separated, but suffers from much lower neutron capture cross section and thus much lower production rates.

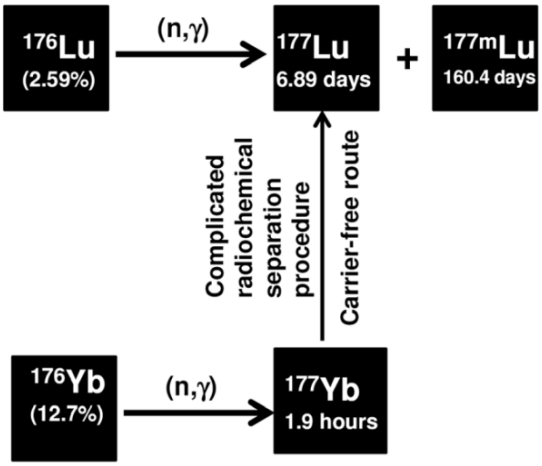

Figure 37: Diagram showing the two main routes to ^{177}Lu. Enriched ^{176}Yb or ^{176}Lu is irradiated with neutrons to either directly or indirectly via ^{177}Yb decay produce ^{177}Lu. Adapted from Dash et al.[127]

5.3.1 Paper VII

The protein "Active Site Inhibited factor 7" (also ASIS or FVIIai) was labeled with ^{177}Lu for a pre-clinical therapeutic study. Factor 7 is a natural ligand to tissue factor, a 47 kDa transmembrane protein, which is the main initiator for the coagulation cascade. However, tissue factor overexpression is also associated with cancer. In pancreatic cancer, accounting for 3 % of all newly diagnosed cancers, but 6 % of cancer deaths due to its high associated mortality, tissue factor overexpression has been linked with metastasis and poor survival. For treatment of pancreatic cancer, tissue factor has been identified as a potential target for targeted cancer therapy. For that same reason, ASIS has previously been labeled for diagnostic purposes using ^{64}Cu, seeing how targeted therapeutics are only feasible with confirmed overexpression of tissue factor[129,130].

This project was aimed at targeting tissue factor for radionuclide therapy to treat tissue factor-expressing pancreatic cancer in mice.

^{177}Lu-cDTPA-ASIS was produced on four separate occasions (cDTPA is shorthand for NCS-p-Bn-CHX-A''-DTPA). Initially the chelator of choice had been DTPA, but the chelate formed with ^{177}Lu was not stable against the 0.1% TFA present in the HPLC eluent nor against the citric acid eluent used in TLC, making quality control difficult. While the lability of the chelate in these solvents may not necessarily result in ^{177}Lu dissociation *in vivo*, we decided to label using cDTPA instead which did indeed result in higher stability at low pH[8,131].

The protein was stored at a concentration of 2.4 mg/mL in calcium-containing isotonic HEPES buffer (50 mM HEPES, 10 mM $CaCl_2$, 150 mM NaCl). To this solution, 50 µL of 300 mM Na-HEPES pH = 10.5, and 70 µg of cDTPA were added per mg of the protein. This corresponds to 5:1 chelator to protein ratio. The cDTPA had been solubilized in DMSO the same day at 15.4 mg/mL allowing the final concentration of DMSO in the reaction solution to be less than 1%. The pH of the mixture was measured using PeHanon pH strips and found to be pH ≈ 8. This mixture was allowed to react for two hours at room temperature and then overnight at 5 ˚C. The following morning, the conjugation efficiency was determined by UV-HPLC (Hitachi Chromaster). Standard curves for both the cDTPA and the ASIS protein allowed quantification of the amount of chelator conjugated to the protein. This was achieved by simply quantifying the remaining unbound chelator at the end of reaction. This showed

that 0.88 chelators were consumed per protein, i.e. 17.5 nmol cDTPA per mg protein. By subtracting the added signal from the conjugated chelators from the protein peak, the specific UV absorbance of the conjugated protein could be calculated for further measurements. The unreacted chelator was removed by gel filtration (PD-10, GE Healthcare) in glycylglycine buffer (10 mM glycylglycine, 10 mM $CaCl_2$, 150 mM NaCl; pH = 7.0). Before adding the sample the PD-10 column had ~5 mg of human serum albumin (HSA) loaded and been washed with >20 mL of the glycylglycine buffer. Gel filtration was performed using a loading volume of less than 1.5 mL to ensure efficient separation with minimum loss of protein. After gel filtration, protein concentration was determined by UV-HPLC and showed that 81% of the original protein mass was collected.

^{177}Lu (molar activity = 48 MBq/nmol) in 0.05 mM HCl (Perkin Elmer) was dried at 135 ˚C and re-suspended in 60 µL 0.1 M HNO_3 and neutralized by addition of 30 µL 300 mM Na-HEPES. The activity was added to the protein and this was allowed to react for at least 1.5 hours at 35 ˚C before addition of 100 µL 50 mM EDTA in H_2O. EDTA was added in >250-fold excess as a ^{177}Lu scavenger to complex any remaining unlabeled ^{177}Lu. After an additional 30 minutes at 35 ˚C, the labeled protein was purified by gel filtration on the same PD-10 column used earlier. This efficiently removes the ^{177}Lu-EDTA from the protein. Subsequent UV-HPLC analysis showed a loss in protein mass of 36% in this purification step, resulting in an overall loss of protein mass of 48% from start to finish. The ^{177}Lu activity was determined using a calibrated Ge(Li)-detector.

The specific activity of the labeled protein was 482 ± 101 MBq/mg (n = 3). The highest specific activity attainable given the molar activity of the ^{177}Lu (48 MBq/nmol) and the conjugation yield of 17.5 nmol/mg is 840 MBq/mg. The difference in these two numbers can be due to metal impurities in solvents and columns as well as metal contaminants with affinity for cDTPA in the stock ^{177}Lu other than ^{nat}Lu.

Gel-electrophoresis (SDS-PAGE) was performed on the ^{177}Lu-ASIS under non-reducing conditions according to the standard Bio-rad protocol on a Protean mini tetra 2 precast gel. This showed only one visible band at approx. 50 kDa proving the ASIS still intact and non-aggregated after the labeling procedure.

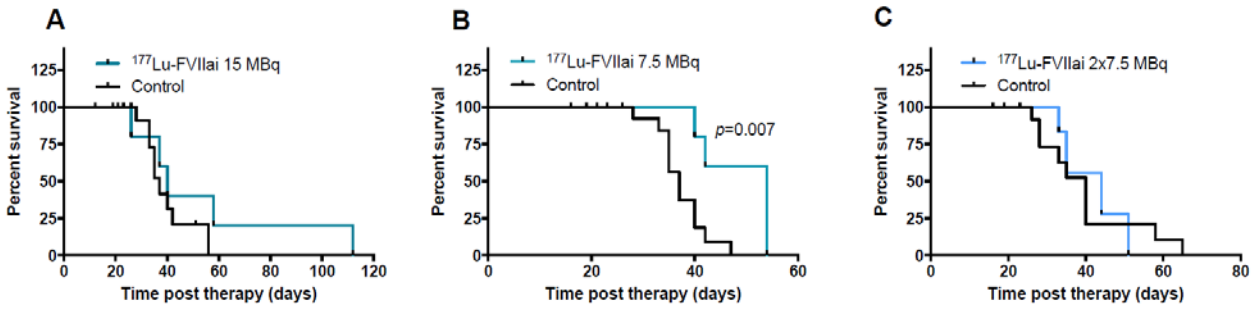

Figure 38: Treatment of mice bearing BxPC-3 tumors with ^{177}Lu-ASIS. A) Treatment with 15 MBq ^{177}Lu-ASIS had a no influence on survival. B) There was a significant increase in the survival of mice treated with 7.5 MBq ^{177}Lu-ASIS compared with the controls (p=0.007; Log-rank test). C) Treatment with 2x7.5 MBq ^{177}Lu-ASIS had a no influence on survival. N=8-16/group. From poster (Abstract nr. 5203) presented at AACR Annual Meeting 2017.

The therapeutic study showed a significant increase in survival in animals receiving a single 7.5 MBq treatment with ^{177}Lu-ASIS, whereas 2 × 7.5 MBq and 1 × 15 MBq did not show increased survival (Figure 38).

Discussion

The developed labeling method proved efficient and reproducible. The result of the therapeutic study however, is difficult to interpret. In the study, only the cohort receiving the lowest dose had increased survival. This does not intuitively make sense, unless the reduced survival in the two high dose cohorts (A and C in Figure 38) is a direct consequence of the increased dose. Noticing the survival curve of the control group in the low dose cohort (B in Figure 38), it is clear that this group has shorter survival than the control groups in the two high dose cohorts. This could be the explanation for the significant increase in survival, observed in the low dose cohort.

6. Introduction to *in vivo* generators

Continuing with the aim of developing diagnostic and therapeutic radionuclides, the concept of in vivo generators was explored. In 1989, Mausner introduced the idea of targeted radionuclide therapy, using long-lived parent radioisotopes labeled to antibodies and relying on the short-lived daughters' high-energy emissions for the therapeutic dose. In this way, the therapeutic daughter is produced from the parent decay *in vivo*, giving rise to the name *in vivo* generators. There is a clear inverse correlation between the half-life of a β-emitter and the mean energy of the emitted β-particle, meaning that very high β-energies are exclusive to isotopes with half-life too short for large vectors like antibodies to achieve optimal distribution. This correlation can be circumvented by utilizing *in vivo* generators. As very short-lived, high energy daughters can have a long half-life parent, this parent isotope can be bound to the vector, effectively prolonging the daughter half-life[132].

For therapeutic daughters, a very important consideration is the chemical consequence of the parent decay. The change from parent to daughter element, can cause drastic changes in chemistry, but even when the parent and daughter chemistry are almost identical (like in the row of lanthanides), parent decay can cause release of the daughter. In general, the rule is that even when the daughter has similar affinity for the parent chelator, α, EC and IC decay will cause the daughter to dislocate, while β and IT decay will not[133–135]. This chemical effect is exactly what was utilized to produce ^{165}Er above, causing ^{165}Er to dislocate from DOTA.

6.1 Paper VIII

The paper "*In Vivo* Radionuclide Generators for Diagnostics and Therapy" reviews in detail the field of *in vivo* generators.

6.2 Paper IX

The dislocation of the daughter, commonly considered problematic, could however have diagnostic potential. We decided to test if the daughter released subsequent to EC decay, could be utilized to quantify vector internalization. If a vector is bound to the surface of a targeted cell, then upon parent decay, the daughter would diffuse away from the cell before decaying. If the vector was internalized prior to the parent decay, the daughter would be trapped and decay inside the cell.

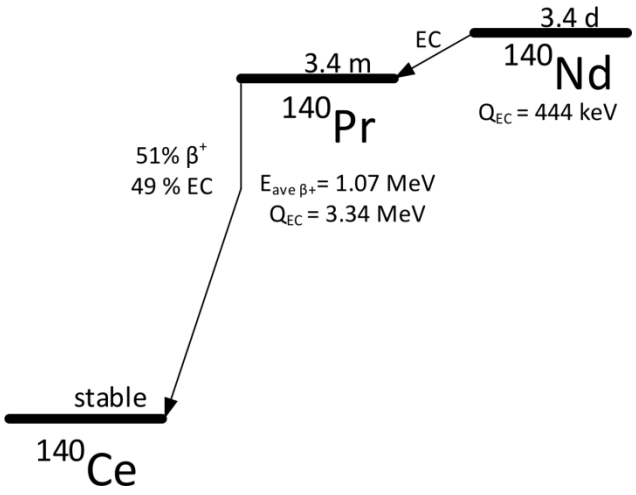

Figure 39: Simplified decay scheme for ^{140}Nd[136].

The isotope ^{140}Nd ($T_{½}$ = 3.37 d) decays by EC to the short-lived daughter ^{140}Pr ($T_{½}$ = 3.4 min) which is a β+ emitter allowing PET imaging (Figure 39). ^{140}Nd was labelled to the vectors DOTA-TATE and DOTA-LM3 which are both specific for somatostatin receptors (overexpressed on a number of neuroendocrine tumors). DOTA-TATE is known to internalize, whereas DOTA-LM3 does not internalize upon binding [137,138]. The labeled vectors were then injected into mice, which were scanned over several time-points. After 24 hours, the animals were sacrificed and scanned again. If the vector was on the cell surface, then the *in vivo* PET signal was assumed to be non-localized. This is because the PET isotope would have moved into circulation and away from the tumor. If the vector was internalized, the PET signal was assumed to be localized to the tumor. The real localization of the DOTA-TATE and DOTA-LM3 was imaged post-mortem, because without blood flow there was no mechanism to separate the parent and daughter decays (Figure 40).

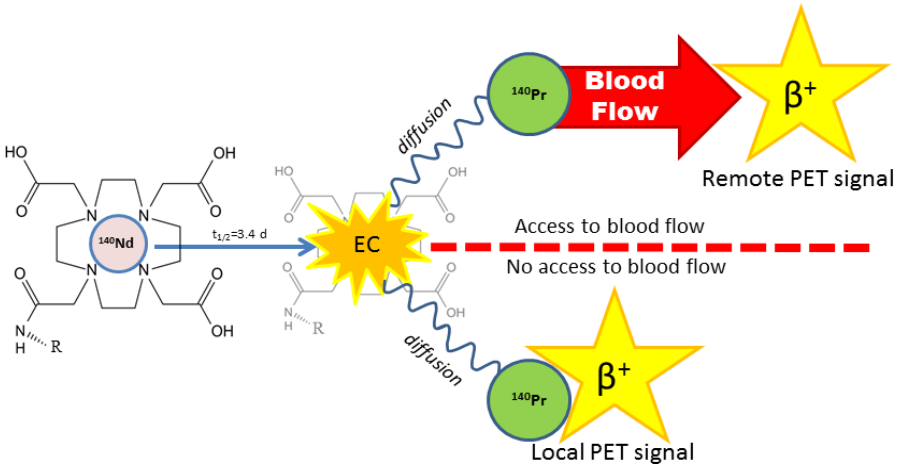

Figure 40: Illustration of the concept when using ^{140}Nd as a PET isotope. If the ^{140}Pr daughter is released into circulation, the ^{140}Pr ion will be moved from the site of parent decay before it decays. If the ^{140}Nd decays after internalization or the daughter otherwise is restricted from reaching the blood, the resulting daughter decay will occur in close proximity to the parent decay and thus in close proximity to the vector.

^{140}Nd production

^{140}Nd as well as ^{134}Ce was used during the project and both radioisotopes were produced at the ISOLDE facility at CERN. ^{134}Ce is only available via exotic production routes, hence its placement on the isotope map far from stability and surrounded by several isotopes of similar half-life. Proton irradiation of the nearest stable neighbor ^{136}Ce would indeed yield ^{134}Pr, which with a half-life of only 18 minutes would produce the daughter ^{134}Ce. However, it would be impossible to separate the produced ^{134}Ce from the ^{136}Ce starting material. A different strategy could be irradiating either ^{nat}La or enriched ^{138}La with high energy protons relying on the reactions ^{nat}La(p,xn)^{134}Ce or ^{138}La(p,5n)^{134}Ce. The issue with both is that irradiations at energies high enough to yield (p,5n) and (p,6n) reactions are not very specific and will thus also yield significant amounts of the neighboring nuclides. ^{140}Nd can, unlike ^{134}Ce, be produced on a small medical cyclotron by proton irradiation of naturally occurring monoisotopic Pr. For ^{140}Nd the difficulties are thus not producing the isotope but separating it from the bulk target material. Separation of neighboring lanthanides is, as mentioned, a very inefficient and time-consuming task.

The ISOLDE radioactive beam facility (Isotope Separator On-Line DEtector) is located at CERN on the PS Booster. The facility has since 1967 delivered radioactive beams and isotopes for applications within

nuclear, solid-state, bio- and astrophysics. The facility utilizes the beam surplus available from the PS Booster and receives 1.4 GeV protons at beam currents up to 2 μA[139,140].

The primary reaction at 1.4 GeV is spallation. The spallation process is triggered as high-energy protons collide with nucleons in target nuclei thus transferring its energy and leaving the target nuclei in highly excited states. The excited nucleus releases excess energy by evaporation of nucleons. Because protons have to cross the coulomb barrier, the nucleus preferentially evaporates neutrons, resulting in the proton rich reaction products. The process can be analogized by a hot Irish coffee, which cools by preferential evaporation of the more volatile component, e.g. alcohol. The highly proton rich products will then beta decay towards stability[141,142].

The target in which the reactions take place is a thin tantalum tube. The tube is ohmicly heated to approximately 2000 ˚C by running a constant DC current of 640 A over it. This extreme heat causes the produced isotopes to diffuse to the tantalum surface from which they evaporate into the tube cavity. From here, they are ionized and accelerated out of the tube and into the mass separator. The ionization process can be improved by laser ionization in which 2-4 laser beams are shined through the tantalum tube, carefully tuned to ionize a specific element in a stepwise manner. This specific ionization technique not only increases the intensity of the radioactive beam, it also improves the purity by preferentially ionizing the requested isotope, causing the ratio to contaminants to increase.

Upon leaving the mass-separator, the isotopes are deposited in a thin Zn film deposited on a gold foil. Zn is used as it is easily dissolved and separated from the lanthanide product and the gold backing used because of its inertness[139].

The paper draft “Neodymium-140 as an *in vivo* generator for preclinical positron emission tomography” is attached.

Discussion

The results of the small animal tests showed a significant difference in pre- and post-mortem scans for the non-internalized DOTA-LM3. In the study, we showed that the non-internalizing tracer ^{140}Nd-DOTA-LM3 accumulates in the pancreas and releases $^{140}Pr^{3+}$ into the blood stream where it quickly redistributes to the liver and lungs. We hope that further work will lead to the development of PET probes using ^{140}Nd as the radiolabel that allows quantification of internalization. The experimental set up described here using pre- and post-mortem imaging should facilitate that development. Determining the internalized fraction might prove possible by comparison of target to lung ratio, if the used vector does not have lung uptake. Having the ability to quantify the tissue dependent internalization of pharmaceuticals using PET would provide a valuable tool in drug delivery investigations of designs where cellular internalization is crucial to drug action.

For this technique to be relevant, the isotope production cannot rely on the exotic production routes available at CERN/ISOLDE. To be readily available for research the ^{140}Nd must be able to be produced on demand and in larger quantities, not to mention at a lower cost. Therefore, there is probably no way around performing the α-HIBA separation. While this might have been detrimental in the case of ^{165}Er, the longer half-life of ^{140}Nd can allow the associated time-consumption.

7. Discussion

7.1 Measurement of dose in targeted radionuclide therapy

When performing radionuclide therapy, dose fractionation and monitoring is not performed to nearly the same degree as in external beam radiotherapy. This is not because the benefits of fractionation would not apply in targeted radionuclide therapy, but rather because these procedures are inherently associated with large uncertainty in estimates of tumor uptake. Commonly used therapeutic isotopes do not have a β^+ branch, and concurrent imaging therefore has to be performed using SPECT imaging instead of quantitative PET imaging. One way of assessing the expected dosimetry is by performing PET scans prior to therapy using the same vector with a diagnostic isotope attached. This is done when treating with ^{177}Lu-DOTA-TATE, where ^{64}Cu-DOTA-TATE is used for PET scanning to quantify the uptake before administration of the therapeutic. Several intact antibodies have been used as vectors in targeted radionuclide therapy using both β^-- and α-emitters to deliver the therapeutic dose. For intact antibodies, the highest tumor uptake is typically seen 3-4 days post injection. To trace the distribution and verify expression of the target on all lesions prior to therapy, long-lived isotopes like ^{89}Zr and ^{52}Mn are necessary, seeing how patient dosimetry does not favor ^{64}Cu for scanning later than two days post injection (Figure 10 & Figure 11).

Pre-treatment imaging in Auger therapy is more complicated. It is of course possible to substitute the Auger emitter for a chemically similar PET radionuclide and evaluate the uptake in the tumor. The issue is that the very short range of Auger-electrons, necessitates internalization of the vector for optimal therapy. Therefore, an image showing quantifiable tumor uptake is not sufficient for reliable prognosis of the efficacy. The isotopes ^{140}Nd and ^{134}Ce however, could possibly deliver the relevant information, as the delayed PET signal from the decaying daughters should allow quantification of the internalized fraction. This would be a valuable tool in the potential move from pre-clinical to clinical use of Auger therapy. Furthermore, the technique could also be used when considering therapy using any of the α-emitters with a chain of radioactive daughters like ^{225}Ac and ^{223}Ra. If the isotope is internalized, the risk of redistribution of radioactive daughters is most likely severely reduced. Thus, a pre-treatment PET scan using ^{140}Nd or ^{134}Ce could estimate the expected extent of redistribution of the radioactive daughters.

7.2 Receptor saturation in Auger therapy

Although the main parameter to consider when choosing a radionuclide for therapy is the associated dose to normal tissue, one could imagine an isotope with emissions so low in energy that it would be impossible to target a sufficient number of nuclei to the target cell. This is indeed a real concern since delivery requires the presence of a certain receptor or cell surface moiety. As these, at least to some degree, are consumed as the specific vectors bind, the number of available receptors must at least be equal to the number of vectors needed to deliver the lethal dose. An approach to estimating if the required uptake can be reached is to review reported uptake values from literature. Here antibodies and antibody-derived formats tend to excel, exhibiting very high and specific uptake. In a recent 2014 paper by Marquez et al. they report 173 %id/g uptake of the HER2 specific antibody pertuzumab, with an injected activity of 3.7 MBq of ^{89}Zr[143]. Assuming 10^8 cells/g [144] this results in

$$No\ of\ nuclei\ delivered\ per\ cell = {1.73 \times 3.7\ MBq}\Big/{\lambda_{^{89}Zr}} \times 10^8 = 2.6 \times 10^4$$

This number of nuclides of ^{135}La corresponds to an activity of 0.26 Bq and if placed in the nucleus, a total dose of 33.6 Gy when integrated over the lifetime of the radionuclide ($N \leftarrow N$ calculated in MIRDCell [115]). The data from Marquez et al. furthermore has a labeled molar activity of only 11.1 GBq/µmol chelator. The ^{135}La produced in this thesis has a molar activity of 70 GBq/µmol and therefore the uptake corresponds to not 0.26 Bq but 1.62 Bq. Also important, is that calculating average cell uptake based on a value like the ^{89}Zr-pertuzumab %ID/g and using that to estimate the uptake capacity of a single cell is not entirely fair. In a solid tumor, not all individual cells have perfect access to the vector due to suboptimal perfusion inside the tissue. Disseminated single cells and micro-metastasis, however, will have much better access to the surrounding blood, and thus an expected uptake that is higher than reported for solid tumors.

7.3 The importance of specific activity

Unfortunately, not all targets can be expected to be expressed as highly as HER2, which in several cell lines have > 10^6 copies per cell [145]. When the number of targets per cell is much lower, the importance of specific activity increases, as a higher fraction of the available receptors is needed to deliver the necessary dose. Therefore, specific activity is, especially within therapy but also in diagnostics, of great importance. In therapeutic applications, the dose that can be delivered to the target is often directly proportional to the specific activity of the therapeutic radioisotope used [146]. In diagnostic scans, the specific activity can dictate the attained target-to-background signal ratio.

A limitation in all radiometal production is the presence of metal contaminants in the starting materials. Most solvents can be obtained in very high purity or can be stored with metal binding resins to remove impurities. Nonetheless, when performing isotope separations requiring large volumes of solvent, contaminants will accumulate over the course of the separation. The bigger issue however, is metal contaminants in the target material. These target materials are typically only available from a very limited number of suppliers, and commonly have significant amounts of competing metal impurities. Those that are not eliminated during the separation procedure will affect subsequent labeling yields. The impurities can be removed by performing a “cold” separation and the separated target material reused either in an electroplated target or as a pressed powder target. This however, is impractical as not all metals are easily electroplated, and because irradiation of the salts is associated with reduced production yields due to poor heat conductivity and isotopic dilution.

Another way to optimize specific activity is to irradiate longer or at higher beam-currents. If more activity is produced in the same target mass, the specific activity is expected to scale linearly with the produced activity. Irradiating at higher beam-currents further have the benefit of higher production rates and thus increased production capability. The targets used in this work have been first generation targets, and have not been optimized for high beam currents. With careful optimization, it should be possible to at least double or triple the production capability.

7.4 RBE of Auger electrons

One major obstruction for the further development of Auger-based therapy is the lack of an appropriate dosimetry model. Many groups have measured the RBE of Auger emitters, but the RBE may not be a great way to characterize the effectiveness of these radioisotopes. Measuring RBE requires knowledge of the dose delivered to the cells. For both α- and β-emitters, the dose can be said to be uniform through volumes the size of cells because the range of these particles are much larger

than the cell diameter. In other words, a known volume can be exposed to a dose that is uniformly distributed over the entire volume, and the effect this irradiation has on that very volume can be assessed. This makes the comparison easy, and the RBE can be measured simply by measuring which dose is needed to kill a certain percentage of the cells in a culture. The problem, when trying to measure the RBE of Auger emitters, is that the ranges of the lowest energy Auger electrons are far shorter than the size of the cell. Therefore, any vector used that does not exhibit uniform cellular distribution will have enormous effect on the resulting RBE measured. Therefore, an RBE measured for an Auger emitter is not just the RBE of the isotope, but the BRE of the entire vector-radioisotope-construct.

The high importance of the intracellular distribution of the Auger emitters for inducing optimal damage to the cell also hints at an important benefit of Auger therapy. The extremely localized damage of Auger emitters should spare non-targeted tissues like liver, kidneys, and spleen: all commonly highly exposed in targeted radionuclide therapy. Verifying this hypothesis would be an important part of the overall argument for use of Auger emitters.

7.5 Clinical outlook

The ability to produce a new tracer with proven benefits for diagnosis of a specific illness, is not always enough to make a clinical product. There are many constricting factors to overcome. The imaging of intact antibodies serves as an example:

In recent years there has been a lot of attention put on radiometal based antibody imaging, following the increasing number of antibody based cancer therapies like Trastuzumab (Herceptin) targeting the HER2 receptor, Bevacizumab (Avastin) targeting VEGF etc. [84,147–150]. Seeing that the receptor phenotype of the primary tumor established via histology is not always conserved in all metastatic lesions [151], there is a need to map out the receptor availability on all lesions to assess the expected efficacy, before starting the treatment. Such an evaluation is at first glance simple. The hospitals of interest would already have the antibody in question. An appropriate isotope like ^{89}Zr is commercially available, as is the appropriate bifunctional chelator p-NCS-Bz-DFO[152]. Furthermore, the conjugation strategy is based on robust and well-tested methods making the whole process readily available for the hospital radiochemists. So why is it not done?

First, one cannot just go ahead and attach a radioisotope to an antibody, and administer the cocktail to a patient. It all has to be done within the framework of good manufacturing practice (GMP). This requires rigorous testing and validation of all associated procedures and materials used, as well as large amounts of paperwork to be filed and approved by authorities before the needed permits can be obtained. This process is highly time consuming and expensive. Furthermore, the approval given needs to be maintained with scheduled tests and revalidations, resulting in a sustained cost associated with each approval. This cost, i.e. the initial cost plus the sustained cost needs to be multiplied by the number of antibodies used in cancer therapy at the hospital, seeing that each will need an individual approval. This all sums up to many hours and a lot of money spent, and since the high cost of these drugs is a heavy weighing part of the argument for pre-treatment imaging, this financial argument is difficult to get around.

Secondly, a high throughput of patients is needed, not only to make it financially feasible but also to ensure the diagnostic certainty of the examination. Even though antibodies have unparalleled

specificity and uptake, interpretation of diagnostic images is not always trivial. The biological targets of antibodies are not exclusively available but merely overexpressed in tumor tissue and thorough understanding of the normal uptake and common artefacts is needed for the physician to correctly evaluate the PET data. This skill takes months to acquire even for high throughput tracers.

Finally, getting the high patient throughput needed to make the examination economically feasible and to acquire the degree of specialized medical knowledge needed requires that the new examination is given priority over other important examinations. Capacity in PET departments is already stretched, and priority is typically given to more versatile tracers that not only have a larger patient base, but also have a wider array of uses.

So, are all highly specialized tracers redundant? No, but the use of these requires a high level of local specialization in single departments receiving their patient base from large geographical areas. This does not mean that patients need to travel across the country, but that the tracer has a half-life that allows its shipping nationwide and a digital framework that allows a few specialized doctors to evaluate all images.

Even though dosimetry is weighted heavily in this thesis, dosimetry's importance is only critical in clinical applications. Therefore, an isotope like ^{52}Mn, which only in special cases would be considered for human use, is nonetheless an important radionuclide for preclinical and pharmaceutical investigations. Here the dosimetry does not matter as long as the doses are below the threshold for acute damage. Properties that *do* matter are of a more practical nature, such as availability, versatility, image resolution, chemical behavior, and ease of handling. All except the first are properties in which ^{52}Mn excels. It has simple labeling chemistry and is stably complexed in the ubiquitous chelator DOTA, it has a very low β^+ energy resulting in excellent image resolution similar to what can be obtained using ^{18}F, and the long half-life of 5.59 days allows for time-consuming chemistry if needed. The 5.59 d half-life complies with worldwide shipping while also allowing for only bi-weekly deliveries. Unfortunately, there is currently no commercial supplier, most likely because isotope development is primarily performed with the aim of clinical use. This example highlights the importance of continued development of new radioisotopes for research.

The same applies for the therapeutic isotopes. Due to the constant improvements in vector designs, the arguments for using targeted radionuclide therapy will only get stronger in the future. Currently, vectors capable of delivering a radioisotope directly to the DNA or even just to the target cell nuclei, are not available. However, this does not render the development of the Auger emitters useless. It will only be a matter of time before these vectors do exist, and at that point, established methods for production of the Auger emitting isotopes will be necessary. For now, the continued interest and development in Auger emitters inspires continued efforts in developing the needed vectors, thus moving the field forward towards pinpoint-accurate Auger therapy.

8. References

[1] Brown GD, Denning DW, Gow NAR, Levitz SM, Netea MG, White TC. Hidden Killers: Human Fungal Infections. Sci Transl Med 2012;4:1–9. doi:10.1126/scitranslmed.3004404.

[2] Denning DW. Invasive Aspergillosis. Clin Infect Dis 1998;26:781–803. doi:10.1086/513943.

[3] Denning DW, Pleuvry A, Cole DC. Global burden of allergic bronchopulmonary aspergillosis with asthma and its complication chronic pulmonary aspergillosis in adults. Med Mycol 2013;51:361–70. doi:10.3109/13693786.2012.738312.

[4] Prattes J, Flick H, Prüller F, Koidl C, Raggam RB, Palfner M, et al. Novel tests for diagnosis of invasive aspergillosis in patients with underlying respiratory diseases. Am J Respir Crit Care Med 2014;190:922–9. doi:10.1164/rccm.201407-1275OC.

[5] Thornton CR. Development of an immunochromatographic lateral-flow device for rapid serodiagnosis of invasive aspergillosis. Clin Vaccine Immunol 2008;15:1095–105. doi:10.1128/CVI.00068-08.

[6] Rolle A-M, Hasenberg M, Thornton CR, Solouk-Saran D, Männ L, Weski J, et al. ImmunoPET/MR imaging allows specific detection of Aspergillus fumigatus lung infection in vivo. Proc Natl Acad Sci U S A 2016;113:E1026-33. doi:10.1073/pnas.1518836113.

[7] Cutler CS, Hennkens HM, Sisay N, Huclier-Markai S, Jurisson SS. Radiometals for combined imaging and therapy. Chem Rev 2013;113:858–83. doi:10.1021/cr3003104.

[8] Price EW, Orvig C. Matching chelators to radiometals for radiopharmaceuticals. Chem Soc Rev 2014;43:260–90. doi:10.1039/c3cs60304k.

[9] Kassis AI. Therapeutic Radionuclides: Biophysical and Radiobiologic Principles. Semin Nucl Med 2008;38:358–66. doi:10.1053/j.semnuclmed.2008.05.002.

[10] de Kruijff RM, Wolterbeek HT, Denkova AG. A critical review of alpha radionuclide therapy-how to deal with recoiling daughters? Pharmaceuticals 2015;8:321–36. doi:10.3390/ph8020321.

[11] CYCLOTRONS USED IN NUCLEAR MEDICINE WORLD MARKET REPORT & DIRECTORY. MEDraysintell 2015.

[12] Lawrence EO. Method and apparatus for the acceleration of ions, 1934.

[13] International Atomic Energy Agency. Cyclotron Produced Radionuclides : Physical Characteristics and Production Methods. TRS-468. October 2009:279.

[14] Schlyer DJ, Van den Winkel P, Ruth TJ, Vora MM, Pillai M, Haji-Saeid M. Cyclotron produced radionuclides: Principles and practice 2009:215.

[15] West HI, Lanier RG, Mustafa MG. 52Cr(p,n)52Mn g,m and 52Cr(d,2n)52Mn g,m excitation functions. Phys Rev C 1987;35:2067–76. doi:10.1103/PhysRevC.35.2067.

[16] Ziegler JF, Ziegler MD, Biersack JP. SRIM - The stopping and range of ions in matter (2010). Nucl Instruments Methods Phys Res Sect B Beam Interact with Mater Atoms 2010;268:1818–23. doi:10.1016/j.nimb.2010.02.091.

[17] Chelation. IUPAC Compend. Chem. Terminol., vol. 1077, Research Triagle Park, NC: IUPAC;

1994, p. 2014. doi:10.1351/goldbook.C01012.

[18] Zeglis BM, Houghton JL, Evans MJ, Viola-Villegas N, Lewis JS. Underscoring the influence of inorganic chemistry on nuclear imaging with radiometals. Inorg Chem 2014;53:1880–99. doi:10.1021/ic401607z.

[19] Vosjan MJWD, Perk LR, Visser GWM, Budde M, Jurek P, Kiefer GE, et al. Conjugation and radiolabeling of monoclonal antibodies with zirconium-89 for PET imaging using the bifunctional chelate p-isothiocyanatobenzyl-desferrioxamine. Nat Protoc 2010;5:739–43. doi:10.1038/nprot.2010.13.

[20] Lin M, Welch MJ, Lapi SE. Effects of Chelator Modifications on 68Ga-Labeled [Tyr3]Octreotide Conjugates. Mol Imaging Biol 2013;15:606–13. doi:10.1007/s11307-013-0627-x.

[21] Bartholomä MD, Louie AS, Valliant JF, Zubieta J. Technetium and gallium derived radiopharmaceuticals: Comparing and contrasting the chemistry of two important radiometals for the molecular imaging era. Chem Rev 2010;110:2903–20. doi:10.1021/cr1000755.

[22] Hancock RD. Chelate ring size and metal ion selection. The basis of selectivity for metal ions in open-chain ligands and macrocycles. J Chem Educ 1992;69:615–21. doi:10.1021/ed069p615.

[23] Liu S, Edwards DS. Bifunctional Chelators for Therapeutic Lanthanide Radiopharmaceuticals. Bioconjug Chem 2001;12:7–34. doi:10.1021/bc000070v.

[24] Abou DS, Ku T, Smith-Jones PM. In vivo biodistribution and accumulation of 89Zr in mice. Nucl Med Biol 2011;38:675–81. doi:10.1016/j.nucmedbio.2010.12.011.

[25] City K, City K. Relation between the location of elements in the periodic table and tumor-uptake rate. Int J Nucl Med Biol 1985;12:167–74.

[26] Wooten AL, Aweda TA, Lewis BC, Gross RB, Lapi SE. Biodistribution and PET Imaging of pharmacokinetics of manganese in mice using Manganese-52. PLoS One 2017;12:1–14. doi:10.1371/journal.pone.0174351.

[27] Holland JP, Evans MJ, Rice SL, Wongvipat J, Sawyers CL, Lewis JS. Annotating MYC status with 89Zr-transferrin imaging. Nat Med 2012;18:1586–91. doi:10.1038/nm.2935.

[28] Jones DW, MacDonald J, Hogg P. Nuclear Medicine Imaging n.d. http://radiologykey.com/nuclear-medicine-imaging-2/.

[29] eurostat. Healthcare resource statistics - technical resources and medical technology - Statistics Explained n.d. http://ec.europa.eu/eurostat/statistics-explained/index.php/Healthcare_resource_statistics_-_technical_resources_and_medical_technology (accessed May 20, 2017).

[30] Rahmim A, Zaidi H. PET versus SPECT: strengths, limitations and challenges. Nucl Med Commun 2008;29:193–207. doi:10.1097/MNM.0b013e3282f3a515.

[31] Miller PW, Long NJ, Vilar R, Gee AD. Synthesis of11C, 18F, 15O, and 13N radiolabels for positron emission tomography. Angew Chemie - Int Ed 2008;47:8998–9033. doi:10.1002/anie.200800222.

[32] Bushberg J, Seibert J, Leidholdt E, Boone J. The Essential Physics of Medical Imaging. vol. 30. Lippincott Williams & Wilkins; 2002. doi:ISBN: 978-0-7817-8057-5.

[33] Bolch WE, Eckerman KF, Sgouros G, Thomas SR. MIRD Pamphlet No. 21: A Generalized Schema for Radiopharmaceutical Dosimetry--Standardization of Nomenclature. J Nucl Med 2009;50:477–84. doi:10.2967/jnumed.108.056036.

[34] Wrixon AD. New ICRP recommendations. J Radiol Prot 2008;28:161–8. doi:10.1088/0952-4746/28/2/R02.

[35] Stabin MG, Sparks RB, Crowe E. OLINDA/EXM: The Second-Generation Personal Computer Software for Internal Dose Assessment in Nuclear Medicine. J Nucl Med 2005;46:1023–7. doi:46/6/1023 [pii].

[36] Jødal L, Le Loirec C, Champion C. Positron range in PET imaging: an alternative approach for assessing and correcting the blurring. Phys Med Biol 2012;57:3931–43. doi:10.1088/0031-9155/57/12/3931.

[37] Ghotbi AA, Kjær A, Hasbak P. Review: Comparison of PET rubidium-82 with conventional SPECT myocardial perfusion imaging. Clin Physiol Funct Imaging 2014;34:163–70. doi:10.1111/cpf.12083.

[38] Blower PJ. A nuclear chocolate box: the periodic table of nuclear medicine. Dalt Trans 2015;44:4819–44. doi:10.1039/C4DT02846E.

[39] Pautler RG, Silva AC, Koretsky AP. In vivo neuronal tract tracing using manganese-enhanced magnetic resonance imaging. Magn Reson Med 1998;40:740–8. doi:10.1002/mrm.1910400515.

[40] Saleem KS, Pauls JM, Augath M, Trinath T, Prause BA, Hashikawa T, et al. Magnetic resonance imaging of neuronal connections in the Macaque Monkey. Neuron 2002;34:685–700. doi:10.1016/S0896-6273(02)00718-3.

[41] Crossgrove J, Zheng W. Manganese toxicity upon overexposure. NMR Biomed 2004;17:544–53. doi:10.1002/nbm.931.

[42] Koretsky AP, Silva AC. Manganese-enhanced magnetic resonance imaging (MEMRI). NMR Biomed 2004;17:527–31. doi:10.1002/nbm.940.

[43] Silva AC, Lee JH, Aoki I, Koretsky AP. Manganese-enhanced magnetic resonance imaging (MEMRI): Methodological and practical considerations. NMR Biomed 2004;17:532–43. doi:10.1002/nbm.945.

[44] Lin Y, Koretsky AP. Manganese ion enhances T1-weighted MRI during brain activation: an approach to direct imaging of brain function. Magn Reson Med 1997;38:378–88. doi:10.1002/mrm.1910380305.

[45] Garrick MD, Dolan KG, Horbinski C, Ghio AJ, Higgins D, Porubcin M, et al. DMT1: A mammalian transporter for multiple metals. BioMetals 2003;16:41–54. doi:10.1023/A:1020702213099.

[46] Au C, Benedetto A, Aschner M. Manganese transport in eukaryotes: The role of DMT1. Neurotoxicology 2008;29:569–76. doi:10.1016/j.neuro.2008.04.022.

[47] Narita K, Kawasaki F, Kita H. Mn and Mg influxes through Ca channels of motor nerve terminals are prevented by verapamil in frogs. Brain Res 1990;510:289–95. doi:10.1016/0006-8993(90)91379-U.

[48] Lewis CM, Graves S a, Hernandez R, Valdovinos HF, Barnhart TE, Cai W, et al. (52)Mn Production for PET/MRI Tracking Of Human Stem Cells Expressing Divalent Metal Transporter

1 (DMT1). Theranostics 2015;5:227–39. doi:10.7150/thno.10185.

[49] Antkowiak PF, Stevens BK, Nunemaker CS, McDuffie M, Epstein FH. Manganese-enhanced magnetic resonance imaging detects declining pancreatic β-cell mass in a cyclophosphamide-accelerated mouse model of type 1 diabetes. Diabetes 2013;62:44–8. doi:10.2337/db12-0153.

[50] Buchholz M, Spahn I, Coenen HH. Optimized separation procedure for production of no-carrier-added radiomanganese for positron emission tomography. Radiochim Acta 2015;0:893–9. doi:10.1515/ract-2015-2506.

[51] Buchholz M, Spahn I, Scholten B, Coenen HH. Cross-section measurements for the formation of manganese-52 and its isolation with a non-hazardous eluent. Radiochim Acta 2013;101:491–9. doi:10.1524/ract.2013.2083.

[52] Lahiri S, Nayak D, Korschinek G. Separation of No-Carrier-Added 52 Mn from Bulk Chromium : A Simulation Study for Accelerator Mass Spectrometry Measurement of 53 Mn 2006;78:7517–21.

[53] Klein ATJ, Rösch F, Coenen HH, Qaim SM. Production of the positron emitter 51Mn via the 50Cr(d, n) reaction: Targetry and separation of no-carrier-added radiomanganese. Radiochim Acta 2002;90:167–77.

[54] Dong Y, Junde H. Nuclear Data Sheets for A = 52. Nucl Data Sheets 2015;128:185–314. doi:10.1016/j.nds.2015.08.003.

[55] Xiaolong H. Nuclear Data Sheets for A = 51. Nucl Data Sheets 2006;107:2131–322. doi:10.1016/j.nds.2006.07.002.

[56] Singh B. Nuclear Data Sheets for A = 89. Nucl Data Sheets 2013;114:1–208. doi:10.1016/j.nds.2013.01.001.

[57] Katakura J, Wu ZD. Nuclear Data Sheets for A = 124. Nucl Data Sheets 2008;109:1655–877. doi:10.1016/j.nds.2008.06.001.

[58] Levkovskij VN. Cross Sections of Medium Mass Nuclide Activation (A= 40–100) by Medium Energy Protons and Alpha Particles (E= 10–50 MeV). Inter-Vesi, Moscow, USSR 1991.

[59] Wooten AL, Lewis BC, Lapi SE. Cross-sections for (p,x) reactions on natural chromium for the production of 52,52m,54Mn radioisotopes. Appl Radiat Isot 2015;96:154–61. doi:10.1016/j.apradiso.2014.12.001.

[60] Cotton F a., Wilkinson G. Advanced Inorganic Chemistry: A Comprehensive Text. 1980. doi:10.1016/j.jaap.2011.11.019.

[61] Pietrzyk D. Anion exchange separations of metal ions in partially nonaqueous solutions. Retrosp Theses Diss 1960;Paper 2390.

[62] Missy P, Lanhers MC, Grignon Y, Joyeux M, Burnel D. In vitro and in vivo studies on chelation of manganese. Hum Exp Toxicol 2000;19:448–56. doi:10.1191/096032700682694260.

[63] Tandon SK, Singh J. Removal of manganese by chelating agents from brain and liver of manganese treated rats: An in vitro and an in vivo study. Toxicology 1975;5:237–41. doi:10.1016/0300-483X(75)90120-1.

[64] Maynard LS, Fink S. THE INFLUENCE OF CHELATION ON RADIOMANGANESE EXCRETION IN MAN AND MOUSE 1. J Clin Invest 1956;35:831–6. doi:10.1172/JCI103336.

[65] Drahoš B, Kubíček V, Bonnet CS, Hermann P, Lukeš I, Tóth É. Dissociation kinetics of Mn2+ complexes of NOTA and DOTA. Dalton Trans 2011;40:1945–51. doi:10.1039/c0dt01328e.

[66] Vanasschen C, Brandt M, Ermert J, Coenen HH. Radiolabelling with isotopic mixtures of 52g/55 Mn(ii) as a straight route to stable manganese complexes for bimodal PET/MR imaging. Dalt Trans 2016;45:1315–21. doi:10.1039/C5DT04270D.

[67] Severin GW, Jørgensen JT, Wiehr S, Rolle A-M, Hansen AE, Maurer A, et al. The impact of weakly bound ^{89}Zr on preclinical studies: non-specific accumulation in solid tumors and aspergillus infection. Nucl Med Biol 2015;42:360–8. doi:10.1016/j.nucmedbio.2014.11.005.

[68] Buck A, Nguyen N, Burger C, Ziegler S, Frey L, Weigand G, et al. Quantitative evaluation of manganese-52m as a myocardial perfusion tracer in pigs using positron emission tomography. Eur J Nucl Med 1996;23:1619–27.

[69] Perk LR, Visser OJ, Stigter-Van Walsum M, Vosjan MJWD, Visser GWM, Zijlstra JM, et al. Preparation and evaluation of 89Zr-Zevalin for monitoring of 90Y-Zevalin biodistribution with positron emission tomography. Eur J Nucl Med Mol Imaging 2006;33:1337–45. doi:10.1007/s00259-006-0160-0.

[70] van Dongen G a MS, Visser GWM, Lub-de Hooge MN, de Vries EG, Perk LR. Immuno-PET: a navigator in monoclonal antibody development and applications. Oncologist 2007;12:1379–89. doi:10.1634/theoncologist.12-12-1379.

[71] Börjesson PKE, Jauw YWS, Boellaard R, De Bree R, Comans EFI, Roos JC, et al. Performance of immuno - positron emission tomography with zirconium-89-labeled chimeric monoclonal antibody U36 in the detection of lymph node metastases in head and neck cancer patients. Clin Cancer Res 2006;12:2133–40. doi:10.1158/1078-0432.CCR-05-2137.

[72] Deri MA, Zeglis BM, Francesconi LC, Lewis JS. PET imaging with 89Zr: From radiochemistry to the clinic. Nucl Med Biol 2013;40:3–14. doi:10.1016/j.nucmedbio.2012.08.004.

[73] Mustafa MG, West HI, O'Brien JH, Lanier RG, Benhamou M, Tamura T. Measurements and a direct-reaction-plus-Hauser-Feshbach analysis of the 89Y(p,n)89Zr, 89Y(p,2n)88Zr, and 89Y(p,pn)88Y reactions up to 40Mev. Phys Rev 1988;38:1624–37.

[74] McCutchan EA, Sonzogni AA. Nuclear Data Sheets for A = 88. Nucl Data Sheets 2014;115:135–304. doi:10.1016/j.nds.2013.12.002.

[75] Holland JP, Sheh Y, Lewis JS. Standardized methods for the production of high specific-activity zirconium-89. Nucl Med Biol 2009;36:729–39. doi:10.1016/j.nucmedbio.2009.05.007.

[76] Cotton SA. Titanium, zirconium and hafnium. Annu Rep Prog Chem, Sect A Inorg Chem 2007;103:137–46. doi:10.1039/b612679k.

[77] Meijs WE, Herscheid JDM, Haisma HJ, Wijbrandts R, van Langevelde F, Van Leuffen PJ, et al. Production of highly pure no-carrier added 89Zr for the labelling of antibodies with a positron emitter. Appl Radiat Isot 1994;45:1143–7. doi:10.1016/0969-8043(94)90029-9.

[78] Meijs WE, Herscheid JDM, Haisma HJ, Pinedo HM. Evaluation of desferal as a bifunctional chelating agent for labeling antibodies with Zr-89. Int J Radiat Appl Instrumentation Part 1992;43:1443–7. doi:10.1016/0883-2889(92)90170-J.

[79] Verel I, Visser GWM, Boellaard R, Stigter-van Walsum M, Snow GB, van Dongen G a MS. 89Zr immuno-PET: comprehensive procedures for the production of 89Zr-labeled monoclonal

antibodies. J Nucl Med 2003;44:1271–81.

[80] Lindmo T, Boven E, Cuttitta F, Fedorko J, Bunn PA. Determination of the immunoreactive function of radiolabeled monoclonal antibodies by linear extrapolation to binding at infinite antigen excess. J Immunol Methods 1984;72:77–89. doi:10.1016/0022-1759(84)90435-6.

[81] Graves SA, Hernandez R, Fonslet J, England CG, Valdovinos HF, Ellison PA, et al. Novel Preparation Methods of 52 Mn for ImmunoPET Imaging. Bioconjug Chem 2015;26:2118–24. doi:10.1021/acs.bioconjchem.5b00414.

[82] Ping Li W, Meyer L a, Capretto D a, Sherman CD, Anderson CJ. Receptor-binding, biodistribution, and metabolism studies of 64Cu-DOTA-cetuximab, a PET-imaging agent for epidermal growth-factor receptor-positive tumors. Cancer Biother Radiopharm 2008;23:158–71. doi:10.1089/cbr.2007.0444.

[83] Stillebroer A. ImmunoPET imaging of renal cell carcinoma with 124I-and 89Zr-labeled anti-CAIX monoclonal antibody cG250 in mice. Cancer Biother … 2013;28:510–5. doi:10.1089/cbr.2013.1487.

[84] Meijs WE, Haisma HJ, Klok RP, van Gog FB, Kievit E, Pinedo HM, et al. Zirconium-labeled monoclonal antibodies and their distribution in tumor-bearing nude mice. J Nucl Med 1997;38:112–8.

[85] Schneider DW, Heitner T, Alicke B, Light DR, McLean K, Satozawa N, et al. In Vivo Biodistribution, PET Imaging, and Tumor Accumulation of 86Y- and 111In-Antimindin/RG-1, Engineered Antibody Fragments in LNCaP Tumor-Bearing Nude Mice. J Nucl Med 2009;50:435–43. doi:10.2967/jnumed.108.055608.

[86] Peri D, Meker S, Manna CM, Tshuva EY. Different ortho and para electronic effects on hydrolysis and cytotoxicity of diamino bis(Phenolato) “Salan” Ti(IV) complexes. Inorg Chem 2011;50:1030–8. doi:10.1021/ic101693v.

[87] Tan C-P, Lu Y-Y, Ji L-N, Mao Z. Metallomics insights into the programmed cell death induced by metal-based anticancer compounds. Metallomics 2014;6:978–95. doi:10.1039/c3mt00225j.

[88] Burrows TW. Nuclear Data Sheets for A = 45. Nucl Data Sheets 2008;109:171–296. doi:10.1016/j.nds.2007.12.002.

[89] Vavere AL, Laforest R, Welch MJ. Production, processing and small animal PET imaging of titanium-45. Nucl Med Biol 2005;32:117–22. doi:10.1016/j.nucmedbio.2004.10.003.

[90] Verel I, Visser GWM, Boellaard R, Marijke ;, Walsum S-V, Snow GB, et al. 89 Zr Immuno-PET: Comprehensive Procedures for the Production of 89 Zr-Labeled Monoclonal Antibodies. J Nucl Med 2003;44:1271–81.

[91] Joyce J, Swihart A. Thyroid: Nuclear medicine update. Radiol Clin North Am 2011;49:425–34, v. doi:10.1016/j.rcl.2011.02.004.

[92] Strebhardt K, Ullrich A. Paul Ehrlich ’ s magic bullet concept : 100 years of progress. Nat Rev Cancer 2008;8:473–80.

[93] Kassis AI, Adelstein SJ. Radiobiologic principles in radionuclide therapy. J Nucl Med 2005;46:4S–12S. doi:46/1_suppl/4S [pii].

[94] Kumar C, Shetake N, Desai S, Kumar A, Samuel G, Pandey BN. Relevance of radiobiological

concepts in radionuclide therapy of cancer. Int J Radiat Biol 2016;92:173–86. doi:10.3109/09553002.2016.1144944.

[95] Alberts B, Johnson A, Lewis J, Raff M, Roberts K, Walter P. Molecular Biology of the Cell. 2002.

[96] Scheinberg DA, Strand M. Kinetic and Catabolic Considerations of Monoclonal Antibody Targeting in Erythroleukemic Mice. Cancer Res 1983;43:265–72.

[97] Gudkov S, Shilyagina N, Vodeneev V, Zvyagin A. Targeted Radionuclide Therapy of Human Tumors. Int J Mol Sci 2015;17:33. doi:10.3390/ijms17010033.

[98] Significant survival benefit for Alpharadin in prostate cancer. Oncol Times UK 2011;8:4. doi:10.1097/01.OTU.0000399899.90923.7c.

[99] Croke J, Leung E, Segal R, Malone S. Clinical benefits of alpharadin in castrate-chemotherapy-resistant prostate cancer: case report and literature review. BMJ Case Rep 2012;2012:8–11. doi:10.1136/bcr-2012-006540.

[100] Kim YS, Brechbiel MW. An overview of targeted alpha therapy. Tumor Biol 2012;33:573–90. doi:10.1007/s13277-011-0286-y.

[101] Young IS, Woodside J V. Antioxidants in health and disease. J Clin Pathol 2001;54:176–86. doi:10.1136/jcp.54.3.176.

[102] JAEA R&D Review 2007. 2007.

[103] Schofield P, Geiger B, Sim K, Einstein AJ. Annals of the ICRP 2011:1–125.

[104] Miederer M, Scheinberg DA, McDevitt MR. Realizing the potential of the Actinium-225 radionuclide generator in targeted alpha particle therapy applications. Adv Drug Deliv Rev 2008;60:1371–82. doi:10.1016/j.addr.2008.04.009.

[105] Chaudhri MA, Chaudhri MN, Nadeem Q, Jabbar Q. Production of Ac-225 with cyclotrons for generating Bi-213 for targeted alpha therapy. IFMBE Proc 2009;25:686–7. doi:10.1007/978-3-642-03474-9-193.

[106] Khabibullin AR, Karolak A, Budzevich MM, Woods LM, Martinez MV, McLaughlin ML, et al. SU-C-204-03: DFT Calculations of the Stability of DOTA-Based-Radiopharmaceuticals. Med Phys 2016;43:3314–3314. doi:10.1118/1.4955536.

[107] Rojas J V., Woodward JD, Chen N, Rondinone AJ, Castano CH, Mirzadeh S. Synthesis and characterization of lanthanum phosphate nanoparticles as carriers for 223Ra and 225Ra for targeted alpha therapy. Nucl Med Biol 2015;42:614–20. doi:10.1016/j.nucmedbio.2015.03.007.

[108] Mantel J. The beta ray spectrum and the average beta energy of several isotopes of interest in medicine and biology. Int J Appl Radiat Isot 1972;23:407–13. doi:10.1016/0020-708X(72)90107-X.

[109] O'donoghue J, Wheldon T. Targeted radiotherapy using Auger electron emitters. Phys Med Biol 1996;41.

[110] Kassis a. I. Cancer therapy with Auger electrons: are we almost there? J Nucl Med 2003;44:1479–81.

[111] Persson L. The Auger Electron Effect in Radiation Dosimetry. Health Phys 1994;67.

[112] Buchegger F, Perillo-Adamer F, Dupertuis YM, Delaloye AB. Auger radiation targeted into DNA: a therapy perspective. Eur J Nucl Med Mol Imaging 2006;33:1352–63. doi:10.1007/s00259-006-0187-2.

[113] Thisgaard H. Accelerator based Production of Auger-Electron-emitting Isotopes for Radionuclide Therapy (Risø-PhD; No. 42(EN)). 2008.

[114] O'Donoghue JA, Bardies M, Wheldon TE. Relationships between tumor size and curability for uniformly targeted therapy with beta-emitting radionuclides. J Nucl Med 1995;36:1902–9.

[115] Vaziri B, Wu H, Dhawan AP, Du P, Howell RW. MIRD pamphlet No. 25: MIRDcell V2.0 software tool for dosimetric analysis of biologic response of multicellular populations. J Nucl Med 2014;55:1557–64. doi:10.2967/jnumed.113.131037.

[116] Kim HJ, Eichinger A, Skerra A. High-affinity recognition of lanthanide(iii) chelate complexes by a reprogrammed human lipocalin 2. J Am Chem Soc 2009;131:3565–76. doi:10.1021/ja806857r.

[117] Singh B, Rodionov A a., Khazov YL. Nuclear Data Sheets for A = 135. Nucl Data Sheets 2008;109:517–698. doi:10.1016/j.nds.2008.02.001.

[118] Madelung O, Rössler U, Schulz M, editors. Barium oxide (BaO) electrical and thermal transport properties BT - II-VI and I-VII Compounds; Semimagnetic Compounds, Berlin, Heidelberg: Springer Berlin Heidelberg; 1999, p. 1–8. doi:10.1007/10681719_254.

[119] Prescher K, Peiffer F, Stueck R, Michel R, Bodemann R, Rao MN, et al. Thin-target cross sections of proton-induced reactions on barium and solar cosmic ray production rates of xenon-isotopes in lunar surface materials. Nucl Inst Methods Phys Res B 1991;53:105–21. doi:10.1016/0168-583X(91)95645-T.

[120] Tárkányi F, Ditrói F, Király B, Takács S, Hermanne A, Yamazaki H, et al. Study of activation cross sections of proton induced reactions on barium: Production of 131Ba 131Cs. Appl Radiat Isot 2010;68:1869–77. doi:10.1016/j.apradiso.2010.03.010.

[121] Tárkányi F, Hermanne a., Takács S, Ditrói F, Király B, Kovalev SF, et al. Experimental study of the 165Ho(p,n) nuclear reaction for production of the therapeutic radioisotope 165Er. Nucl Instruments Methods Phys Res Sect B Beam Interact with Mater Atoms 2008;266:3346–52. doi:10.1016/j.nimb.2008.05.005.

[122] Beyer GJ, Zeisler SK, Becker DW. The Auger-electron emitter 165 Er: excitation function of the 165 Ho(p,n) 165 Er process. Radiochim Acta 2004;92:219–22. doi:10.1524/ract.92.4.219.35608.

[123] Zandi N, Sadeghi M, Afarideh H. Evaluation of the cyclotron production of 165Er by different reactions. J Radioanal Nucl … 2013;295:923–8. doi:10.1007/s10967-012-2116-0.

[124] Tárkányi F, Takacs S, Hermanne A. Investigation of production of the therapeutic radioisotope 165 Er by proton induced reactions on erbium in comparison with other production. Appl Radiat … 2009;67:243–7. doi:10.1016/j.apradiso.2008.10.006.

[125] Song TY, Kim JW, Kim HI, Lee CW, Lee YO, Yang SC, et al. Measurement of Activation Cross Sections of Erbium Irradiated by Proton Beam. Nucl Data Sheets 2014;119:249–51. doi:10.1016/j.nds.2014.08.068.

[126] Loveland WD, Morrissey DJ, Seaborg GT. Modern Nuclear Chemistry. 2005. doi:10.1002/0471768626.

[127] Dash A, Pillai MRA, Knapp FF. Production of ^{177}Lu for Targeted Radionuclide Therapy: Available Options. Nucl Med Mol Imaging (2010) 2015;49:85–107. doi:10.1007/s13139-014-0315-z.

[128] Chakraborty S, Vimalnath K V., Lohar SP, Shetty P, Dash A. On the practical aspects of large-scale production of 177Lu for peptide receptor radionuclide therapy using direct neutron activation of 176Lu in a medium flux research reactor: the Indian experience. J Radioanal Nucl Chem 2014;302:233–43. doi:10.1007/s10967-014-3169-z.

[129] Nielsen CH, Erlandsson M, Jeppesen TE, Jensen MM, Kristensen LK, Madsen J, et al. Quantitative PET Imaging of Tissue Factor Expression Using 18F-labled Active Site Inhibited Factor VII. J Nucl Med 2015:89–96. doi:10.2967/jnumed.115.154849.

[130] Nielsen CH, Jeppesen TE, Kristensen LK, Jensen MM, El Ali HH, Madsen J, et al. PET Imaging of Tissue Factor in Pancreatic Cancer Using 64Cu-Labeled Active Site-Inhibited Factor VII. J Nucl Med 2016;57:1112–9. doi:10.2967/jnumed.115.170266.

[131] Stimmel JB, Kull FC. Samarium-153 and Lutetium-177 chelation properties of selected macrocyclic and acyclic ligands. Nucl Med Biol 1998;25:117–25. doi:10.1016/S0969-8051(97)00151-0.

[132] Mausner L. The in vivo generator for radioimmunotherapy. J Label … 1989;89:498–500.

[133] van Rooyen J, Szucs Z, Rijn Zeevaart J. A possible in vivo generator 103Pd/103mRh--recoil considerations. Appl Radiat Isot 2008;66:1346–9. doi:10.1016/j.apradiso.2008.02.088.

[134] Szucs Z, Rooyen J van, Zeevaart J. Recoil effect on β-decaying in vivo generators, interpreted for 103 Pd/ 103m Rh. Appl Radiat Isot 2009;67:1401–4. doi:10.1016/j.apradiso.2009.02.022.

[135] Zeevaart J, Szucs Z. Recoil and conversion electron implications to be taken into account in the design of therapeutic radiopharmaceuticals utilising in vivo generators. J Label … 2012;55:115–9. doi:10.1002/jlcr.2906.

[136] Nica N. Nuclear Data Sheets for A = 140. Nucl Data Sheets 2007;108:1287–470. doi:10.1016/j.nds.2007.06.001.

[137] Maecke HR, Reubi JC. Somatostatin receptors as targets for nuclear medicine imaging and radionuclide treatment. J Nucl Med 2011;52:841–4. doi:10.2967/jnumed.110.084236.

[138] Fani M, Del Pozzo L, Abiraj K, Mansi R, Tamma ML, Cescato R, et al. PET of Somatostatin Receptor-Positive Tumors Using 64Cu- and 68Ga-Somatostatin Antagonists: The Chelate Makes the Difference. J Nucl Med 2011;52:1110–8. doi:10.2967/jnumed.111.087999.

[139] Köster U. ISOLDE target and ion source chemistry. Radiochim Acta 2001;89:749–56. doi:10.1524/ract.2001.89.11-12.749.

[140] dos Santos Augusto R, Buehler L, Lawson Z, Marzari S, Stachura M, Stora T, et al. CERN-MEDICIS (Medical Isotopes Collected from ISOLDE): A New Facility. Appl Sci 2014;4:265–81. doi:10.3390/app4020265.

[141] Russell GJ. Spallation Physics - An Overview. Int Collab Adv Neutron Sources KEK Tsukuba 1990:291–9.

[142] Krása A, Rež AK. Spallation Reaction Physics. Fac Nucl Sci Phys Eng Czech Tech Univ Prague 2010.

[143] Marquez B V, Ikotun OF, Zheleznyak A, Wright B, Hari-Raj A, Pierce R a, et al. Evaluation of 89 Zr-pertuzumab in Breast Cancer Xenografts. Mol Pharm 2014;11:3988–95. doi:10.1021/mp500323d.

[144] Del Monte U. Does the cell number 10^9 still really fit one gram of tumor tissue? Cell Cycle 2009;8:505–6. doi:10.4161/cc.8.3.7608.

[145] Onsum MD, Geretti E, Paragas V, Kudla AJ, Moulis SP, Luus L, et al. Single-cell quantitative HER2 measurement identifies heterogeneity and distinct subgroups within traditionally defined HER2-positive patients. Am J Pathol 2013;183:1446–60. doi:10.1016/j.ajpath.2013.07.015.

[146] Advancing Nuclear Medicine Through Innovation. vol. 176. Washington, D.C.: National Academies Press; 2007. doi:10.17226/11985.

[147] Mestel R. IMAGING WITH ANTIBODIES. Nature 2017;543:743–6. doi:10.1038/543743a.

[148] Dijkers EC, Oude Munnink TH, Kosterink JG, Brouwers a H, Jager PL, de Jong JR, et al. Biodistribution of 89Zr-trastuzumab and PET imaging of HER2-positive lesions in patients with metastatic breast cancer. Clin Pharmacol Ther 2010;87:586–92. doi:10.1038/clpt.2010.12.

[149] Gaykema SBM, Schr??der CP, Vitfell-Rasmussen J, Chua S, Munnink THO, Brouwers AH, et al. 89Zr-trastuzumab and 89Zr-bevacizumab PET to evaluate the effect of the HSP90 inhibitor NVP-AUY922 in metastatic breast cancer patients. Clin Cancer Res 2014;20:3945–54. doi:10.1158/1078-0432.CCR-14-0491.

[150] Van De Watering FCJ, Rijpkema M, Perk L, Brinkmann U, Oyen WJG, Boerman OC. Zirconium-89 labeled antibodies: A new tool for molecular imaging in cancer patients. Biomed Res Int 2014;2014. doi:10.1155/2014/203601.

[151] Solomayer EF, Becker S, Pergola-Becker G, Bachmann R, Krämer B, Vogel U, et al. Comparison of HER2 status between primary tumor and disseminated tumor cells in primary breast cancer patients. Breast Cancer Res Treat 2006;98:179–84. doi:10.1007/s10549-005-9147-y.

[152] Perk LR, Vosjan MJWD, Visser GWM, Budde M, Jurek P, Kiefer GE, et al. P-Isothiocyanatobenzyl-desferrioxamine: A new bifunctional chelate for facile radiolabeling of monoclonal antibodies with zirconium-89 for immuno-PET imaging. Eur J Nucl Med Mol Imaging 2010;37:250–9. doi:10.1007/s00259-009-1263-1.